Generation of non-classical light using ultra-cold Rydberg ensembles

Masterarbeit

Johannes Schmidt

24. Oktober 2014

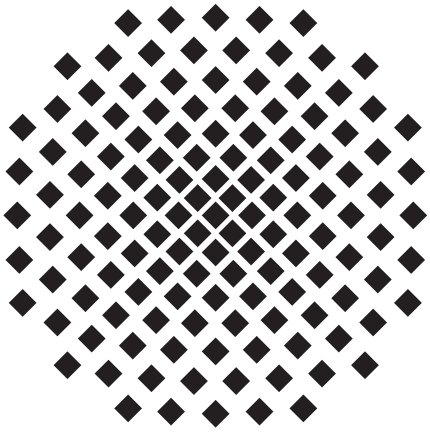

Universität Stuttgart
5. Physikalisches Institut

Hauptberichter: Dr. Sebastian Hofferberth

Mitberichter: Prof. Dr. Wolfgang Bolse

Zusammenfassung

In dieser Arbeit wird ein Einzelphotonen Transistor, der auf der Rydberg-Rydberg Wechselwirkung basiert, vorgestellt. Mit dieser Methode ist es auch möglich den Blockaderadius um Rydberg-atome räumlich aufgelöst darzustellen. Dazu wurde ein Abbildungssystem entwickelt und vermessen. Um das bestehende Experiment grundlegend zu verbessern wurde eine Vorrichtung zum steuern elektrischer Felder in einer neuen Glaskammer entworfen, aufgebaut und getestet. Dies eröffnet die Möglichkeit externe Streufelder zu kompensieren, atomare Wechselwirkungen einzustellen und Rydbergatome auf eine destruktive Weise zu detektieren, indem man sie ionisiert und daraufhin auf einem Detektor nachweist. Außerdem wurde das Verfahren der Quantenzustands Tomographie mithilfe der Maximum Likelihood Abschätzung aufgebaut und getestet. Dies sind alles Schritte auf dem Weg zur Verwirklichung eines kontrollierten Phasengatters.

Abstract

In this thesis a single photon-transistor realized by Rydberg-Rydberg interaction is being presented. Using this method it is possible to spatially resolve the blockaded region around Rydberg atoms. For this purpose an imaging system has been designed and tested during the course of this thesis. As a major improvement of the current experiment setup an electric field control has been designed, assembled and tested in a new glass chamber. This opens up the possibility of compensating external stray fields, tuning atomic interactions and detecting Rydberg atoms in a destructive way by ionization and subsequent detection on an ion detector. Furthermore the method of quantum state tomography using maximum likelihood estimation has been set up and tested. These are all steps towards the future goal of realizing a controlled phase gate.

Contents

1. Introduction

The topic of preparing, changing and detecting quantum states encoded in the state of light is called quantum optics. In quantum mechanics the radiation field is not only regarded as an electromagnetic wave, but light is considered to be consisting of single particles, the photons. The great challenge in engineering quantum mechanical states like Fock states, squeezed states or "Schrödinger cat" states [1] is, that photons interact only very weakly among each other. For this reason one needs a nonlinear medium on the few photon level, which could in the simplest case be one single atom coupled to the light field. Unfortunately this is limited by the finite scattering rate between photons and atoms [1].
Solid state systems like quantum dots and nitrogen vacancies in photonic crystal cavities were able to proof, that it is possible to modulate the amplitude and the phase of some few photons [2, 3]. Drawback of such systems is still the low coupling efficiency and it is hard to manufacture a large amount of systems in an indistinguishable way [4]. In optical cavities with high finesse, interactions between single photons have already been realized by coupling atoms to the electromagnetic mode inside the cavity [5, 6]. But these systems suffer from the bad scalability and big technical challenges with which one has to cope. A different way to increase the interaction of the atoms with the light field is by using single-mode hollow-core fibers. In those systems, the strong confinement enables the interaction of the light field with already a few atoms [7, 8].
Another promising approach to induce nonlinearities on a few photon level is to utilize ultracold atomic gases with atoms excited to Rydberg levels [9]. Rydberg atoms are highly excited atoms with principal quantum numbers $n \gg 1$ [10]. Therefore the Rydberg atoms have similar properties like Hydrogen, making them a comparatively clean and predictable system. They have exaggerated properties, which make precise engineering of the interaction strength between the Rydberg atoms and ground state atoms feasible. For example the dipole-dipole interaction scales with n^4 and the radiative lifetime with n^3. Moreover the strong polarizability, which scales with n^7 facilitates tuning of the interaction strength [11]. These systems show a blockade effect, which prohibits the excitation of a similar second Rydberg atom in the vincinity of the first one [9, 12]. Benefiting from this property it was possible to develop atomic quantum gates [13, 14].
The nonlinear and tunable behaviour of Rydberg atoms makes them the ideal mediator between quanta of light. It is possible to map these strong atomic interactions on the light field by electromagnetically induced transparency (EIT), where a photon gets transformed into a quasiparticle, the polariton [15]. Polaritons propagating through the medium at distances smaller than the Rydberg blockade radius will experience a shift of the susceptibility, which means a change of the absorptive and refractive properties of the medium [16–18].
This opens the opportunity to realize for example a controlled phase gate. Such a gate leaves one basis state $|0\rangle$ unchanged, whereas the perpendicular state $|1\rangle$ gets mapped onto $e^{i\theta}|1\rangle$ [19]. With such methods at hand we are coming closer to the vincinity of the implementation of multi-photon entanglement, quantum feedback circuits, repeaters and computers [20–22].

Structure of this thesis The work at hand is divided into four main parts, which pave the way towards realizing a phase gate. In the first chapter the mechanism and the measurement results of a single-photon transistor using strong Rydberg-Rydberg interactions are being presented [23]. This transistor offers the ability of switching the number of transmitted photons in a controlled way. It proofs the strong interaction between Rydberg atoms and points towards the possibility of realizing a controlled phase gate.
This scheme also offers the ability to spatially resolve the blockaded region around a Rydberg atom. In the course of this thesis an imaging system has been designed and characterized, which makes observation of the blockaded region around Ryberg atoms possible. This is topic of the second chapter.
With regard to more possibilities of controlling the quantum state of Rydberg atoms, the experimental setup had to be improved. One approach was to include a construction for manipulating electric fields. The design, assembly and characterization of the electric field control is part of the third chapter. It consists of eight electrodes, which permit compensation of external stray fields and manipulation of the interaction strength [10]. The construction includes also the ability of detecting Rydberg atoms in a destructive manner, by ionizing them and detecting the ions on a detector, namely a microchannel plate [11]. We also exchanged the vacuum chamber with a new one produced out of quartz glass.
In the fourth chapter a possible way of actually measuring a phase shift caused by a controlled phase gate is introduced. Quantum state tomography enables us to determine the full density matrix of the quantum state of light encoded in the polarization of the light field. For this purpose the scheme was thoroughly tested and characterization methods for the optics involved in this measurement process are presented.

2. Single-Photon Transistor Mediated by Interstate Rydberg Interactions

2.1. Transistor scheme

2.1.1. Motivation

One main building block in realizing quantum computers and communication is a controlled NOT gate [14]. We were able to contribute to the ongoing developements by implementing an all-optical transistor on a single photon level (Publication: [23], Viewpoint: [24]). With our setup we were able to show attentuation of over 10 source photons by one single gate photon. Although gain greater than one has already been demonstrated in cavity QED experiments [25], we could show, that this is possible in free-space as well using electromagnetically induced transparency (EIT) as the underlying basic building block [26]. This is one path towards enabling quantum memories, repeaters [27], generating Schrödinger cat states and improving the detection efficiency for photons [28].
Similar results have been published by the quantum optics group in munich [29].

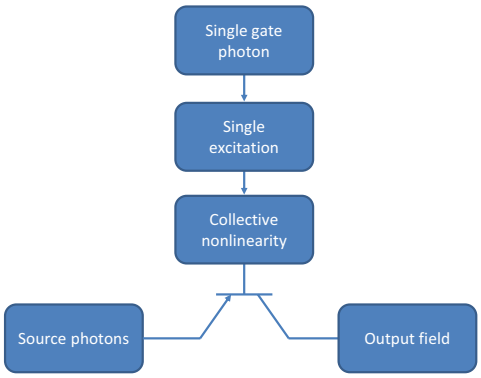

Figure 1: Basic principle of the transistor.

2.1.2. Basics

Rydberg atoms are in our case excited via a two-photon process, illustrated in figure 2. Interestingly, there occurs a transparency window for the probe field ε, if the probe field is tuned directly on resonance with the intermediate level $|5P_{3/2}\rangle$. This is because there are in theory two ways to excite the intermediate state $|5P_{3/2}\rangle$. The one path is obviously $|g\rangle \rightarrow |e\rangle$ excited by the probe field ε, the other path is $|g\rangle \rightarrow |e\rangle \rightarrow |r\rangle \rightarrow |e\rangle$ done by the probe field and the control field Ω via stimulated emission. These two pathways have certain quantum mechanical probabilities, which interfere destructively. The overall eigenstate is no longer coupled to the intermediate state, which leads to transmission of the probe field. This phenomenon is called electromagnetically induced transparency (EIT) [30]. If the probe field is tuned offresonantly, then the 3-level system is effectively reduced to a 2-level system and the probe field gets scattered at the intermediate state. The resulting transmission as function of detuning δ of the probe field from the intermediate state can then look like it is shown in figure 4 (rigth side, brown curve). The fit and the theoretical background can be found in the review by Fleischhauer et al. [31]. The FWHM of the transparency window is given as $\Delta = \frac{\Omega_c^2}{\Gamma\cdot\sqrt{\mathrm{OD}}}$, where Γ is the decay rate of the intermediate state given as

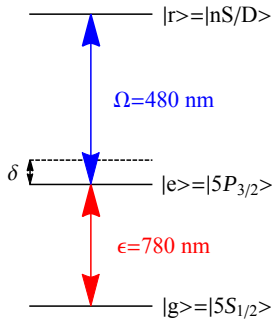

Figure 2: Excitation scheme.

$\Gamma = 2\pi \cdot 6.0666(18)$ MHz [32], OD is the optical depth and $\Omega_c/2\pi = \frac{\mu \cdot E}{2\pi\hbar} = \frac{\mu}{h \cdot w_0}\sqrt{P\varepsilon_0 c\pi^3}$ is the Rabi frequency with the transition dipole moment μ, which can be approximated by $\mu(5P_{3/2} \longrightarrow nS_{1/2}) = 4.4025 \cdot n^{*^{-3/2}} \cdot e \cdot a_0$. P is the laser power with beam waist w_0. Note, that the height of the transparency window is also determined by the coherence decay rate.
The excitation travels then as a spinwave or polariton through the cloud and the probe light gets effectively slowed down.
If one switches the control field off, while the major part of the probe field is still inside the cloud, then the spinwave is not able to propagate any further and the excitation gets stored, decaying only with the lifetime of the excited state [33].

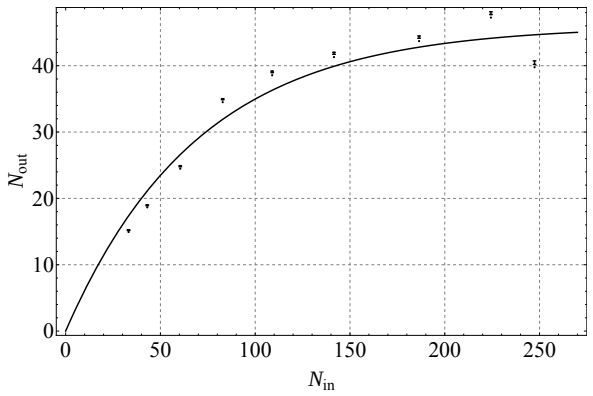

Figure 3: Self-blockade. Outgoing number of photons as function of the amount of incoming photons per delay time.

A Rydberg excitation interacts with all atoms inside a sphere around it via dipole-dipole interaction, which shifts their Rydberg energy levels $|r\rangle$. This interaction can be modelled in the non-degenerate case by a van der Waals interaction. The van der Waals coefficient C_6 giving the strength of the interaction $U(r) = h\frac{C_6}{r^6}$ can either be calculated by numerically diagonalizing the interaction Hamiltonian and by fitting the van der Waals interaction $U(r) = h\frac{C_6}{r^6}$ to the resulting energy spectra or by the approximating equation $C_6 = n^{11} \cdot (11.97 - 0.8486 \cdot n + 0.003385 \cdot n^2)$ [34]. A result of this interaction is, that a second excitation can not be in the same sphere as the first Rydberg atom, because the level scheme is shifted and the EIT condition is lost. This is called the blockade effect and the blockade radius is given as $r_b = (C_6/\Delta)^{1/6}$ [20, 35]. This effect is visible in the transmission of the probe photons, which will be scattered at the intermediate level. The relation between incoming and outgoing probe photons is shown in figure 3 and can be fitted with an exponential saturation function [36] (see section 2.2.3).

2.1.3. Mechanism

The excitation scheme and the transmission spectra are depicted in figure 4. The gate photons are stored in the medium by coupling the ground state $|g\rangle = |5S_{1/2}, F = 2, m_F = 2>$ to the Rydberg state $|r_g\rangle = |90S_{1/2}, m_J = 1/2>$ with the control field Ω_g in a two-photon Raman process. The probe field ε_g is detuned by $\delta_g = 40$ MHz from the intermediate state $|e\rangle = |5P_{3/2}, F = 3, m_F = 3>$. The source photons are tuned to the EIT resonance, $\delta_s = 0$, by the weak probe field ε_s and are coupled to the Rydberg state $|r_s\rangle = |89S_{1/2}, m_J = 1/2>$ by the control field Ω_s. That means, in the absence of a gate excitation they are traveling through the transparent medium at reduced velocity. If a gate excitation is present prior to the source excitation, then the interaction between $|r_g\rangle$ and $|r_s\rangle$ shifts the energy levels of the source excitation and therefore the EIT condition gets lost.

As a consequence the source photons ε_s get scattered from the intermediate state $|e\rangle$. This works only inside the blockade sphere around the gate excitation, where the interaction strength $U(r_b)/h$ is greater than the EIT transparency window $\Delta = 2$ MHz and the optical depth is high enough. One can imagine, that the EIT transparency window gets shifted, the 2-photon resonance gets lost and the source photons end up in the transmission valley of the spectrum.

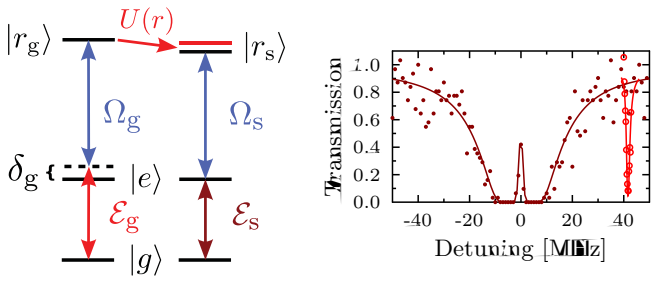

Figure 4: Left: Level scheme, Right: Transmission spectra of source photons (brown) and gate photons (red), taken from [23].

2.1.4. Setup and choice of states

For our implementation we use a pairwise counter-propagating configuration of the probe and coupling beams of source and gate, like it is shown in picture 5. This has the advantage, that we are able to reduce Doppler shifts and we minimize crosstalk of source and gate probe photons at the beamsplitter. The coupling and probe beams are separated by dichroic mirrors before coupling the probe beams into the fibers to the single-photon detectors. Like this we can simultaneously detect transmitted gate and source photons with the single-photon detectors PD_s and PD_g, which are the COUNT-250C-FC from Laser Components. We use two different excitation states in order to avoid an unwanted readout. One could use only one excited state and one coupling laser as well and switch polarization between gate and source excitation with an EOM [37], thereby coupling to different hyperfine levels. The disadvantage is, that the polarization will never be rotated perfectly and a partial readout of gate excitations will be unavoidable. For our choice of state combination numerical simulations yield a van der Waals coefficient of $C_6 = -4.70 \cdot 10^7$ MHz $\cdot\, \mu$m^6. Assuming a width $\Delta = 2$ MHz of the EIT transparency window, the blockade radius is $r_b = 14.5\ \mu$m, which is much larger than the extent of the excitation beams. The $1/e^2$ radii of the gate and source probe lasers are 5 μm, assuring that the blockade radii will always be larger than the excitation region in radial direction.

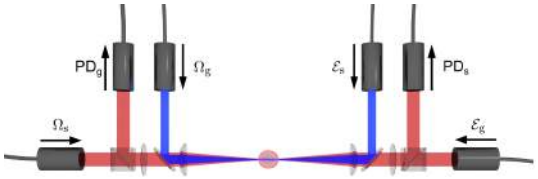

Figure 5: Schematic of our excitation and detection setup.

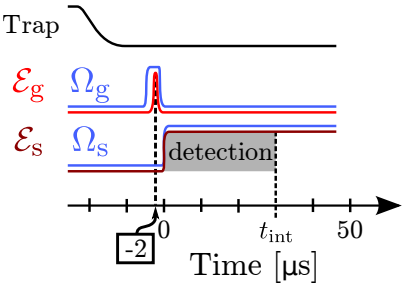

Figure 6: Pulse sequence, taken from [23].

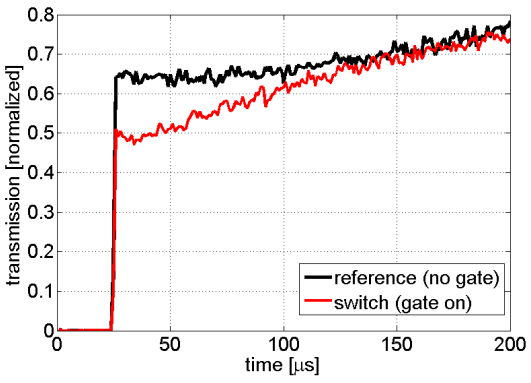

Figure 7: Sample of transmitted source photons. Black: Reference without gate excitation, Red: Source photons with gate excitation.

The power of the gate coupling laser is 240 mW, which is the maximum power of the lasers and corresponds to a Rabi frequency of 12.3 MHz. The power of the source coupling laser is 60 mW, which is a Rabi frequency of 6.3 MHz. We choose the larger power for the gate excitation to increase the probability to store a gate photon. The power of the source coupling laser was set such, that the EIT spectrum showed a narrow enough transparency window but at the same time the largest peak height possible for this tradeoff. The optical depth OD = 25 of our system can be determined by a fit to the transmission valley of the source photons [31]. Our experiment cycle is shown in picture 6. After loading our atoms in a MOT, resulting in a temperature of 40 μK and 10^7 atoms we transfer them in an optical dipole trap with trap frequencies $\omega_r = 2\pi \cdot 3500$ Hz and $\omega_z = 2\pi \cdot 3600$ Hz, which corresponds to an extent of $\sigma_r = 25$ μm radially and $\sigma_l = 40$ μm in the longitudinal direction. The dipole trap consists of a crossed dipole trap with a dimple beam perpendicular to it (see also chapter 4.3.1). With this trap setting we can make sure, that we have at maximum only three gate excitations inside the cloud. The resulting temperature of the atoms determined by time-of-flight series is 40 μK. The traps are then switched off, to avoid level shifts due to the AC-Stark effect of the trap lasers. Afterwards a coherent gate pulse containing on average one photon is sent in the cloud, after a waiting time of 2 μs the source photons are sent through the medium.
The resulting transmitted signal of source photons can look like in figure 7. Clearly, the transmission of source photons is being attenuated for about 100 μs, which corresponds to the lifetime of the gate excitation. The reference signal without gate excitation is depicted in black. The transmission increases due to the expanding cloud and consequently loss of optical depth. The whole experiment cycle takes about 1.5 s.

2.2. Characterization

From many measurements like shown in figure 7 and an integration time of 30 μs we are able to derive some characteristic quantities of our transistor. The integration time is chosen such, that the expansion of the cloud is negligible but large enough to gather a significant amount of statistical data.

2.2.1. Limits

There are several mechanisms limiting the overall performance of our transistor.

- We use coherent photon sources. That means, that our photon arrival will always be governed by Poissonian statistics. The probability to emit k photons is given by $P_{\bar{N}} = \frac{\bar{N}^k}{k!} e^{-\bar{N}}$.
- The overall detection efficiency, including single photon counters and fiber coupling efficiency is 0.31 for the source photons and 0.27 for the gate photons.
- The gate photons might be transmitted as a spinwave through the medium, because the coupling light is switched on too long. The amount of transmitted gate photons can be monitored by the single-photon counter PD_g. On the other hand, if the coupling

light is switched on too short, then the source gate photons get scattered away at the intermediate level. The timing has been optimized on the efficiency of our transistor.

- There is still a finite probability, that the gate photons get scattered at the intermediate level. We measured the finite absorption $A_{ge} = 0.15$ independently with no coupling light at an OD of 25 and a detuning of 40 MHz.

The overall amount of stored gate photons $\bar{N}_{g,st}$ is then given by

$$\bar{N}_{g,st} = (1 - A_{ge}) \cdot \bar{N}_{g,in} - \bar{N}_{g,out}, \tag{1}$$

where $\bar{N}_{g,in}$ denotes the average amount of gate photons going into the cloud and $\bar{N}_{g,out}$ is the average amount of photons coming out of the cloud. There may still be mechanisms removing the gate excitation, but which cannot be large, as we will see in the next section.

2.2.2. Contrast

We start by keeping the weak source input photon rate fixed at $R_{s,in} = 0.69(1)\ \mu s^{-1}$. In figure 8 (left) we plot the optical switch contrast

$$C = 1 - \left(\bar{N}_{s,out}^{\text{with gate}} / \bar{N}_{s,out}^{\text{no gate}} \right) \tag{2}$$

as a function of the mean number of ingoing gate photons $\bar{N}_{g,in}$, which have been determined by reference measurements. The contrast is mainly governed by Poissonian statistics. In a perfect switch all gate photons get stored perfectly and the interaction works perfectly inside the blockaded region. In this case the contrast is given by the probability of emitting photons out of the coherent gate probe laser: $C_{coh} = 1 - e^{-\bar{N}_{g,in}}$. This behaviour is depicted as dashed line in figure 8. The number of actually stored gate excitations can be measured and calculated with equation (1). Plotting the contrast as function of the number of stored gate excitations together with the theoretical limit for a coherent light source shows (figure 8), that other possible loss mechanisms must be very small, since we are already approaching the theoretical limit very closely.

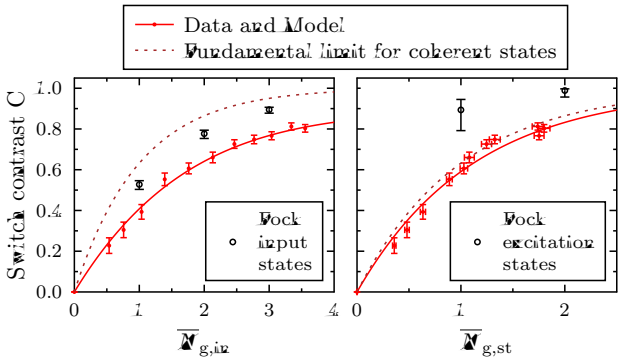

Figure 8: Contrast as function of the number of ingoing gate photons. Left: Actual measurement, Right: Contrast corrected for finite storage efficiency. Taken from [23].

The gate excitation acts on the source photons like a medium with some finite optical depth OD_{sp} and because at maximum three gate excitations fit into our cloud, the expected switch contrast can be given by

$$C(\bar{N}_{g,in}) = 1 - \sum_{k=0}^{\infty} \frac{\bar{N}_{g,in}^{k} e^{-\bar{N}_{g,in}}}{k!} e^{-\min(k,3) \cdot \text{OD}_{sp}}. \tag{3}$$

Fitting this function to our data yields an optical depth $\mathrm{OD}_{sp} = 0.75(5)$ of the gate excitation acting on the source photons. Calculating the optical depth for the actually stored gate excitations yields $\mathrm{OD}_{st} = 2.2(7)$.
The expected contrast using a deterministic gate photon source with k photons can be calculated by

$$C_{Fock}(k) = 1 - e^{-\min(k,3)\cdot \mathrm{OD}_{sp}}. \tag{4}$$

Correspondingly for actually stored Fock input states $C_{Fock,st}(k) = 1 - e^{-\min(k,3)\cdot \mathrm{OD}_{st}}$. These data points are depicted black in figure 8.

2.2.3. Gain

Next, we keep the average number of ingoing gate photons fixed at $\bar{N}_{g,in} = 0.75$ and use an integration time of $t_{int} = 90\ \mu$s, which is comparable to the fly-away time of the stored gate excitations. For low source photon rates we can redo the contrast calculations and get a contrast of $C_{coh,90\mu s} = 0.22(3)$, an optical depth of $\mathrm{OD}_{sp} = 0.45(1)$ for a single Fock input state and an optical depth of $\mathrm{OD}_{st} = 0.94(10)$ in the case where the deterministic gate photon is actually stored.

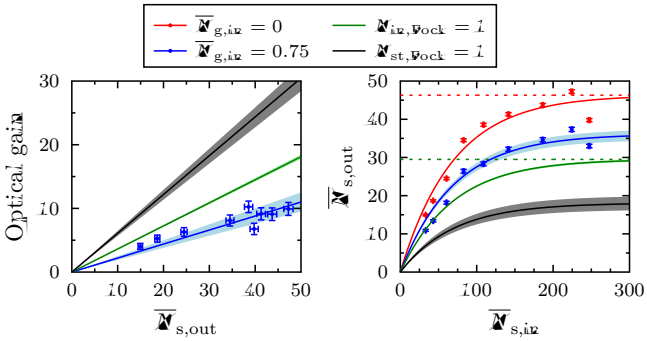

Figure 9: Left: Optical gain as function of outcoming source photons. Left: Number of outcoming source photons as function of ingoing source photons. Taken from [23].

As another figure of merit we use the optical gain defined by

$$G = \bar{N}_{s,out}^{\text{no gate}} - \bar{N}_{s,out}^{\text{with gate}}, \tag{5}$$

which is the amount of attenuated source photons. This is shown in figure 9 (left, blue). The maximum optical gain is $G = 10(1)$. Further increase is limited by the self-blockade of the source photons, which is shown in figure 9 on the right in red without any gate photons. Fitting to these data points a function $\bar{N}_{s,out} = a \cdot (1 - e^{-\bar{N}_{s,in}/b})$ [36], yields $a = 46$ and $b = 70$. Multiplying this fit with the extinction $(1 - C_{coh,90\mu s})$ results in the blue line. This line fits very well to the blue data points. This is evidence, that the transistor is mainly limited by the self-blockade of the source photons, but could achieve a robust gain $G \gg 1$ for around 250 incoming source photons if the self-blockade of the source photons can be overcome. The other lines result all from multiplying the red line with $(1 - C)$, with the contrasts $C_{in,Fock} = 0.362(2)$ and $C_{st,Fock} = 0.61(3)$.

2.3. Nondestructive Rydberg detection

In order to use our transistor scheme, we show, that it is possible to detect Rydberg atoms non-destructively in one single shot. In figure 10 histograms of source photon counts are shown, not corrected for the detection efficiency of the single-photon counters and obtained from 250 runs. If no gate excitation was present, $\bar{N}_{\text{stored}} = 0$, then the counting statistics of the coherent source photons clearly follow a Poissonian curve (blue).

When on average $\bar{N}_{\text{stored}} = 0.61$ excitations are present, then this histogram is shifted towards zero events and the Poissonian characteristic is lost. From the considerations in chapter 2.2.2 we know, that the averaged storage events still consist of parts, where no gate photon was present due to the Poissonian statistics of the coherent gate probe light. This part is given by the blue histogram weighted by the probability of having no gate photons $p(0) = e^{-\bar{N}_{stored}}$. The difference to the red histogram is the histogram of gated events weighted by their probability.

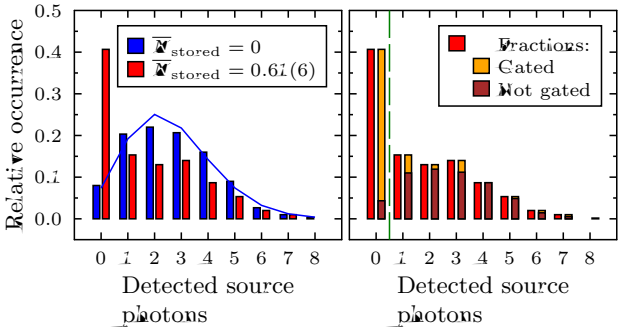

Figure 10: Left: Histogram of source photon events, Right: Decomposed histogram with gated and not gated fractions. Taken from [23].

In order to detect a Rydberg atom we are going to send some source photons inside the cloud. We want to know, at what amount of transmitted source photons we can still claim to have detected a Rydberg atom. Therefore we calculate the discrimination level (green line), whether no or one and more gate excitations were present. The fidelity of this prediction is given by the probability of successfully predicting zero gate excitations p_0 and the probability of predicting one or more gate excitations p_g.

$$p_0(x) = \left(\sum_{k=x}^{\infty} h_0(k)\right) / \left(\sum_{k=0}^{\infty} h_0(k)\right) \tag{6}$$

$$p_g(x) = \left(\sum_{k=0}^{x} h_g(k)\right) / \left(\sum_{k=0}^{\infty} h_g(k)\right) \tag{7}$$

$$F(x) \geq \min\left(p_0(x), p_g(x)\right) \tag{8}$$

We are using $h_0(k)$ as the height of the histogram bar of a not gated event and $h_g(k)$ as the relative number of gated events. Equation (8) is being optimized by taking the maximum of F for all x [29, 38]. The resulting discrimination level is $x < 1$ and $F = 0.79(4)$. (More about fidelities in chapter 5.1.4).

2.4. Improvements and outlook

There are some improvements, which could be made:

- In order to lower the self-blockade effect one could reduce the size of the atomic cloud to $\sigma_l = r_{gs}/2$, without changing the overall OD.
- One can try to tune the interaction such, that $r_{gs} \gg r_{ss}$ by using dipole-coupled (in first order) state combinations or Förster resonances, like the Förster resonance between $n = 69$ and $n = 67$ [29]. Note, that for spatial detection, r_{gs} must remain smaller than half the distance between the gate excitations, which can be approximated by $r_{gg}/2$.

The next step is to read out the stored gate excitations by switching the gate coupling light on again after the transistor experiment. This requires long coherence times, which can be achieved by using state combinations with lower principal quantum numbers and by eliminating electrical stray fields, which is the topic of chapter 4. This paves the way towards multi-photon entanglement, quantum feedback circuits, nondestructive detection of gate photons and optical probing of Rydberg excitation dynamics [21, 22]. A possible application of the transistor scheme presented here is the spatially resolved detection of the blockade sphere around the Rydberg atoms, which is the topic of the next chapter.

3. Imaging Setup

3.1. Detection proposal

Common imaging techniques used to detect single atoms measure the fluorescence or absorption employing strong optical transitions. In systems where a lot of decay paths exist this is no longer possible. After a successful excitation the possibility, that the atom decays in a state, which is no longer coupled to the imaging light is very high. Therefore only very few imaging photons can be scattered. One can of course try to enhance the transition rate by placing the atom inside a cavity in which transitions other than the imaging transition are not resonant, but only by loosing spatial resolution.
A way out can be given by our transistor scheme introduced in chapter 2.1. In this case, the imaging photons or, in the language of our transistor, the source photons are no longer scattered at the imaging object itself, but at all the ground state atoms sitting inside the blockaded region around the gate excitation. This greatly enlarges the impact of the Rydberg atom on the imaging light field [21, 22, 39]. As explained in chapter 2.2, the amount of scattered imaging photons is then mainly limited by the self-blockade.
The technical limitation of the low signal-to-noise ratio will still partly remain, since our scheme will always suffer from photon-shot noise and from density fluctuations inside the atomic cloud. One expects from this technique insights in dynamic processes, like for example diffusion or the formation of lattices by self-assembly of Rydberg atoms. During this thesis I designed and tested an imaging system consisting of three lenses, which will be used to image the blockaded region around Rydberg atoms in the future.

3.2. Design

The imaging setup was developed using the ray-tracing program Zemax. I want to outline briefly some parameters, which can give good indications about the quality of an optical system.

3.2.1. Optical parameters

Airy radius: The Airy radius is the distance d at which two self illuminating objects can still be distinguished

$$d = 1.22 \cdot \lambda / \sin(\alpha) \tag{9}$$

with α being the angle of the cone of light that could possibly enter the imaging system. It sets the maximum resolution of an imaging system [40]. In our case α is at most 32°and $\lambda = 780$ nm resulting in a minimal object size of 1.8 μm.

Modulation-Transfer-Function: The contrast or modulation is defined as:

$$Modulation = \frac{I_{max} - I_{min}}{I_{max} + I_{min}} \tag{10}$$

For example the 1951 USAF resolution test chart, which consists of different sizes of three horizontal and vertical bars, has a modulation almost equal to 1.0. By transferring such a pattern through an optical system, it gets convoluted with all the imaging errors of the system and the image will have reduced contrast. A function that makes a statement about the contrast or the response of the system for all spatial frequencies is called the Modulation-Transfer-Function (MTF). It shows for perfect contrast, $Modulation = 1$, in the object plane, what contrast to expect in the imaging plane. High contrast becomes particularly interesting when dealing with very low photon rates and a low signal-to-noise ratio. The MTF characterizes the ability of a system to resolve objects depending on their size and it is therefore one of the most important benchmarks of an imaging system [40].

Aberrations: In linear optics one normally makes an approximation of first order of the kind $\sin(\alpha) \approx \alpha$, where α is the angle between the light ray and the optical axis. For light rays with large angles to the optical axis this is no longer valid and one has to take higher order contributions into account. The five image defects of third order are called spherical aberration, coma, astigmatism, field of curvature and distortion. They are quantized by the so called Seidel coefficients [40]. For designing an optical system they can give valuable hints on which optics or surface is causing unwanted effects and what optics has to be exchanged. They can also be measured with a so called Shack-Hartmann sensor, which was unfortunately not available at the time of the design and characterization of the imaging system presented here.

3.2.2. Elements

A drawing of the objective exported from Zemax is shown in figure 11. All lenses can be bought from Thorlabs.

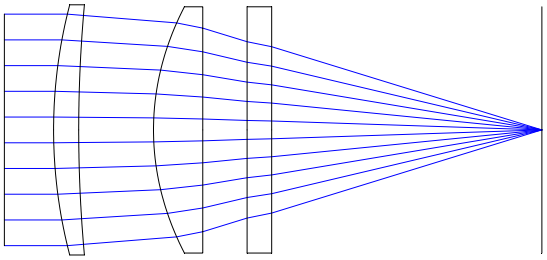

Figure 11: Objective: From left to right: Image plane, LE1985-B, AL50100-B, Glass 5mm N-FK5, object plane.

The objective consists of a sample glass plate made from the same quartz glass as the new glass chamber. This glass plate sits in a distance of 54.9 mm away from the position of the atomic cloud. In Zemax I chose the quartz glass type N-FK5 with a thickness of 5 mm, which has similar properties like quartz glass. This glass wall causes spherical aberrations since the rays have to go under a steep angle through the surfaces. Next to the glass wall in a distance of 10 mm is a 2.0" aspheric lens AL50100-B. This lens has a numerical aperture of 0.240 and focal length of 100 mm which is much too large. In order to reduce the focal length we use

the 2” meniscus lens LE1985-B in a distance of 15.2 mm from the front surface of the prior lens. Meniscus lenses are designed such, that they cause a minimum of additional spherical aberrations, because light rays are being bent equally on both sides of the lens. This kind of assembly has a small focal length and at the same time induces a minimum of aberration into the system. This was motivated by a publication of L. M. Bennie et al. [41]. Ideally the beam should now be collimated.

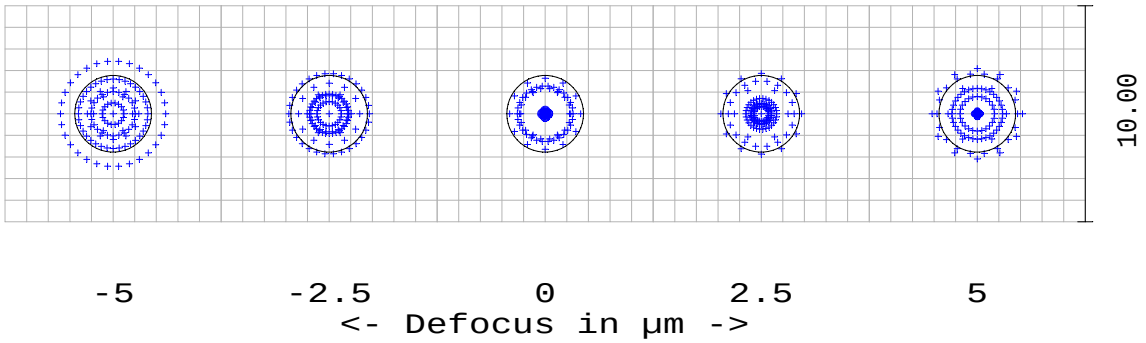

Figure 12: Spot diagrams through focus in the object plane.

Shining in a collimated beam from the image plane towards the object plane yields the through focus spot diagrams shown in figure 12. The distances of the lenses were optimized on the smallest rms radius, which is just small enough to be diffraction limited. The collimated beam is then focused down with a 2” plano-convex lens LA1727-B with a focal length of 750 mm. This yields in theory a magnification of 8.66. The camera used for testing is a pco.pixelfly usb camera with 1392x1040 pixels with a pixel size of 6.45x6.45 μm^2. Therefore an object of 2 μm size will be focused on 2.7 pixels, which will also roughly be the pixel to object size ratio used later on in the experiment, due to low intensity and signal to noise ratio. The objective lenses are mounted in a cage system from Thorlabs. The whole lens arrangement including the cage system costs around 600 Euro. Note, that commercial systems are magnitudes higher in price, which of course always depends on the desired resolution and the circumstances, like distance from the object or unavoidable aberrations from the glass walls of the vacuum chamber.

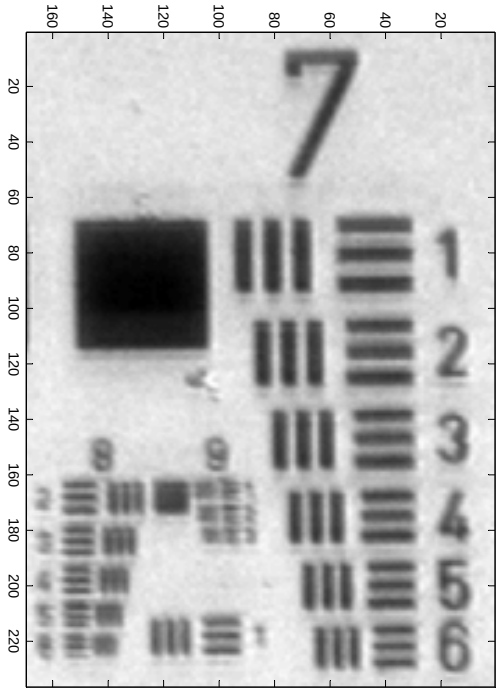

Figure 13: Picture of the 1951 USAF resolution test chart with group 8 element 3 (1.55 μm linewidth) still being visible. Unit is pixels.

3.3. Characterization

In order to see actual experimental results, we used the 1951 USAF resolution test chart mounted on a 3D translation stage with approximately 10 μm precision. The lenses of the objective were mounted in a cage system on the same rails. There is astigmatism in the system, which is due to the fact, that the lenses were slightly tilted. Laser light at 780 nm was used, dulled by a diffusor, which consists of a rough glass plate and a lab tissue mounted on a fast rotating motor. This yields a homogeneous wavefront travelling towards the object. The resulting light power was 1.9 mW. Unfortunately this motor also caused a lot of vibrations. An exposure time of 100 μsec was used, which is long enough to average over local changes in intensity due to the fast rotating diffusor but short enough to prevent a blurry picture.
An example picture of the test chart focused on the 8th group, 1st element can be seen in picture 13. This corresponds to a distance of the bars of 1.95 μm. One can see, that the bars of the 3rd element in group 8 are still easily distinguishable by eye and the contrast averaged over both directions is $(26.5 \pm 0.9)\%$. Therefore it is reasonable to claim a resolution of (1.55 ± 0.1) μm. This is almost diffraction limited as the Abbe limit is $d = \lambda/\mathrm{NA} = 1.5$ μm, which is valid for this kind of setup. The magnification is (8.53 ± 0.37), which is in good accordance to the calculated magnification of 8.66.

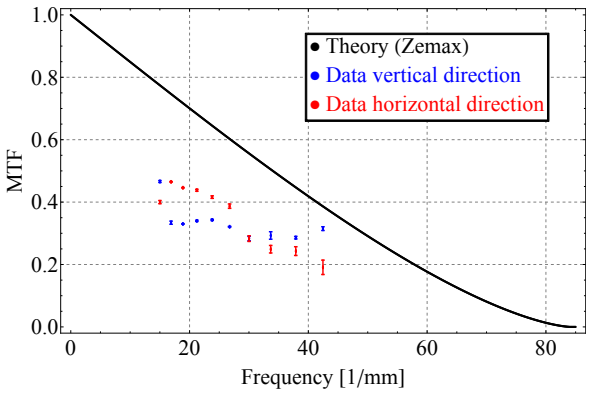

Figure 14: MTF over spatial frequency in the imaging plane: Black: Theoretical prediction, Blue and red: Measurement taken by averaging 10 pixels in horizontal and vertical direction and calculating the contrast.

In order to extract the contrast, pictures of all elements in group 7 and of the first four elements in group 8 in focus were taken. By averaging over 10 pixels for each horizontal and vertical bar, the contrast was calculated. The resulting MTF including the theoretical prediction from Zemax are shown in figure 14. The two imaging directions seem to have different contrast, which is because of astigmatism caused by slightly tilted lenses. Moreover, the contrast will also be distorted by having decreasingly less pixels per structure of interest. Overall the contrast should in principle be much better, but is mainly limited by the interplay of dynamical range of the camera, required exposure time and illumination of the testtarget. But still it is possible to grasp the trend of the MTF and a contrast of $(26.7 \pm 0.5)\%$ for the 8-1 element can be confirmed. The attempt to measure the depth of field with the test chart failed, because the translation stage was not precise enough. I can only claim it to be in the

range (10 ± 10) μm. The same applies to the field of view. The best way would have been to look at the Airy disk of a pinhole and position it with a piezo stage. With this one could have reconstructed the pointspread function. But there was neither a suitable pinhole at hand, nor a translation stage with the required precision.
Nonetheless, the pictures show, that the setup serves our purposes. One has to keep in mind, that for the actual experiment a much more sensitive camera has to be used, which will not necessarily have the same pixel sizes. Therefore the magnification has to be set again.

4. Electric Field Control

4.1. Motivation

The electric field control developed and built during this thesis enables us on the one side to compensate external stray fields, resulting in a smaller linewidth of the Rydberg energy levels and therefore a more stable frequency position thus yielding more stability for the whole experiment. On the other hand one can also tune the energy levels of Rydberg atoms, in order to use for example Förster resonances, which can have preferable interaction strength and blockade radii [42]. This enables using lower principal quantum numbers, which have longer coherence times and therefore we might improve the total performance of our transistor experiment for instance.

The option to ionize atoms opens furthermore a whole new field of experiments. By applying electric field pulses with high amplitude, Rydberg atoms can be ionized and detected on an ion detector [11]. With this we are able to verify the Rydberg detection scheme introduced in chapter 2.3 with the number of ions incident on the detector. Another very important application is the "cleaning" of atomic states, which are no longer coupled to the light field but do still interact with the surrounding atoms [20]. This can in principle permit a much higher experiment rate, because one can perform several measurements using only one single cloud. Of course only when the switching time of the high voltage can be realized fast enough. High experiment rates are crucial for our measurements, since we need a lot of cycles to gather a significant amount of statistical data, which is not distorted by drifts of the setup.

Figure 15: Complete E-field control sitting inside the glass chamber.

4.2. Theoretic background

4.2.1. DC-Stark shift

The Stark shift of an atomic level caused by a DC electric field can be calculated either by diagonalizing the full Hamiltonian (atomic + Stark) or by perturbation theory. For the non-degenerate S-, P-, and D-states, second order perturbation theory yields a quadratic Stark shift

$$\Delta_{\text{Stark}} = \frac{1}{2}\alpha E^2. \tag{11}$$

The dependence of the polarizability α on the effective principal quantum number n^*

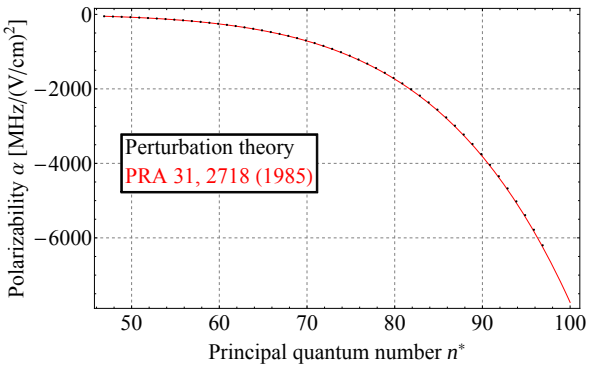

Figure 16: Polarizability α depending on the principal quantum number extracted from simulations und from equation (12).

was extracted from experimental data [43]:

$$\alpha\left[\mathrm{MHz/(V/cm)^2}\right] = 2.202\cdot 10^{-9} n^{*6} + 5.53\cdot 10^{-11} n^{*7} \tag{12}$$

The calculated polarizability as well as data from a simulation are shown in figure 16. From equations (11) and (12) one can calculate the Stark shift resulting from an applied electric field. For example a single ion sitting in a distance of 30 mm will cause an electric field of $E(30\mathrm{mm}) = \frac{e}{4\pi\varepsilon_0\cdot(30\mathrm{mm})^2} = 1.6\cdot 10^{-9}$ V/mm at the position of the atomic cloud. This corresponds to a Stark shift of $\Delta_{Stark} = 4.9\cdot 10^{-7}$ Hz for $n^* = 90$, which is vanishlingly small, since we can observe shifts of around 10 MHz.

4.2.2. Electric field ionization

The potential between the valence electron and the Rydberg atom in a classical approximation is a superposition of the Coulomb potential $V_{Coulomb}(r) \simeq -1/r$ and the external electric potential $V_{field} = -eE\cdot z$. This is depicted in figure 17. This classical approximation is valid for large electric fields. The field required to ionize an atom in a given Rydberg state can be estimated as [11]

$$|E| = \frac{\pi\varepsilon_0 R_{\mathrm{Ryd}}^2}{e^3 n^{*4}} = 3.2136\cdot 10^5 \frac{\mathrm{kV}}{\mathrm{cm}}\cdot\frac{1}{n^{*4}} \tag{13}$$

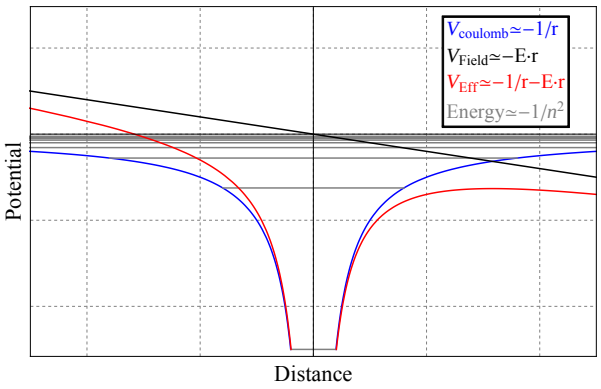

Figure 17: Scheme of the discrete energy levels lying inside a Coulomb potential and the superposition of this potential with an external electric potential.

with R_{Ryd} being the reduced Rydberg constant for the specific species. The dependence of the ionization voltage on the principal quantum number is shown in figure 25. As one can see in the figures 17 and 25, it is getting more and more difficult to ionize the Rydberg atoms stateselective, because the ionization voltage has to be set increasingly accurate with no overshooting and as homogeneous across the atomic cloud as possible with increasing principal quantum number. For lower quantum numbers this is feasible, but for higher ones, beginning at n=80 to n=90, the ionization threshold is no longer clearly distinguishable due to tunneling processes for example.

4.3. Design ideas

Several requirements on the electric field control have to be met.

4.3.1. Optical access

One of the main requirements is to maintain optical access to the atomic system. The beams, that use the most space are the three MOT beams with a diameter of approximately one centimeter. In between the two MOT beams are the beams for the Raman sideband cooling, the optical dipole trap and the excitation lasers. Perpendicular to these beams must be space left for either imaging or the dimple beam, which is used to form a smaller cloud.

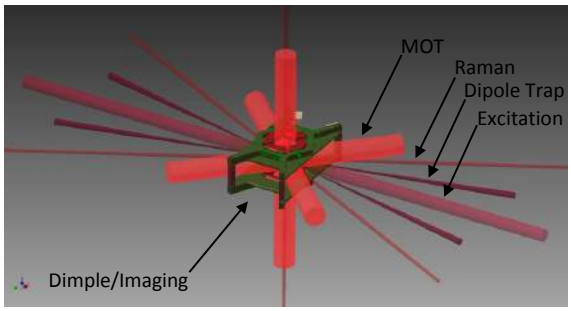

Figure 18: Sketch of the beams passing the glass chamber. The imaging/dimple beam is not shown.

4.3.2. Shielding of charges

A major issue with glass surfaces near the atomic cloud is that glass is a dielectricum, which cannot conduct charges. A charge, which was once created and got stuck on the surface will only by chance move away. There are possibilities to get rid of charges on dielectric surfaces like ITO-coating, which is not compatible with Rubidium, or shining in with UV-light, which mostly worsens the problem. The same applies to all other dielectric objects, like ceramics, such as Macor, or lenses near the atomic cloud. The best idea is to shield all those charges thoroughly away by as many metal surfaces as possible.

4.3.3. Design of the electrodes

Since previous works [11, 42, 44] have shown, that a cloverleaf like configuration of the field plates is able to provide a sufficient compensation for excitation of Rydberg levels up to $n \approx 200$, we decided to use a similar configuration. In this way we can compensate stray electric fields in every direction and have at the same time optical access for the perpendicular MOT beams. Small field gradients can mainly be achieved by placing the two cloverleafs as far apart as possible, the remaining problem is the mounting and electric insulation from the rest of the assembly. The electrodes were designed such, that the surfaces diverge towards the middle of the cloverleaf. This was inspired by a previous work [45], although it had only minor impact on the electric field, at least in the simulations. The idea is to guide the field smoothly into the middle of the assembly and by this prevent large peaks of the field density.

4.3.4. Mounting the electrodes

The company tectra offers split bushes made from high purity Alumina (Al_2O_3), like they are shown in picture 30. Always two of those bushes are then used to guide a screw through the grounded metal into the electrode, thereby keeping the electrode from touching the ground. The bushes are sitting in half opened holes to enable venting and prevent virtual leaks.

4.3.5. Mounting the whole assembly

Figure 19: Baseplate sitting inside the spherical octagon held by Groove Grabbers.

The whole E-field control is held by long angled plates. These plates are attached via a baseplate to four so called Groove Grabbers from Kimball Physics [MCF600-GrvGrb-C01]. These Groove Grabbers are clamped into two notches inside a spherical octagon from Kimball Physics [MCF600-SphOct-F2A8]. This construction has the major advantage, that in the end the glass cell can simply be slipped over the whole device, without having to tinker anything inside the cell afterwards.

4.3.6. Choice of materials

There are two things to keep in mind when choosing a material. First it has to be suitable for ultra high vacuum, that means it should have a very low outgassing rate and it should be nonmagnetic, because every magnetic dipole near the atoms causes unwanted dephasing. A third issue is, that Rubidium can react very aggressively with some materials, like gold for example. A metal with nonmagnetic properties is Titanium. But like nearly all stainless metals it builds up a passive layer of some metaloxide on the surface, which prevents further corrosion of the material and which is a dielectricum. This layer can, in the case of Titanium, be very thick, has a yellow colour and is an outstanding strong dielectricum with a dielectric constant of $\varepsilon = 111$ to $\varepsilon = 257$, depending on the crystal orientation [46]. This material is therefore unfeasible for our purposes. Our choice fell on the stainless steel AISI 316L, the european DIN standard is 1.4404, this material can be bought in different sizes, for example from fruechtl-kronos. It is an austenitic stainless steel, which is nearly not magnetizable. This kind of steel is mostly used for vacuum parts and flanges [47]. It is for example also used for the complete particle accelerator at CERN [48]. The disadvantage of this steel is the inner tension inside the material, which makes machinig of precise and in particular large parts very hard.

4.3.7. Glass cell

Our first glass cell was made from borosilicate glass from the company JapanCell, because we wanted to evaporate Rubidium atoms from the glass surfaces by heating the glass with UV-light, thereby enhancing the Rubidium background pressure in the glass cell. This could

in principle lead to shorter MOT loading times [49]. Borosilicate is especially suitable for this method, because it absorbs UV-light better than quartz glass. In the end it turned out, that we leave the Rubidium dispensers switched on all the time and do not need additional UV-light, since MOT loading times are nonetheless acceptable. However the borosilicate glasses tend to show thermal lensing. If an intense highly focused beam hits the glass, the parallel glass surfaces transfrom into small lenses with a focal length of approximately 11 mm. This corrupts every stability effort, since one can no longer adjust with a cw-beam. Every ramp or pulse pattern with the dipole trap will lead in the end to a displacement of the atomic cloud. The effects of this thermal lensing were tested with sample glasses made from borosilicate and quartz glass in different configurations using an Ytterbium broadband laser at 1064 nm from IPG Photonics (PYL-20-M-CP), which has an output power of over 30 W. Below in the figures 20 we plot the beam diameter measured with our beammaster, which consists of a webcam chip with appropriate evaluation software, versus the power of the laser. "f" denotes the focal length of the used lens, "d" is the distance of the sample to the lens and α is the angle by which the sample was rotated. A schematic sketch is shown in figure 21.

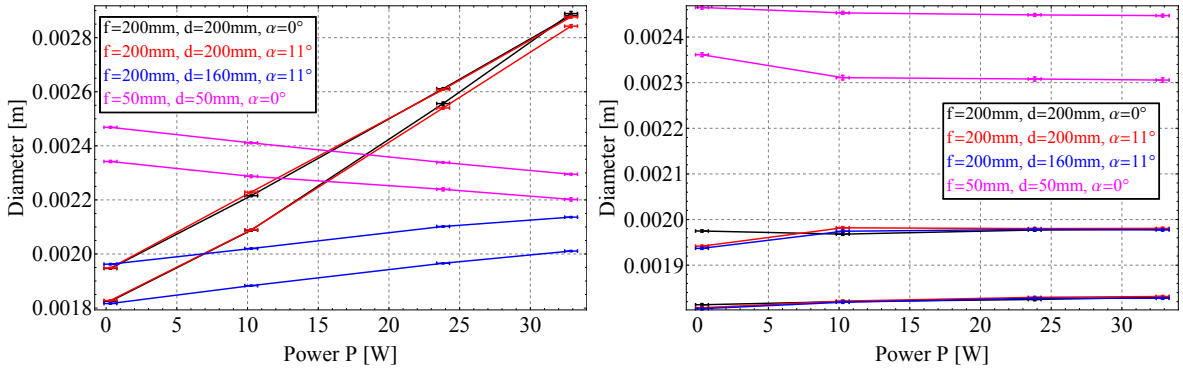

Figure 20: Effect of thermal lensing on the beam diameter depending on the laser power. Left: Borosilicate, Right: Quartz. The two lines for each configuration denote the two different diameters in x- and y-direction.

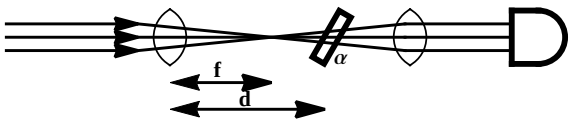

Figure 21: Setup used to measure the influence of thermal lensing on the beam diameter.

The quartz glass shows, apart from small measurement fluctuations, no thermal lensing, whereas the borosilicate shows tremendous dependence on the input power.

The new glass cell was manufactured again by JapanCell and is made from quartz glass. In the front, where the whole experiment takes place, sits a glass box. This is followed by a tube with a glass metal transition, which ends on a metal flange. This is necessary to steadily adapt the different coefficients of thermal expansion of the glass and the metal flange. The glass parts are bonded together with Epoxy. All glass surfaces have an antireflection coating

optimized for the wavelengths 420, 480, 532 and 1064 nm with a reflectivity smaller than 1.5% and smaller than 1.0% for the wavelength 780 nm [50]. A picture of the cell is shown in figure 30.

4.3.8. Ion detectors

Either the microchannel plate (MCP) F4655-13 from Hamamatsu or the channeltron Magnum 5901 from Photonis will be used to detect ions, see chapters 4.7.1 and 4.7.5.

4.4. Simulations

The program SIMION 8.1 was used to simulate electric fields and particle trajectories. The resulting data sets were then imported to MATLAB. Below in figure 23, slices through the position of the cloud in the assembly are shown for different voltage settings at the electrodes. In all cases the voltages -2000 V and -500 V are applied to the front and back plate of the MCP (-3000 V is applied to the channeltron respectively) and -0.05 V to the mesh in front of the MCP. The mesh voltage was chosen such, that sufficient compensation of the fields can be guaranteed while maintainig the ability to attract even very slow ions. In this way the most general and practical statements can be made.

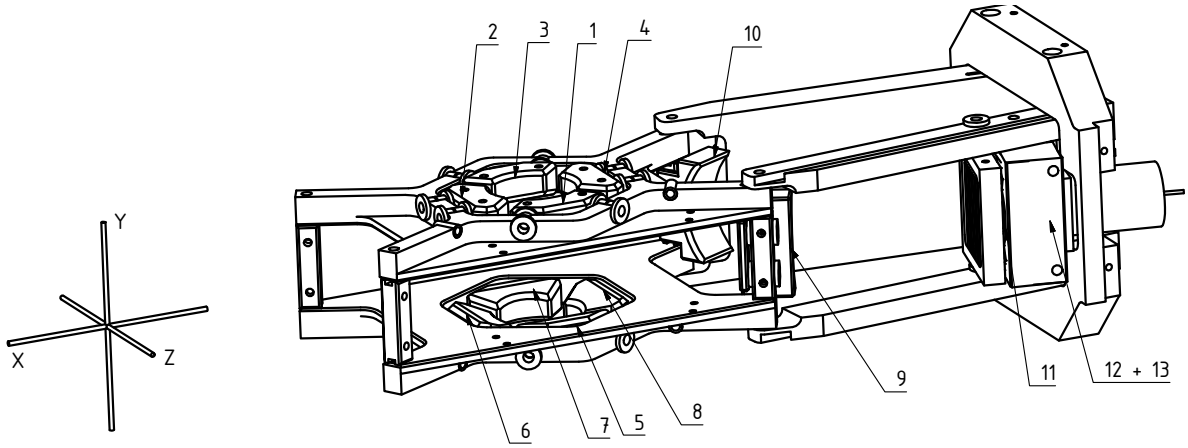

Figure 22: Schematic drawing of the front part of the E-field control with numbering of the plates and reference system. Electrodes 1-8: Electric field compensation, Electrodes 9-10: Steering of the ionized atoms, Electrode 11: Mesh for compensation of the fields of the channeltron/MCP, Electrodes 12-13: Channeltron/MCP.

4.4.1. Influence of the MCP and the channeltron

The fields of the MCP shown in figure 23 have only small influence on the fields at the position of the cloud. This is mainly due to the mesh in front of the MCP. Simulations for the channeltron at the place of the MCP show very similar behaviour.

The voltages that need to be applied to compensate the influence of the MCP are given in table 1. These voltages are very small, although at least in theory the voltage source USB3112 (see also chapter 4.6.4) should be able to provide $10\ \mathrm{V}/2^{16}\mathrm{bits} = 153\mu\mathrm{V/bit}$. We expect from previous works [11, 42, 44], that in the end some 10 mV to 100 mV will be necessary to compensate for Stark shifts. One has to keep in mind, that an electric field on the order of $\approx 10^{-6}$ V/mm causes for a quantum state with $n^* \approx 100$ a shift of 10 Hz, which is no longer resolvable with our excitation lasers, due to their linewidth of at least 50 kHz.

Electrode	Voltage [mV]
1, 5	0.16
2, 6	0.0
3, 7	0.1
4, 8	0.45

Table 1: Voltages required to compensate the influence of the MCP on the electric field.

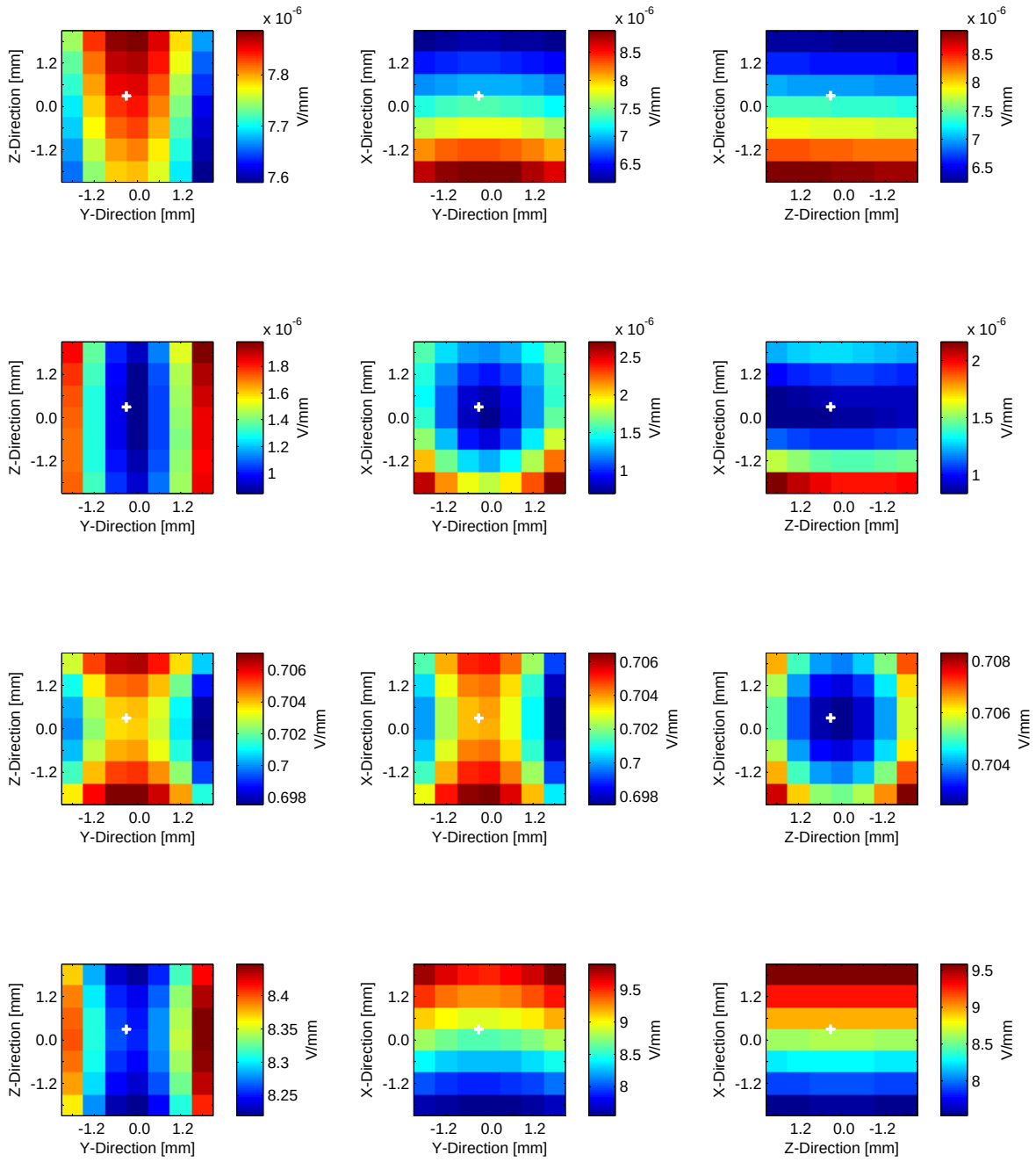

Figure 23: First row: Fields generated by the MCP and the mesh with all other electrodes switched off, Second row: Rough attempt to compensate the fields of MCP and mesh, Third row: Fields generated by putting plates 1-4 on +10 V and plates 5-8 on -10 V, Fourth row: Plates 2 and 6 on +500 V. (From top to bottom). The white cross indicates the position of the atomic cloud, which is due to the discrete grid and averaging slightly shifted. The colorbar indicates the absolute value of the electric field.

4.4.2. Electric fields created by the electrodes

The pictures 23 show, that it is possible to generate in theory a very homogeneous electric field across the atomic cloud with variations below 0.03 dB. From the pictures 23, the field at the position of the cloud depending on the applied voltage can be calculated. These straight lines are shown in picture 24. The relation between voltage and electric fields are as follows:

- Plates 1-4 positive, plates 5-8 negative: $E(U)[\frac{\mathrm{V}}{\mathrm{mm}}] = 0.070\frac{1}{\mathrm{mm}} \cdot U[\mathrm{V}]$
- Plates 1 and 5 positive: $E(U)[\frac{\mathrm{V}}{\mathrm{mm}}] = 0.021\frac{1}{\mathrm{mm}} \cdot U[\mathrm{V}]$
- Plates 2 and 6 positive: $E(U)[\frac{\mathrm{V}}{\mathrm{mm}}] = 0.017\frac{1}{\mathrm{mm}} \cdot U[\mathrm{V}]$

4.4.3. DC-Stark shift

From the equations (11) and (12) one can calculate the electric field required for compensating a specific Stark shift. A reasonable shift could be for example 10 MHz.

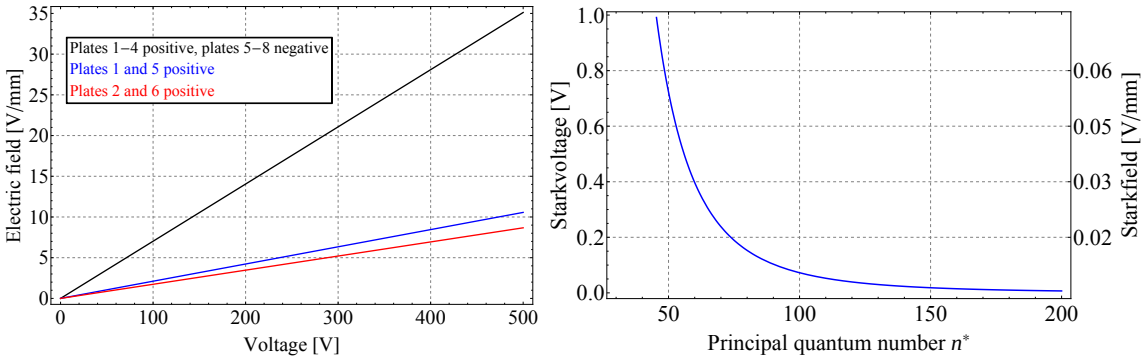

Figure 24: Left: Electric field depending on the applied voltage, Right: Electric field and voltage required to compensate a Stark shift of 10 MHz depending on the principal quantum number.

The voltage and the electric field needed in the case where the plates 1-4 are positively and the plates 5-8 are negatively charged depending on the principal quantum number for a shift of 10 MHz are shown in picture 24. As mentioned before, the required voltages are in the range of some 100 mV, which should be technically feasible with our voltage source, the USB3112.

4.4.4. Electric field ionization

We use again the relation between electric field and applied voltage for the case where only the plates 2 and 6 are positively charged.

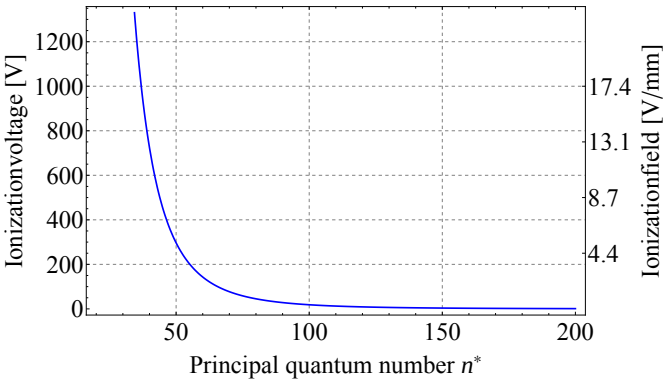

Figure 25: Electric field and voltage required to ionize an atom depending on the principal quantum number.

Then the ionization voltage depending on the principal quantum number looks as shown in figure 25. With 500 V we should be able to ionize every Rydberg state down to a principal quantum number of $n^* = 44$. This is a very good property, since we will not have to care about for example suitable high voltage cables and connectors and we will have a lot of freedom to easily ionize every Rydberg atom in the cloud.

4.4.5. Ion guiding

Once the Rydberg atoms are ionized, the ions are guided to the MCP (or channeltron respectively) with the steering plates 9 and 10. Ion trajectories have been calculated with SIMION for the maximum ionization voltage of 500 V at the plates 2 and 6. The MCP front plate is set to -2000 V, the back plate to -500 V and the steering plate 9 is set to -85 V. The Mesh in front of the MCP, which should absorb most of the fields going out of the channeltron, is charged with -0.05 V. The calculated trajectory for this parameter set is depicted in picture 26.

The starting points of the trajectories are normally distributed around the cloud position with a variance of 0.75 mm. Note, that depending on the voltage of the MCP and the actual cloud position, steering voltages of up to -100 V might be required. The round steering electrodes lead to a very flat distribution of the ions, which can be expanded using the electrodes 4 and 8 at a negative voltage. This is shown in the pictures 27. The mesh acts in such a voltage configuration (-0.05 V) on the ions like a lens with the focal point being in front of the MCP. Therefore the particles get distributed over the MCP without burning always one single spot on the MCP plates, see picture 27.

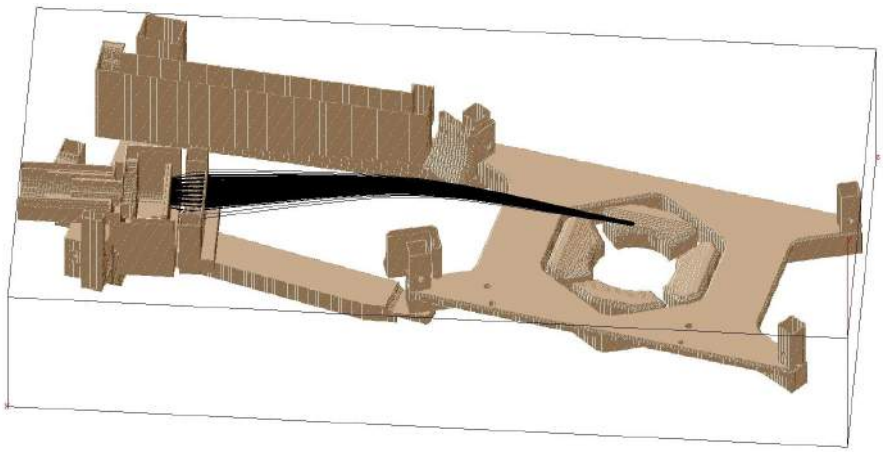

Figure 26: Trajectories of ions starting normally distributed around the position of the atomic cloud.

Remark I want to point out, that the presented values are only simulation data. In practice small ripples on the surfaces, the previously mentioned passive layer of metaloxide, glass and ceramics and the copper wires will influence the form of the electric field. It would be surprising if the presented data could exactly be reproduced in the experiment. The shown values should therefore give only a hint or estimation of the behaviour and the magnitude of the expected fields.

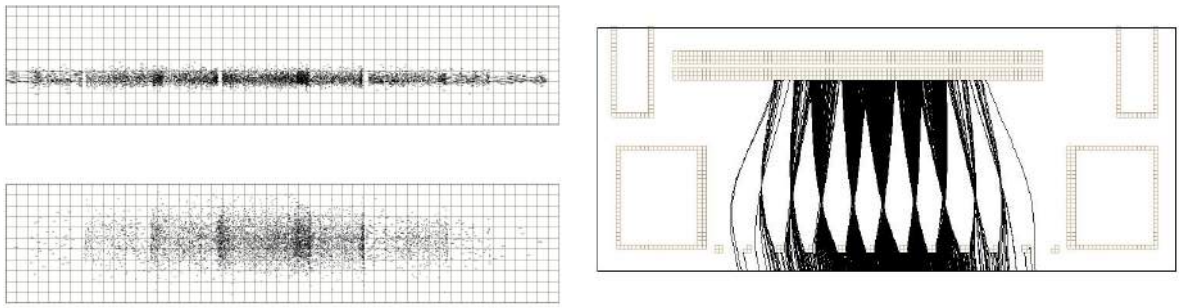

Figure 27: Left: Top: Endpoints of ion trajectories on the MCP, Bottom: Endpoints on the MCP with plates 4 and 8 on -40 V. Right: Lensing effect of the mesh. Cut through mesh and MCP. One grid point corresponds to 0.2 mm.

4.5. Assembly

Since we wanted to test the electric properties of the assembly and the characteristics of the ion detectors without the glass cell, we mounted the whole E-field control on the octagon and put several metal tubes and a small window on the octagon instead of the glass cell. This is shown in picture 28.

The assembly had to be done two times, since the delivered glass cell was over 5 mm too small in diameter. Therefore some parts had to be manufactured twice.

Figure 28: The test setup.

4.5.1. Cleaning procedure

All parts were cleaned after the procedure proposed in [51]:

- 20 minutes ultrasonic bath in industrial strength cleaner (Branson, IS-Industriereiniger)
- Thorough cleaning with water
- 20 minutes ultrasonic bath in acetone
- Flushing with isopropanol

Commercial parts like the octagon are assumed to be delivered vacuum clean. The Kapton insulated Copper wires were wiped clean with ethanol and lint free wipes (Kimwipes). All parts were exclusively handled with gloves and wrapped in aluminum foil.

4.5.2. Baking

In order to burn remaining dirt away, for example oil or isopropanol, we decided to bake all metal and ceramic parts in the test tube at a temperature of 300 °C. This conditioning helps also to achieve faster a high vacuum after reopening the chamber. We used two heating wires, five temperature sensors and the turbopump HiPace80 from Pfeiffer, which can get only in the range of $10^{-8} - 10^{-9}$ mbar. The pressure was measured with the gauge PKR251 from Pfeiffer. Unfortunately we wrapped too much of the wires around the chamber, so that after a while the smell of burnt plastic got so sickening, that we had to remove partly the aluminum foil to get the ends of the wires out. This is why one can see a temperature and pressure dip around the 5. June in the figures 29. The end pressure was $4.6 \cdot 10^{-8}$ mbar, so one can claim, that the E-field control shows no virtual leaks and assuming cleanliness should be suitable for ultra high vacuum.

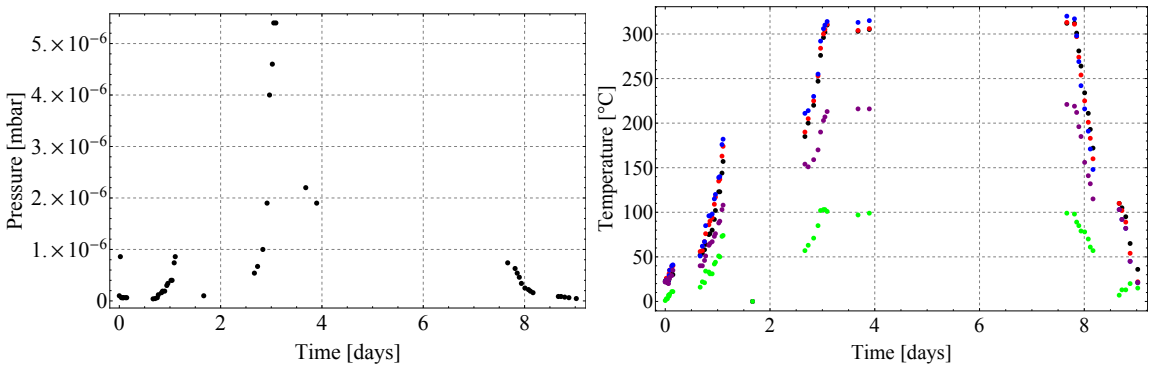

Figure 29: Left: Pressure, Right: Temperature at different positions of the test setup over time.

4.5.3. Wiring

The wires we use to connect all electrodes and supply voltages for the ion detector are Kapton insulated copper wires (FTAK10010) with a diameter of 1.1 mm from Kurt Lesker. Those wires have a breakthrough voltage of 10 kV and can hold currents up to 10 A. The Kapton at the tip of a wire was removed and wound around the screw of the corresponding electrode. The wires are guided from the electrode to the electrical feedthroughs in the octagon via ceramic tubes from tectra, which lie in half opened holes. Caution was taken, that at nearly no position the atoms or ions will ever see the bare wires. The endtips of the wires are connected to the feedthrough pins (EFT0542052) with Be-Cu barrel connectors (FTAIBC041) from Kurt Lesker. The insulation of the tips was not stripped this time, because the risk to cause dirt or damage on the knive edge with the scalpel inside the octagon was too high. Instead the screws in the barrel connectors were tightened as fast as possible and the electrical connection was tested with an ohmmeter with clean tips. Since only very small currents will flow through the connections, this is no problem. Little Macor plates with four holes are used to hold the pins of the feedthroughs apart.

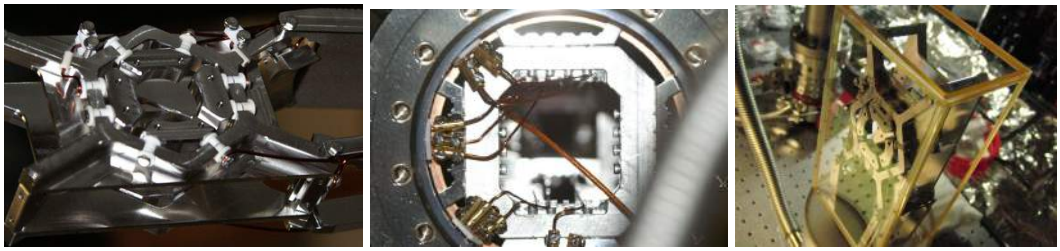

Figure 30: From left to right: E-field control wired; Octagon with Be-Cu connectors and Macor spacers; Finished assembly inside the glass cell.

Electrode	Resistance [Ω]	Capacity [pF]	Breakthrough voltage [kV]
1	0.4 ± 0.1	31.3 ± 0.1	3.6 ± 0.2
2	0.6 ± 0.1	33.4 ± 0.1	3.7 ± 0.2
3	0.6 ± 0.1	30.7 ± 0.1	3.6 ± 0.2
4	0.4 ± 0.1	30.8 ± 0.1	3.7 ± 0.2
5	0.2 ± 0.1	29.1 ± 0.1	3.6 ± 0.2
6	0.8 ± 0.1	31.9 ± 0.1	3.6 ± 0.2
7	0.4 ± 0.1	30.6 ± 0.1	3.6 ± 0.2
8	0.6 ± 0.1	31.5 ± 0.1	3.6 ± 0.2
9	1.4 ± 0.1	32.3 ± 0.1	3.5 ± 0.2
10	0.7 ± 0.1	26.4 ± 0.1	3.6 ± 0.2

Table 2: Characteristic electric properties of the electrodes.

4.6. Characterization

4.6.1. Resistance

The resistance was measured between the outer pins of the feedthrough to the corresponding electrode with an ohmmeter and vacuumclean probes. It shows, that the contact at the barrel connectors works. Measuring the resistance between the electrodes and the ground turned out to exceed the range of the ohmmeter. So it must be way over 20 MΩ.

4.6.2. Capacity

For measuring the capacity of one electrode, all other electrodes were grounded. Using the digital LCR/ESR-Meter Peaktech 2170 the capacity was measured. The measured capacities are obviously very small, thus the rise- and falltimes of charging will be dominated by the capacity and the inner resistance of the BNC cables, which are in the range of 200 pF and 50 Ω for a 2 m cable. In order to get a good prediction of the loading behaviour of the electrodes, one has to characterize the specific BNC-cables as well.

4.6.3. Breakthrough voltages

For measuring the breakthrough voltages an AppliedKilovolts voltage supply with 10 kV and a maximum curent of 4 mA was used. By turning up the control voltage very slowly and by checking the monitor voltage at the same time, rough estimates of the breakthrough voltage were gathered. It turned out, that nearly all electrodes showed breakthroughs at voltages between 1 kV and 2.2 kV, but by turning the voltage up again one can win one or two more kilovolts. This is because small ripples on the metals get polished away by the electric spark, which is also called high-voltage conditioning. The measured breakthrough voltages are basicly the breakthrough voltages at normal pressure in air. Assuming a distance of 2-3 mm at the sockets of the feedthrough pins and a electric strength of air of 3.3 kV/mm, this confirms this argumentation.
Note, that simply watching the monitor voltage is a very rough and even dangerous way to measure the breakthrough voltage. A much better way would have been to take a voltage source where the current can be limited manually. One can then limit the time of the breakthrough and go much more precisely towards the critical voltage without having to risk damage of the electric devices. Unfortunately no such device was available at the time of the measurements.

The breakthrough voltage or electric strength respectively is given by the Paschen law [52]:

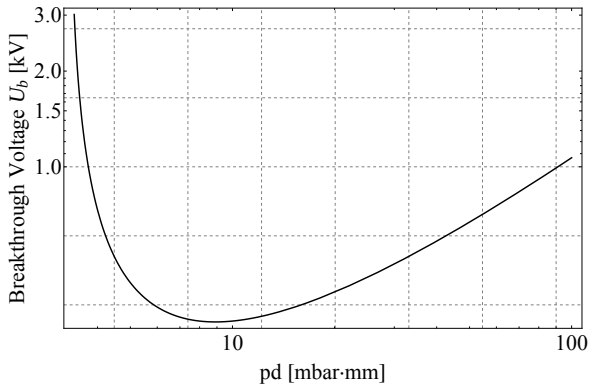

Figure 31: Breakthrough voltage over distance times pressure according to the Paschen law 14.

$$U_b = (B \cdot p \cdot d)/(\mathrm{Ln}(\frac{A \cdot p \cdot d}{K})), \qquad (14)$$

where p is the pressure, d the distance, and $K = \mathrm{Ln}(1 + 1/v)$, v, A and B are constants. For air they are given as $A = 1.2\ \mathrm{mbar}^{-1}\mathrm{mm}^{-1}$, $B = 36.5\ \mathrm{Vmbar}^{-1}\mathrm{mm}^{-1}$ and $v = 0.02$, yielding, $K = 3.39$ [53]. A plot of the relation (14) is shown in figure 31. For a distance of 3 mm and a pressure of $1.0 \cdot 10^3$ mbar this yields a breakthrough voltage of 16.1 kV. This is obviously much higher than measured, which is because the Paschen law is only valid for parallel and smooth plates.

4.6.4. Rise- and falltimes

As mentioned in chapter 4.6.2, the loading behaviour will mainly be given by the capacity of the BNC-cable. The signal generated by the Agilent 33500B function generator was measured first with 50 Ω termination at the LeCroy 64Xi (600 MHz). Then traces were recorded one time with 50 Ω termination at the feedthrough pin of electrode 2 and then completely unterminated. The traces are shown in figure 32. A similar measurement was done using the USB3112 microcontroller also shown in figure 32. Because the rise time of the output of this function generator is so slow, all ringing is suppressed and appropriate termination is not needed for

this measurement. In order to suppress high frequency noise a lowpass filter consisting of a 50 Ω resistor and a 2.2 μF capacity is soldered at the output ports of the controller. Attempts have been made to measure the Allan deviation of the voltage over time, but it turned out, that mostly only the fluctuations of the oscilloscope were measured. Nevertheless, major parts of the reflections can be suppressed by using a 50 Ω termination directly at the feedthrough. The best way would have been to put the resistor directly at the electrode, but that would again result in thermal drifts, because inside the vacuum heat cannot be dissipated and the current flowing through the resistor would therefore cause fluctuations of the resistance.

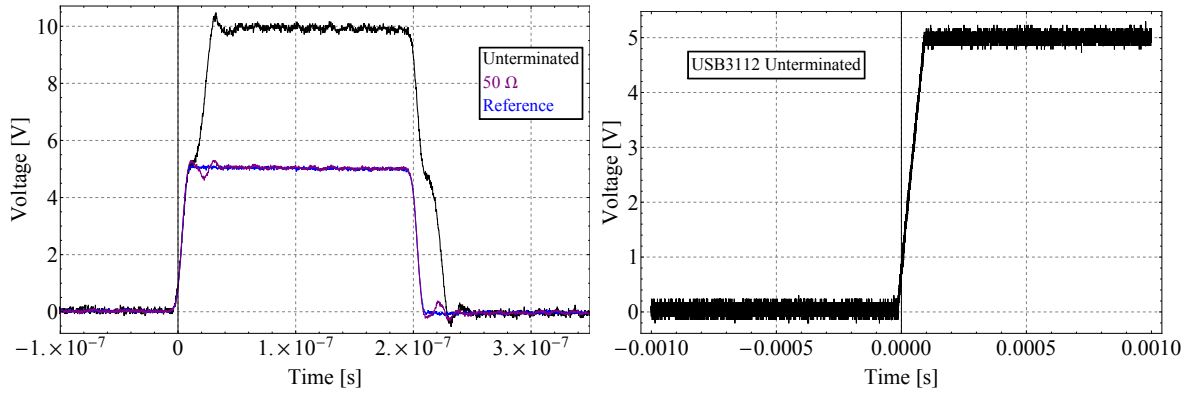

Figure 32: Switching behaviour of Agilent 33500B (left) and of USB3112 (right).

4.6.5. HV-Switch

For achieving the high ionization voltages of up to 500 V in very short time, we use the NIM-AMX500-3 from CGC Instruments. It consists of three separate channels where each has an internal resistance of 11 Ω. The output can be switched by a TTL pulse between a high and a low level. Using a 500 V voltage supply from Applied Kilovolts, presented in figure 36, and a 3 m BNC cable at electrode 2, which corresponds to a total capacity of 352 pF, the switch was characterized. Results and the measurement setup are shown in figure 33. The trigger pulse delivered by the Agilent 33500B is shown in red and black. For high voltages a crosstalk from the output to the trigger channel is visible. This crosstalk can also be observed after a trigger pulse in the output channel. The minimum trigger time is 330 ns and the lowest trigger voltage is 2.7 V. The output signal shows large overshooting, which can be suppressed by using a 57 Ω resistor in series in the output path. This enlarges the initial rise time, although the time at which a stable voltage level is achieved is similar to the time without resistor and is 500 ns. The same applies to the falling time, which is even more crucial for our experiment, since this sets the time when Stark shifts can again be compensated successfully.

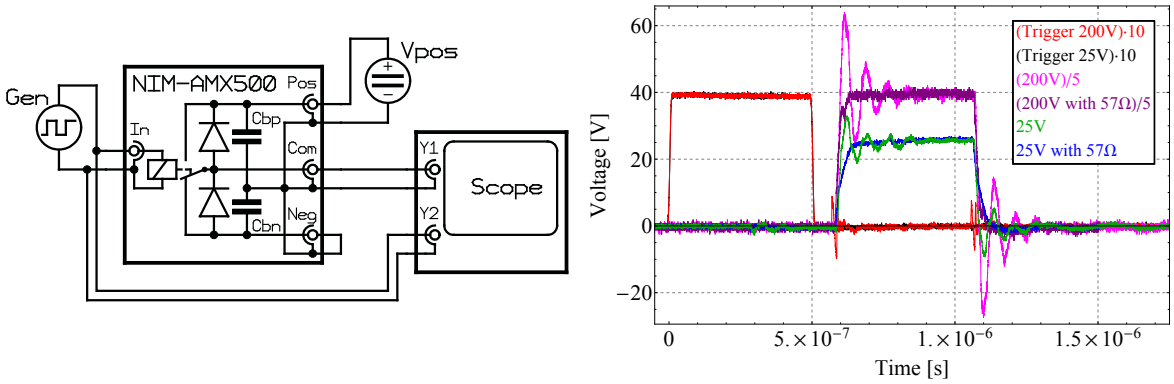

Figure 33: Left: Measurement setup, taken from [54], Right: Characterization measurements of the NIM-AMX500-3.

4.7. Ion detectors

We have the possibility to use two different ion detectors, which have both advantages and disadvantages. For both detectors housings and cables exist.

4.7.1. Microchannel Plate

Figure 34: Installed MCP with mesh in front.

The first of our ion detectors is a so called microchannel plate (MCP). These types of detectors consist of two plates made from several millions ultra-thin glass capillaries, which are fused together and sliced into thin plates of an average thickness of 0.5 millimeters [55]. A sketch of such a plate is shown in the figure 35 below. From the front to the back of the plates a high voltage in the kilovolts range is applied. Each of the capillaries acts as an independent electron multiplier, multiplying the charge of an incident ion by a gain of $g = \exp(\alpha \cdot G)$, where $\alpha = L/d$ is the length to diameter ratio and G is called the gain factor. The surface of these plates is covered by a thin metal layer, for example Inconel, a Nickel alloy or Ni-Cr, designed such, that the surface resistance is somewhere between 100 Ω and 200 Ω across the MCP's surface.

The angle between the channel axis and the axis perpendicular to the plate surface is called the bias angle and is in our case 12°. There are two reasons why one uses this bias angle. The first is, that there is a higher probability for incident particles to hit a channel wall. The other reason is more subtle. By enlarging the length to diameter ratio α one increases the gain, but at the same time noise caused by ion feedback increases ultimately limiting the gain by degrading the signal to noise ratio. Ion feedback is caused by residual gas atoms, which are being ionized inside a capillary. The resulting ions travel back to the front of the MCP and cause a wrong signal. This problem can be circumvented by using two alternately opposing plates. The ions are then absorbed at the junction between the two plates [57]. Of course this

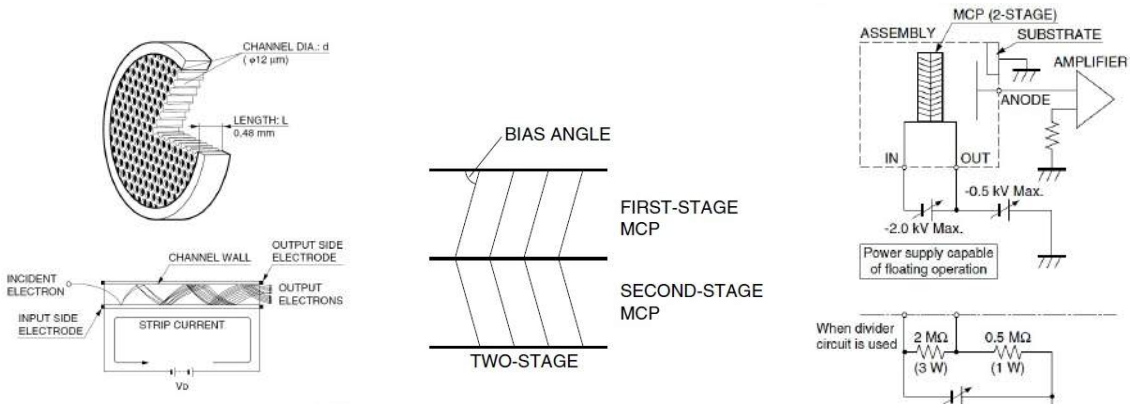

Figure 35: Left: Operating principle, Middle: Bias angle, Right: Wiring schematic. Taken from [55] and [56]

works best, when the channels are really opposed to each other, like it is shown in figure 35.

The resulting signal is in our case then read out by a single anode, which is made in a way, that only few parts of the resulting signal pulse gets reflected. This can be accomplished by manufacturing the angle of the cone as well as the surface in tight tolerances.

Our MCP is the F4655-13 from Hamamatsu, which is wired like it is depicted in the figure 35 above.

We use the voltage supplies from AppliedKilovolts. Characteristics of the voltage supplies are shown in the pictures 36. These were measured using the high voltage probe Agilent N2771A. This device must be well grounded, every other operation imposes major safety issues. This is why the voltage between the MCP plates (2kV) cannot be measured directly.

We use a voltage divider at the voltage supply for the MCP to get -2000 V at the front plate of the MCP and -500 V at the backplate. The voltage ratio determines the resulting gain and the voltage between front and back plate determines the so called strip current $I_s = \frac{U}{R_1+R_2}$, which is directly connected to the deadtime τ_{dead} of the MCP by $\tau_{dead} = Q_{out}/I_s$. The voltage supplies have the option to control the output voltage by a voltage between 0V and 10V, furthermore the actual output can be monitored by a monitor voltage between 0V and 10V. They need a supply voltage of 24V, which is delivered by a lab voltage supply.

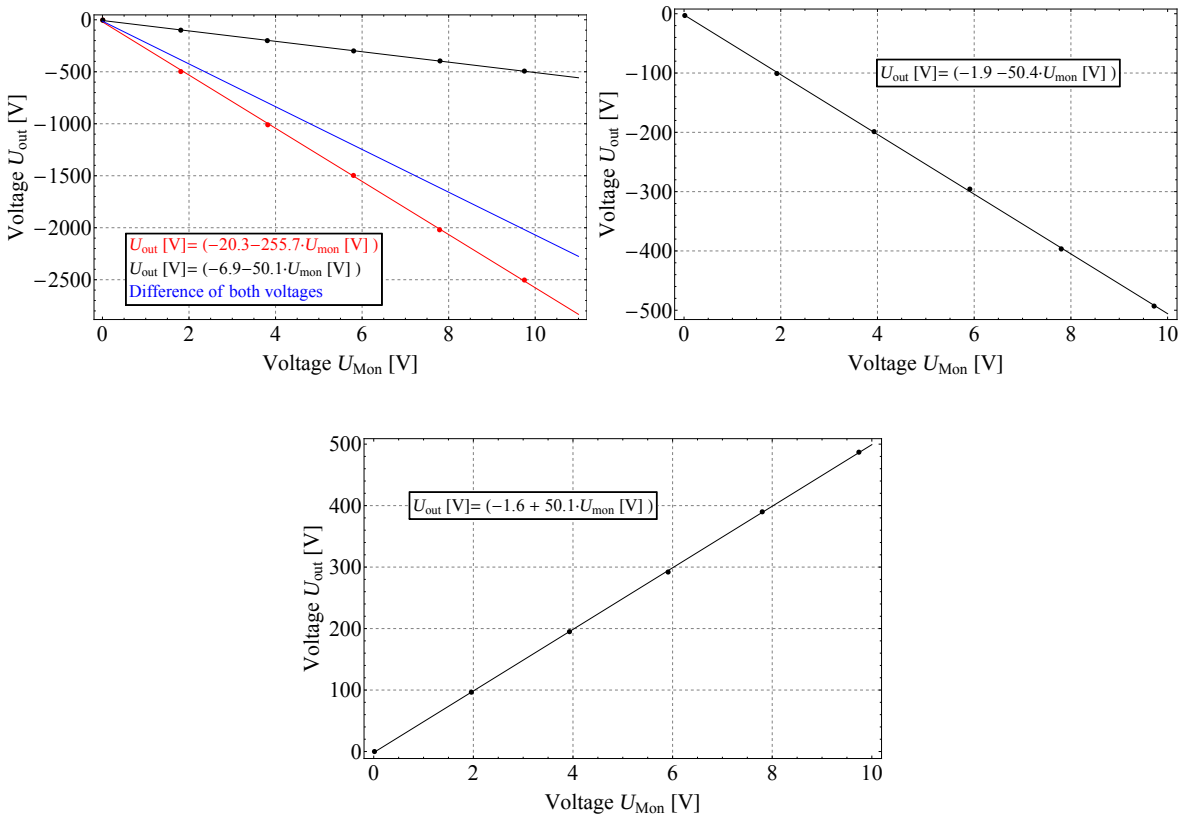

Figure 36: Top, Left: Voltage supply for the MCP, Top, Right: Voltage supply for steering plate 9, Bottom: Voltage supply for ionization with plates 2 and 6.

4.7.2. Assembly of the MCP

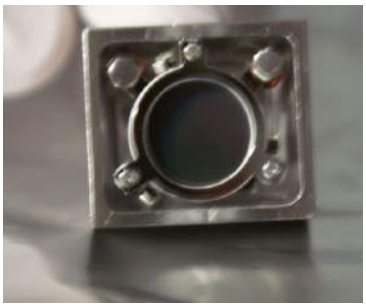

Figure 37: Assembled MCP.

The whole MCP is mounted inside a small metal box, where the original baseplate has been replaced by the backwall of the box of the same thickness. On the backwall a BNC connector with the anode is being mounted. A specially for vacuum designed BNC cable [FTAKCBM2CM12] from Kurt J. Lesker connects the MCP to a BNC-BNC feedthrough [IFDBG012032M]. The two supply voltages are delivered by two Kapton insulated copper wires of 1.1 mm thickness [FTAK10010]. These wires are clamped with screws to the lashes of the MCP-In and MCP-Out leads and lead through two holes in the back of the metal box. For protection two ceramic tubes are put between hole walls and wires.

4.7.3. Mesh

Figure 38: The finished mesh.

In order to avoid unwanted strayfields from the MCP (or the channeltron respectively) we constructed a mesh, which is placed directly in front of the MCP. The mesh consists of twelve wires made from the alloy 1.4404 (316L) with a diameter of 0.25 mm [GoodFellow]. The wire can take forces of around 5 kg. This was measured with a torque wrench and a M6 screw. The force this wire can take is surprisingly small, mainly due to the fact that the wire was made by cold work and is therefore very brittle. The wires were tightened with clamping jaws and some weights. Underneath the clamping jaws a 0.3 mm thick copper band was placed, which helps to fix the wires. Afterwards we tested the tension of the wires with an electrode in a distance of 6 mm to the mesh and an applied voltage of 0-10 kV. In between the electrode and the mesh there was a plexiglass plate of 6 mm thickness placed. As there was no visible bending of the wires observable, we conclude, that the position of the wires should be unaffected by the electric field of the MCP. During the assembly we decided to leave out two inner wires, which has only a slight effect on the electric field compensation and the ion lensing but decreases the amount of ions being absorbed on the wires. The whole mesh was cleaned afterwards again with acetone and isopropanol.

4.7.4. Characterization of the MCP

Remark: In order to avoid dangerous voltage peaks at the measurement devices caused by malfunction of the MCP or the channeltron one should use two antiparallel diodes, which break through at a specific voltage or use a simple operational amplifier, which breaks as soon as a specific voltage is being exceeded.

Before the MCP was operated the first time, the electric continuity was tested and the strip current was measured at a pressure of $1.2 \cdot 10^{-7}$ mbar by applying a voltage in small steps from 0 V to 500 V between the front and back plate and measuring the current with the Keithley 2701. A plot of the measurement is shown in figure 39.

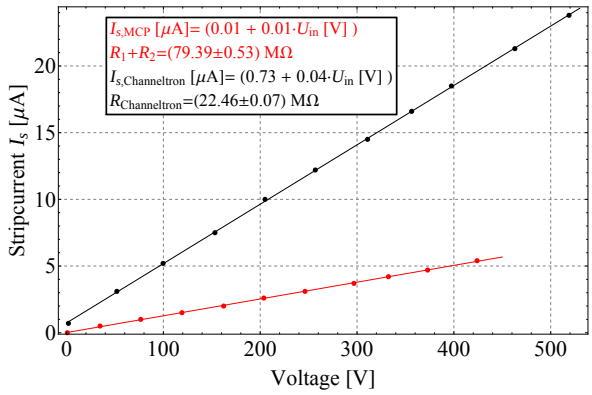

Figure 39: Stripcurrent between front- and backplate of the MCP (Red) and of the channeltron (Black).

The combined resistance of the two plates is (79.4 ± 0.5) MΩ, which is different from the specified value of 53 MΩ but still of the same magnitude. Afterwards the MCP was operated regularly and some hundred dark counts were recorded with the LeCroy Waverunner 640 Zi (4.0 GHz, 40 GS/s). It could be observed, that the operation caused a slight increase in pressure, since the MCP is heating up during operation. In this case from $1.0 \cdot 10^{-7}$ mbar to $1.2 \cdot 10^{-7}$ mbar. Some randomly chosen traces of the darkcounts recorded are shown in figure 40.

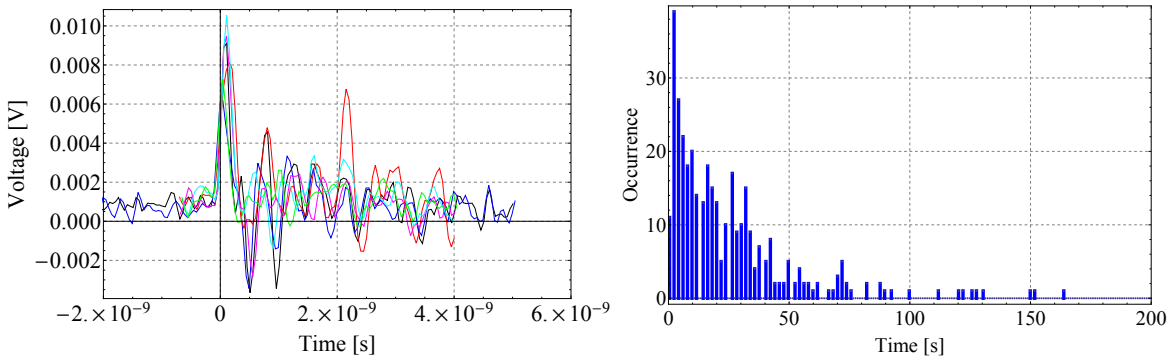

Figure 40: Left: Some randomly chosen example traces, Right: Darkcount statistics of the MCP.

The average duration of the first pulse is $(6.9 \pm 1.6) \cdot 10^{-10}$ s with a rise time of $(3.6 \pm 1.8) \cdot 10^{-10}$ s and a falling time of $(3.4 \pm 1.6) \cdot 10^{-10}$ s. The darkcounts are caused by electric field emissions from the channel walls, ionization of residual gas, local discharge and photoelectron emission caused by electric field scintillation of the MCP support paths [55].

The darkcount rate turns out to be extremly low: (0.038 ± 0.006) counts/s, compared to 0.44 counts$/(\mathrm{s} \cdot \mathrm{cm}^2) \longrightarrow 0.73$ counts/s as specified in the datasheet, which is mainly because of the magnitudes lower pressure being used [58]. A plot of the dark count statistics is shown in figure 40. It will be interesting to see, whether this darkcount rate changes, when the Rb-dispensers are in place and the MCP gets polluted with Rubidium. As can be seen in the time traces, every count is followed by a comparatively long trace of oscillations, the so called ringing. The period of this ringing is $(5.2 \pm 0.5) \cdot 10^{-10}$ s and the decay time, to which the amplitude of the oscillation has decreased to 1/e of the initial amplitude is $(1.3 \pm 0.2) \cdot 10^{-9}$ s. Another characteristic plot of MCPs is the pulse height distribution, shown in figure 41.

This distribution depends heavily on the type of MCP and on the correct angle between the two MCP plates. If the channels are aligned, then this distribution has an exponential shape. For correct alignment, this exponential shape changes into a quasi-gaussian shape. The reason for this is the space charge saturation. It is not possible to achieve arbitrary high gains since the electrostatic repulsion between the electrons limits an arbitrary high production of secondary electrons. A measure for the pulse height dispersion is the pulse height resolution PHR=FWHM/A, defined as the ratio between the full width half maximum of the pulse height distribution to the maximum amplitude achieved for highest gain [55]. In our case this is $PHR \lesssim 50\%$ compared to PHR=108% specified in the datasheet. A reason for this can of course be the rather poor statistics, since only 400 counts could successfully be recorded.

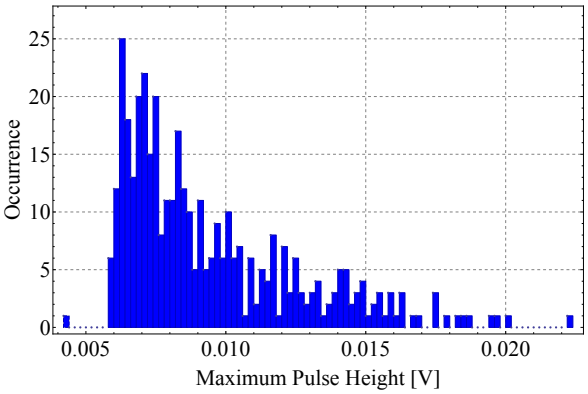

Figure 41: Pulse height resolution of the MCP.

4.7.5. Channeltron

The second one of our ion detectors is the channeltron CEM 5901 Magnum from Photonis [60]. This channeltron consists of six twisted channels, which are each made from Burle glass coated with a conducting and a semiconducting layer. The channels are twisted to prevent ion feedback. Additionally the larger surface area prolonges the lifetime of the device [59]. A schematic of this configuration is shown in figure 42. The channeltron has a small nonconducting ring at about the middle of the device. Everything said about the MCP applies similarly to channeltrons.
This channeltron is designed for pulse counting and cannot be used for analog signal detection, not even by turning the supply voltage down.

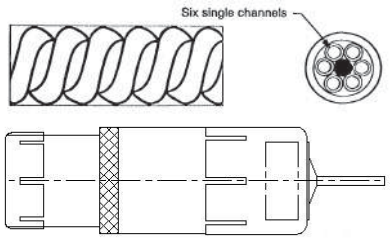

Figure 42: Schematic of the twisted channels in a channeltron and technical outline of the Magnum electron multiplier. Taken from [59].

4.7.6. Assembly of the channeltron

The channeltron is mounted in a box, which consists of two parts in between which, the channeltron is clamped at the nonconducting zone. Like in the case of the MCP, the supply voltages for the channeltron are provided by two copper wires. The signal is fed to the core of a stripped BNC cable by clamping the signal pin of the channeltron to the wire with a barrel connector. The channeltron has been cleaned in acetone and isopranol. After the whole assembly, we became aware, that it is adviced to bake it afterwards at 80 °C for at least 15

minutes [59]. Missing this step may have led to increasing dark count rates, which should go away after outgassing for long enough time.

4.7.7. Characterization of the channeltron

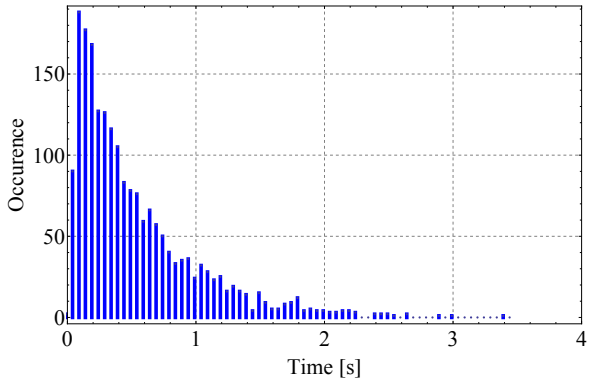

Figure 43: Darkcount statistics of the channeltron.

We characterized the channeltron in the same manner like the MCP. The stripcurrent is shown in figure 39. The resistance of the channeltron is (22.47 ± 0.07) MΩ.
Some sample traces using no amplifier and using the operational amplifier ZX60-14012L-S+ from Mini-Circuits, which is a broadband amplifier (300 kHz to 14 GHz) with a gain of up to 10 dBm, are shown in figure 44.

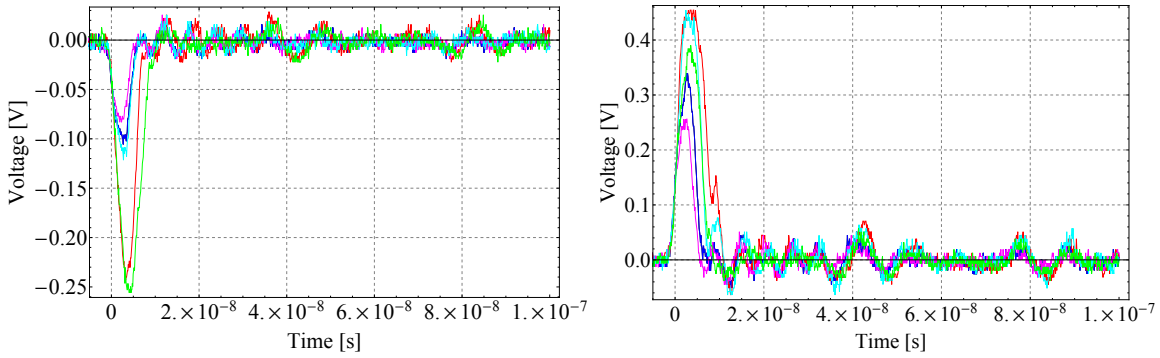

Figure 44: Left: Some randomly chosen example traces with no amplifier, Right: Sample traces using the ZX60-14012L-S+.

This signal is in either case suitable to be detected with our TimeTagger modules, which are fast digital signal counters. The rise time of the first pulse is between $2.5 \cdot 10^{-9}$ s and $11.3 \cdot 10^{-9}$ s, depending on the pulse height. The fall time is between $3.7 \cdot 10^{-9}$ s and $15.4 \cdot 10^{-9}$ s. The full pulse has an average duration of $(11.7 \pm 3.0) \cdot 10^{-9}$ s. The decay time of the ringing is $(1.3 \pm 0.4) \cdot 10^{-7}$ s with a period of $(2.8 \pm 0.7) \cdot 10^{-9}$ s, which is in this case not so crucial compared to the MCP, since we can simply set a threshold level at the TimeTagger.
The dark count statistics are shown for the unamplified case in figure 43. The dark count rate for the channeltron is very high: (1.426 ± 0.002) counts/s compared to one count per minute given by the specsheet. This tremendous increase is very likely because of the cleaning procedure. Further outgassing will reduce the dark count rate.
The pulse height distribution shows two peaks, which becomes even more obvious in the amplified case. This could be either due to two dark counts, which would mean, that the channeltron is suitable for analog counting though. Or it is because of ion feedback. The two distributions are shown in figure 45. The pulse height resolution can be estimated to

$PHR \approx 54\%$. Below in table 3, all measured and specified characteristics are shown again for the MCP and the channeltron.

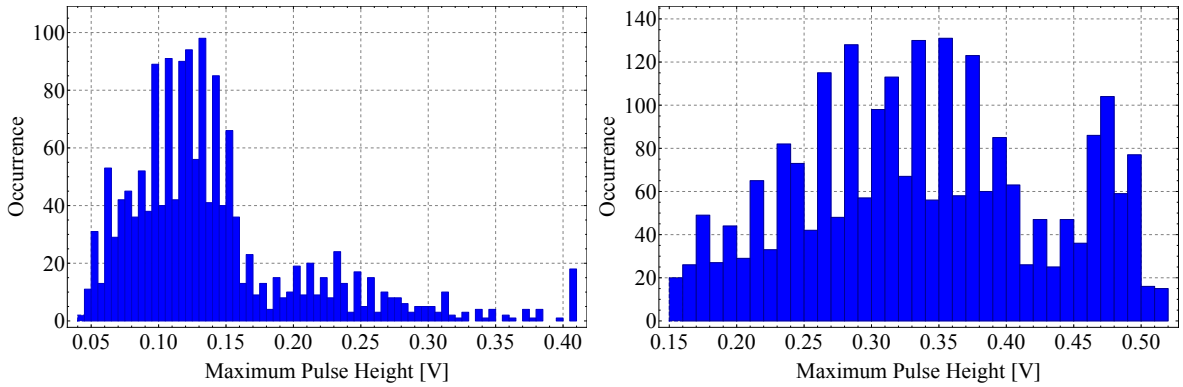

Figure 45: Left: Pulse height distribution without amplifier, Right: Distribution using the ZX60-14012L-S+.

DataType	MCP		Channeltron	
	Measured	SpecSheet	Measured	SpecSheet
Gain	-	$1.0 \cdot 10^6$	-	$5.8 \cdot 10^7$
Resistance	(79.4 ± 0.5) MΩ	57.3 MΩ	(22.47 ± 0.07) MΩ	17.12 MΩ
Mean Pulse Height	9.42 mV	-	14.12 mV	-
Darkcount Rate	(0.038 ± 0.006) cts/s	0.73 cts/s	(1.426 ± 0.002) cts/s	≤ 1 cts/min
Pulselength	$(6.9 \pm 1.6) \cdot 10^{-10}$ s	$\approx 5 \cdot 10^{-10}$ s	$(11.7 \pm 3.0) \cdot 10^{-9}$ s	-
Rise time	$(3.6 \pm 1.8) \cdot 10^{-10}$ s	-	$(2.5 - 11.3) \cdot 10^{-9}$ s	-
Fall time	$(3.4 \pm 1.6) \cdot 10^{-10}$ s	-	$(3.7 - 15.4) \cdot 10^{-9}$ s	-
Ringing: Period	$(5.2 \pm 0.5) \cdot 10^{-10}$ s	-	$(2.8 \pm 0.7) \cdot 10^{-9}$ s	-
Ringing: Decay	$(1.3 \pm 0.2) \cdot 10^{-9}$ s	-	$(1.3 \pm 0.4) \cdot 10^{-7}$ s	-
PHR	$\approx 50\%$	108%	54%	$\leq 70\%$

Table 3: Summary of all available characteristic values of the MCP and the channeltron.

5. Quantum State Tomography

It was already mentioned in chapter 2.1, that the introduced transistor, which is still classical, aims towards the future goal of realizing a quantum gate. This could for example be a controlled phase gate. So far we have only looked at the imaginary part of the nonlinear susceptibility. This part is responsible for the absorption, whereas the real part determines the refractive properties of the medium [31]. On resonance the source photons do not experience a phase shift, but with a gate excitation present prior to the source photons, the phase spectrum will shift by some amount given by the interaction strength between gate and source excitations. In this way a phase gate works similar to the transistor, but instead of watching the change in transmission we try to observe the switching of an additional phase.
An experiment showing a conditional phaseshift has already been performed [18]. In this experiment linearly polarized light $|V\rangle = (|\sigma^+\rangle + |\sigma^-\rangle)/\sqrt{2}$ is used for the source photons. The trick is, that the $|\sigma^-\rangle$ polarized light has a 15-times smaller Clebsch-Gordan coefficient than the $|\sigma^+\rangle$ light. It is therefore nearly not coupled to the Rydberg level, therefore non-interacting with the medium and serves as a phase reference, whereas the $|\sigma^+\rangle$ light is coupled strongly to the Rydberg level and picks up some phase with respect to the $|\sigma^-\rangle$ light. The phase difference of those two components translates directly into a rotation of the polarization, which can be measured with quantum state tomography.
Quantum state tomography is the process by which a full mathematical description of the state of a system can be obtained.
In classical mechanics it is always possible to find a set of measurements, which fully reconstructs the state of a system, e.g. the position and momentum of a particle. Due to the Heisenberg uncertainty relation and the no-cloning theorem this is inherently harder in quantum mechanics. Every measurement will have some back-action on the system under observation inevitably changing the state of the system. It is also impossible to simply make perfect copies of the system without knowing the state beforehand [19].
The only possibility to determine the quantum state is to prepare a large amount of identical systems and to perform different measurements on each of them. With every measurement being the projection of the state onto one of the eigenvectors of the state space, the state can be reconstructed. This method is called quantum state tomography [61].
To proof the creation of a controlled phase gate one must even go one step further. It is not enough to characterize one possible outgoing state, but one has to characterize the response of the gate on every kind of ingoing state in order to reconstruct the linear map, which maps an ingoing state on a different outgoing state. This is called quantum process tomography [62].

5.1. Quantum States

5.1.1. Density matrix

For quantum states, which are not completely known or are mixtures of projectors onto pure states $|\psi_i\rangle$ with a probability P_i, the description of the state with state vectors is no longer convenient. Instead one uses the density matrix, defined as

$$\rho = \sum_i P_i |\psi_i\rangle\langle\psi_i|. \tag{15}$$

Expectation values of an operator $\hat{O}$ can be retrieved from $\langle\hat{O}\rangle = \mathrm{tr}(\hat{O}\rho)$ and the probability P_i of measuring state $|\psi_i\rangle$ is given by the expectation value of ρ:

$$P_i = \langle\psi_i|\rho|\psi_i\rangle = \mathrm{tr}(|\psi_i\rangle\langle\psi_i|\rho) \tag{16}$$

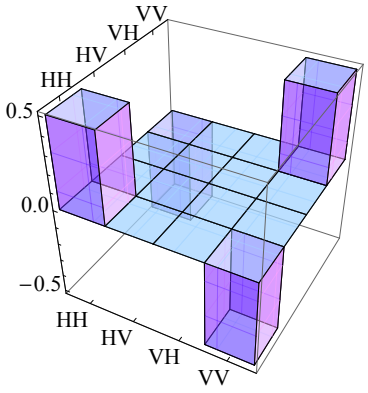

Figure 46: Depiction of the density matrix of the $|\phi^-\rangle$ state.

An operator is called a density matrix, if it fulfills the following conditions:

- $\rho^\dagger = \rho$: Hermitian $\Longleftrightarrow$ Time-reversability
- $\mathrm{tr}(\rho) = 1$: Trace is equal to one $\Longleftrightarrow$ Normalization
- $\rho \geq 0$: Positive semidefinite $\Longleftrightarrow$ Physicality

A pure state, which is a state that can be described by one single state vector, fulfills the condition $\rho^2 = \rho$ and consequently $\mathrm{tr}(\rho^2) = 1$. In this case the density matrix $\rho = |\psi\rangle\langle\psi|$ is equal to the projector onto the state $|\psi\rangle$.

5.1.2. Entanglement, environment and decoherence

With this description of a quantum mechanical state one can easily give the full mathematical description of a composite system in the Hilbert space $H_A \otimes H_B$. A system is called separable, if it is a product state, i.e. $|\psi\rangle = |\psi_A\rangle \otimes |\psi_B\rangle$. A state, which is not separable is sometimes also called entangled. For example the Bell states are fully entangled two-qubit states:

$$|\psi^\pm\rangle = (|HV\rangle \pm |VH\rangle)/\sqrt{2} \tag{17}$$

$$|\phi^\pm\rangle = (|HH\rangle \pm |VV\rangle)/\sqrt{2} \tag{18}$$

Using $|H\rangle = \begin{pmatrix}1\\0\end{pmatrix}$ and $|V\rangle = \begin{pmatrix}0\\1\end{pmatrix}$, the density matrix for the $|\phi\rangle^-$ state can be given as:

$$\rho = |\phi^-\rangle\langle\phi^-| = \frac{1}{2}\begin{pmatrix}1&0&0&-1\\0&0&0&0\\0&0&0&0\\-1&0&0&1\end{pmatrix}. \tag{19}$$

Although the trace of the density matrix squared is equal to one, the trace of the density matrix of the subsystem $\rho_{(1)} = \mathrm{tr}_{(2)}(\rho) \Rightarrow \mathrm{tr}(\rho_{(1)}^2) = 0.5$ is not equal to one, but instead the subsystem is completely mixed and therefore unknown.
From this consideration one can already conclude, that measuring a mixed state is like measuring only one subsystem of a larger entangled state. In practice a system is always interacting with the environment, which can be modelled as the system being entangled with a qubit to which we do not have any access. From this point of view, decoherence and entanglement with the environment are the same.

5.1.3. Polarization

Throughout this work single qubits will be encoded in the electric field polarization of photons with horizontal polarization $|H\rangle = |0\rangle$, vertical polarization $|V\rangle = |1\rangle$. All pure polarization states can be constructed from coherent superpositions of these two basis states:

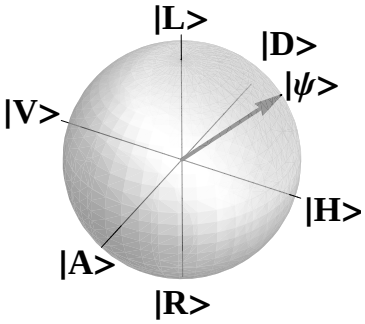

Figure 47: Plot of the Poincaré sphere.

$$|H\rangle = |0\rangle \tag{20}$$
$$|V\rangle = |1\rangle \tag{21}$$
$$|D\rangle = (|H\rangle + |V\rangle)/\sqrt{2} \tag{22}$$
$$|A\rangle = (|H\rangle - |V\rangle)/\sqrt{2} \tag{23}$$
$$|L\rangle = (|H\rangle + i|V\rangle)/\sqrt{2} \tag{24}$$
$$|R\rangle = (|H\rangle - i|V\rangle)/\sqrt{2} \tag{25}$$

There is a very concrete illustration of the polarization by means of the Poincaré sphere. The density matrix can be decomposed in the form [19]

$$\rho = \frac{1}{2}\sum_{i=0}^{3} S_i \sigma_i \tag{26}$$

with $\underline{\underline{\sigma}}$ being the Pauli matrices

$$\sigma_0 = \begin{pmatrix} 1 & 0 \\ 0 & 1 \end{pmatrix}, \sigma_1 = \begin{pmatrix} 0 & 1 \\ 1 & 0 \end{pmatrix}, \sigma_2 = \begin{pmatrix} 0 & -i \\ i & 0 \end{pmatrix}, \sigma_3 = \begin{pmatrix} 1 & 0 \\ 0 & -1 \end{pmatrix} \tag{27}$$

and $\underline{S}$ being the Stokes vector

$$S_i = \mathrm{tr}(\sigma_i \rho). \tag{28}$$

The vector (S_1, S_2, S_3) shows the direction of the polarization on the Poincaré sphere, like it is shown in figure 47 and S_0 is with the right normalization equal to one. The S_i are given by the

outcome of two projection measurements onto the states (20)-(25):

$$S_0 = P_{|H\rangle} + P_{|V\rangle} = I_{|H\rangle} + I_{|V\rangle} \tag{29}$$
$$S_1 = P_{|H\rangle} - P_{|V\rangle} = I_{|H\rangle} - I_{|V\rangle} \tag{30}$$
$$S_2 = P_{(|H\rangle+|V\rangle)/\sqrt{2}} - P_{(|H\rangle-|V\rangle)/\sqrt{2}} = I_{|D\rangle} - I_{|A\rangle} \tag{31}$$
$$S_3 = P_{(|H\rangle+i|V\rangle)/\sqrt{2}} - P_{(|H\rangle-i|V\rangle)/\sqrt{2}} = I_{|L\rangle} - I_{|R\rangle} \tag{32}$$

The probability $P_{|\psi\rangle}$ of measuring a state $|\psi\rangle$ corresponds classically to measuring an intensity $I_{|\psi\rangle}$.

5.1.4. Distance, fidelity and entropy

In quantum information a lot of different measures are known to characterize the quality of a state or an operation. Some of the most used are introduced here.

Distance: The first is the trace distance between two states ρ and σ, defined as:

$$D(\rho,\sigma) = \frac{1}{2}\mathrm{tr}(|\rho-\sigma|). \tag{33}$$

For single qubits with Stokes vectors $\underline{S}$ and $\underline{R}$, this is simply half of the Euclidian distance $D(\rho,\sigma) = \frac{1}{2}|\underline{S}-\underline{R}|$. Therefore it can be interpreted as the distinguishability between two states. The trace distance is a metric, which is convex on the space of density operators and acts in general contractive under any quantum operation [19]. The absolute value of a matrix is defined as $|\sigma| = \sqrt{\sigma\sigma^\dagger}$.

Fidelity: The fidelity defined as

$$F(\rho,\sigma) = \mathrm{tr}\left(\sqrt{\sqrt{\rho}\sigma\sqrt{\rho}}\right) \tag{34}$$

is not a metric on the space of density operators, as will become clear in chapter 5.4. This monotonic and concave measure quantifies the quality of a state, but has no direct physical meaning like the trace distance. Instead it has some mathematical properties, which are useful. For example the following holds:

$$1 - F(\rho,\sigma) \leq D(\rho,\sigma) \leq \sqrt{1-F(\rho,\sigma)^2} \tag{35}$$

Pure states satisfy the equation $D(|S\rangle,|R\rangle) = \sqrt{1-F(|S\rangle,|R\rangle)^2}$. Note, that for commuting states $\rho = \sum_i P_i|\psi_i\rangle\langle\psi_i|$ and $\tau = \sum_i T_i|\phi_i\rangle\langle\phi_i|$, the fidelity reduces to the classical fidelity $F(\rho,\tau) = \sum_i \sqrt{P_i T_i} = F(P_i,T_i)$ [19].

Von Neumann entropy: In order to quantify the uncertainty in the measurement of a state ρ, one defines the von Neumann entropy as

$$S(\rho) = -\mathrm{tr}(\rho \cdot \log_2(\rho)) = -\sum_i \rho_i \cdot \log_2(\rho_i), \tag{36}$$

where the ρ_i are the eigenvalues of the density matrix ρ. The entropy is for a completely mixed d-dimensional state at maximum $\log_2(d)$. It is a measure for the mixedness or decoherence of a state [19].

5.1.5. Measurement idea

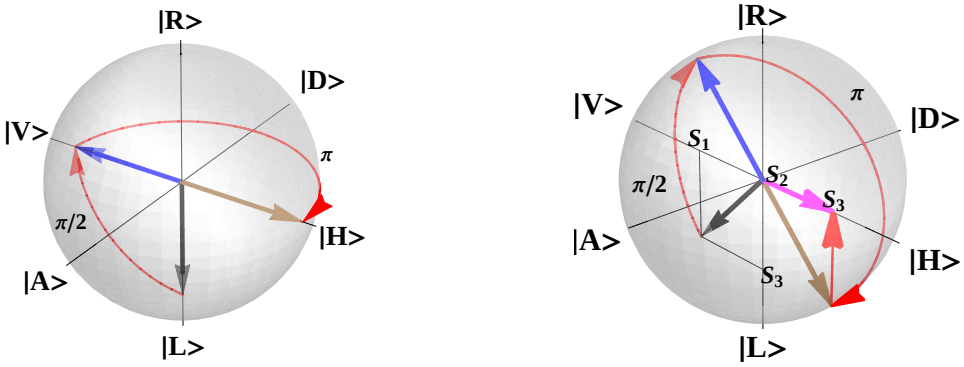

Figure 48: Measurement idea: The waveplates are set such, that $|L\rangle$ (black arrow) gets first rotated by a $\pi/2$-waveplate into the $|H\rangle - |D\rangle$ plane (blue arrow) and then by a π-waveplate into the $|H\rangle$ direction (brown arrow). The resulting state gets then projected onto the $|H\rangle$ and $|V\rangle$ axis (pink arrow). For an arbitrary state the same operation with the same waveplate settings corresponds to determining S_3 by measuring $I_{|H\rangle} - I_{|V\rangle}$. The red arrows show only the order of operations not the trajectory.

We recall that in the single qubit case the density matrix can be represented as $\rho = \frac{1}{2}\sum_{i=0}^{3} S_i\sigma_i$. That means, for determining ρ we need to make three complete measurements of S_1, S_2, S_3 in the $|H\rangle, |D\rangle$ and $|L\rangle$ bases. This can be done by rotating the k-th component of the incoming state with π- and $\pi/2$-waveplates in the $|H\rangle$ direction and then by projecting the resulting state with a polarizing beamsplitter onto the $|H\rangle$ and $|V\rangle$ axis respectively. This is illustrated in figure 48.
These rotations correspond in the mathematical sense to unitary operations $U_\Delta(\theta)$

$$U_\Delta(\theta) = \begin{bmatrix} \cos(\theta)^2 + e^{i\cdot\Delta}\sin(\theta)^2 & \cos(\theta)\sin(\theta) - e^{i\cdot\Delta}\cos(\theta)\sin(\theta) \\ \cos(\theta)\sin(\theta) - e^{i\cdot\Delta}\cos(\theta)\sin(\theta) & e^{i\cdot\Delta}\cos(\theta)^2 + \sin(\theta)^2 \end{bmatrix}, \tag{37}$$

where θ is the angle of the waveplate to the horizontal with retardation Δ. The whole unitary transformation for the ν-th measurement is given by

$$U_\nu = U_\pi(\theta_{\pi,\nu})U_{\pi/2}(\theta_{\pi/2,\nu}) \tag{38}$$

For n qubits we procede like in the single qubit case, by projecting the state in a sequence of separable bases. The unitary transformation is in this case given by

$$U_\nu = {}^1U_\nu \otimes {}^2U_\nu \otimes \ldots \otimes {}^nU_\nu \tag{39}$$

The number of counts, that we actually measure for the ν-th measurement setting at the r-th detector pair, which projects the incoming state into the canonical basis state $|r\rangle$ with initial intensity I_0 is given by [61]

$$n_{\nu,r} = I_0 \cdot \mathrm{tr}(M_{\nu,r} \cdot \rho) \quad \text{and} \tag{40}$$

$$M_{\nu,r} = U_\nu^\dagger |r\rangle \langle r| U_\nu. \tag{41}$$

5.1.6. Amount of measurements, n- vs. 2n-detectors

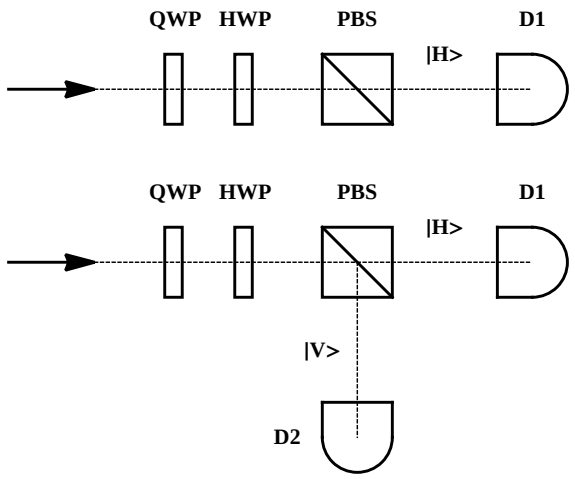

Figure 49: Top: Measurement apparatus for the n-detector setup, Bottom: Measurement apparatus for the 2n-detector setup.

A n-qubit state has 4^n Stokes parameters, which are given by 2^n probabilities. Therefore, $4^n \times 2^n$ measurements are required to determine a n-qubit state. These $4^n \times 2^n$ measurements are of course linearly dependent, since the density matrix consists of 4^n parameters, from which one is already given by the normalization constraint.

This is why $4^n - 1$ parameters have to be determined by 2^n measurements each. Having a closer look at the actual parameters one recognizes apart from the normalization further redundancies, like:

$$S_{2,2} = P_{|RR\rangle} - P_{|RL\rangle} - P_{|LR\rangle} + P_{|LL\rangle} \tag{42}$$

$$S_{0,2} = P_{|RR\rangle} + P_{|RL\rangle} - P_{|LR\rangle} - P_{|LL\rangle} \tag{43}$$

One can also say, that from the additional constraint $\rho^\dagger = \rho$ we only have to determine 3^n parameters with 2^n measurements. A measurement apparatus suitable for this is shown in figure 49. One can of course save qubits and therefore time by utilizing $2n$ detectors. This results then in setting 3^n times a new measurement basis with the retarders, but gaining everytime 2^n values, just enough measurements to completely determine one parameter of the density matrix.

5.2. Algorithm

5.2.1. Maximum likelihood

Statistical errors in our measurements will in general lead to illegal density matrices, which do not fulfill the requirements 5.1.1 for a physical density matrix, although the complete knowledge about the quantum state is definitely increased. This is because we try to reconstruct the quantum state from measurements done under different conditions, but on an equally prepared ensemble of states. In the spirit of the probabilistic quantum theory we do not ask the question [63]: "What state is determined by our measurement?" We rather ask: "What quantum state seems to be most likely for our measurement?"
The method of maximum likelihood estimation is a procedure, which accounts for the constraints on density matrices, namely the unitarity, normalization and the positivity. By truncating the whole Hilbert space it provides us with a physically possible quantum state.

5.2.2. Maximum likelihood algorithm

Let us assume some density matrix ρ and hence the number of photon counts $\bar{n}(\rho)$ we expect to measure given this matrix. The probability density to actually measure n counts provided, that we guessed $\bar{n}(\rho)$ is given by the conditional probability density $p(n|\bar{n}(\rho))$. If we now perform N measurements and record $n_1, n_2 \ldots n_N$ independent counts, then the joint probability density is accordingly given as product of the single conditional probabilities:

$$\mathscr{L}(n_1, n_2 \ldots n_N|\bar{n}(\rho)) = \prod_{k=1}^{N} p(n_k|\bar{n}(\rho)). \tag{44}$$

This function is called the likelihood function and quantifies the degree of belief that for a measurement yielding n_k counts, the system was really prepared in the state ρ [63]. The maximum likelihood estimator of $\bar{n}(\rho)$ is given by the maximum of the likelihood function $\mathscr{L}$ for all possible $\bar{n}$ or ρ respectively. Equivalently one can maximize the logarithm of this function as well:

$$L(\bar{n}(\rho)) = \ln(\mathscr{L}(\bar{n}(\rho))) = \sum_{k=1}^{N} \ln(p(n_k|\bar{n}(\rho))) \tag{45}$$

According to the equations (40) and (41) the number of expected counts is given by $\bar{n}_{\nu,r}(\rho) \simeq \mathrm{tr}(U_\nu^\dagger |r\rangle\langle r| U_\nu \cdot \rho)$. Since we are dealing with coherent states, we assume for the conditional probability density a Gaussian profile [61]

$$p(n|\bar{n}) \simeq \exp\left[-\frac{(\bar{n}_{\nu,r}(\rho) - n_{\nu,r})^2}{2\sigma_{\nu,r}^2}\right] = \exp\left[-\frac{(\bar{n}_{\nu,r}(\rho) - n_{\nu,r})^2}{2\bar{n}_{\nu,r}}\right]. \tag{46}$$

Inserting this equation in (45), we see, that we need to minimize

$$L(\rho) = \sum_{\nu,r}\left[\frac{(\bar{n}_{\nu,r}(\rho) - n_{\nu,r})^2}{2\bar{n}_{\nu,r}}\right] \tag{47}$$

for all $\bar{n}$ in order to find ρ.
Until now we have not taken the normalization and the positivity constraints on the density matrix into account. For a non-negative definite matrix ρ, the following holds: $\langle\psi|\rho|\psi\rangle \geq 0$ $\forall|\psi\rangle$. This constraint is satisfied by any matrix in the form $\rho = T^\dagger T$. This matrix is then also hermitian. To fulfill the normalization constraint, we simply write ρ as [61]

$$\rho = \frac{T^\dagger T}{\mathrm{tr}(T^\dagger T)}. \tag{48}$$

As mentioned before, the density matrix ρ for a n-qubit system consists of 3^n independent parameters. In order to fit the intensity of the data as well, we will use 4^n parameters and we choose T in a tri-diagonal form, which makes inverting ρ easier. In the single qubit case T has the form

$$T = \begin{pmatrix} t_1 & 0 \\ t_3 + it_4 & t_2 \end{pmatrix} \tag{49}$$

and $\rho = \frac{T^\dagger(\underline{t})T(\underline{t})}{\mathrm{tr}(T^\dagger(\underline{t})T(\underline{t}))}$. In our program we have to minimize a sum of squares in the form [61]

$$\mathscr{L}(\underline{t}) = \sum_x [f_x(\underline{t})]^2, \tag{50}$$

$$f_{\nu,r} = \frac{I_0 \cdot \mathrm{tr}\left(M_{\nu,r}T^\dagger(\underline{t})T(\underline{t})\right) - n_{\nu,r}}{\sqrt{2 \cdot I_0 \cdot \mathrm{tr}\left(M_{\nu,r}T^\dagger(\underline{t})T(\underline{t})\right)}}. \tag{51}$$

5.2.3. Quantum process tomography

The ultimate goal of our transistor experiment is to realize a phase gate. In order to characterize such a quantum gate sufficiently it is not enough to merely know the action of the gate on one input state, but instead we want to know the complete linear map E which fully describes the dynamics of our quantum system [62]

$$\rho \longrightarrow \frac{E(\rho)}{\mathrm{tr}(E(\rho))} \tag{52}$$

and maps some input state on some other output state $\rho_{in} \longrightarrow \rho_{out}$ by a linear mapping $E(\rho)$. One makes use of the operator-sum representation of E [19]. Let us assume, the input state in our quantum mechanical black box P is a product state of ρ and a fictious second system ρ_{env}, which could be the environment. This system has the basis $\{|e_i\rangle\}$ and the initial state $|e_0\rangle$. The output state of the whole system is then $P[\rho \otimes \rho_{env}]P^\dagger = P[\rho \otimes |e_0\rangle\langle e_0|]P^\dagger$. Considering only the system ρ, we have to take the partial trace:

$$E(\rho) = \mathrm{tr}_{env}\left[P[\rho \otimes |e_0\rangle\langle e_0|]P^\dagger\right] \tag{53}$$

$$= \sum_i \langle e_i|P[\rho \otimes |e_0\rangle\langle e_0|]P^\dagger|e_i\rangle \tag{54}$$

$$= \sum_i A_i \rho A_i^\dagger, \tag{55}$$

where the A_i are given as $A_i = \langle e_i|P|e_0\rangle$.
In order to measure the A_i, we spectrally decompose them into $A_i = \sum_m a_{im}\tilde{A}_m$ using a fixed basis $\{\tilde{A}_i\}$ with some complex numbers a_{im}. The linear map is then

$$E(\rho) = \sum_i \left(\sum_m a_{im}\tilde{A}_m\right)\rho\left(\sum_n a^*_{in}\tilde{A}^\dagger_n\right) \tag{56}$$

$$= \sum_{mn} \tilde{A}_m \rho \tilde{A}^\dagger_n \chi_{mn}, \tag{57}$$

with the positive, hermitian error correlation matrix $\chi_{mn} = \sum_i a_{im}a^*_{in}$.
Let us choose N^2 linearly independent basis elements ρ_j on the space of $N \times N$ matrices, for example $|n\rangle\langle m|$ with $|n\rangle, |m\rangle, |+\rangle = (|n\rangle + |m\rangle)/\sqrt{2}, |-\rangle = (|n\rangle + i|m\rangle)/\sqrt{2}$ as input states into our gate. We can determine the output states $E(|n\rangle\langle m|)$ and linear combinations of them by measuring $E(|n\rangle\langle n|), E(|m\rangle\langle m|), E(|+\rangle\langle +|), E(|-\rangle\langle -|)$ with quantum state tomography.
Because E is a linear map, the measurement result may be written as

$$E(\rho_j) = \sum_k \lambda_{jk}\rho_k. \tag{58}$$

From this λ_{jk} can be calculated. Furthermore, we are able to write down the following relation

$$\tilde{A}_m \rho_j \tilde{A}^\dagger_n = \sum_k \beta^{mn}_{jk}\rho_k. \tag{59}$$

Using this equation and the relations (58) and (57) we can write

$$\sum_k \sum_{mn} \chi_{mn}\beta^{mn}_{jk}\rho_k = \sum_k \lambda_{jk}\rho_k \Leftrightarrow \tag{60}$$

$$\sum_{mn} \chi_{mn}\beta^{mn}_{jk} = \lambda_{jk}, \tag{61}$$

which is true, due to the linearly independent ρ_k. Because we know λ and β, we are able to calculate χ, which yields in the end $E(\rho)$ from equation (57). Solving equation (61) is not straight forward. Instead we have to use the generalized inverse κ of β, which can be calculated with every common algebra program:

$$\beta^{mn}_{jk} = \sum_{st,xy} \beta^{jk}_{st}\kappa^{st}_{xy}\beta^{xy}_{mn} \tag{62}$$

$$\Longrightarrow \chi_{mn} = \sum_{jk} \kappa^{mn}_{jk}\lambda_{jk}. \tag{63}$$

Let the unitary matrix $U^\dagger$ diagonalize χ,

$$\chi_{mn} = \sum_i a_{im}a^*_{in} = \sum_{xy} U_{mx}d_x\delta_{xy}U^*_{ny}. \tag{64}$$

Comparing to $A_i = \sum_m a_{im}\tilde{A}_m$ yields

$$A_i = \sqrt{d_i}\sum_j U_{ij}\tilde{A}_j. \tag{65}$$

As an example choose the $\tilde{A}_i$ as

$$\tilde{A}_0 = \sigma_0 \tag{66}$$
$$\tilde{A}_1 = \sigma_1 \tag{67}$$
$$\tilde{A}_2 = -i\sigma_2 \tag{68}$$
$$\tilde{A}_3 = \sigma_3 \tag{69}$$

for a single qubit system. In general we need to perform d^4 measurements to determine χ, from which some are redundant, due to normalization. The resulting 12 parameters of χ in the one qubit case may be determined by four measurements with the input states $|H\rangle, |V\rangle, |D\rangle, |L\rangle$, where each yields $d^2 - 1$ values. The four matrices

$$\rho_1' = E(|H\rangle\langle H|) \tag{70}$$
$$\rho_4' = E(|V\rangle\langle V|) \tag{71}$$
$$\rho_2' = E(|D\rangle\langle D|) - iE(|L\rangle\langle L|) - (1-i)(\rho_1' + \rho_4')/2 \tag{72}$$
$$\rho_3' = E(|D\rangle\langle D|) + iE(|L\rangle\langle L|) - (1+i)(\rho_1' + \rho_4')/2 \tag{73}$$

can then be determined by state tomography. Because of the choice of the basis, we can write $\beta = \Lambda \otimes \Lambda$, with $\Lambda = \frac{1}{2}\begin{pmatrix}\sigma_0 & \sigma_1\\ \sigma_1 & \sigma_0\end{pmatrix}$ and therefore

$$\chi = \Lambda \begin{pmatrix}\rho_1' & \rho_2'\\ \rho_3' & \rho_4'\end{pmatrix}\Lambda. \tag{74}$$

Like this we are able to completely characterize the action of a single-qubit gate onto an incoming state [62].
This is just one of many other methods to characterize a quantum process [64]. Other schemes are either technically not feasible yet or are not suitable for our type of experiment.

5.2.4. Error estimation

Estimating the overall errors for polarization processes is nontrivial, because the single errors do not add up like in standard error calculation. An error made with a $\pi/2$-waveplate will not add up to the error made with a successive π-waveplate, but will be amplified. Additionally, the impact of an error of the retardation is depending on the position of the plate. For horizontally polarized light passing the waveplate along the zero axis, the error of the retardation is negligible, but will have a larger effect for a nonzero position. This is illustrated in figure 50.
For this reason, it is common not to theoretically calculate the errors, but to guess random input states, counts and retardations distributed around the actually measured values and to perform then a maximum likelihood estimation of many of those guessed states [61].

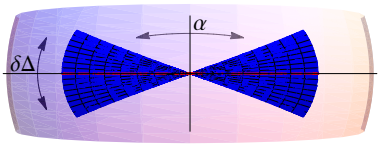

Figure 50: Section of the Poincaré sphere. Impact of the error of retardation $\delta\Delta$ on the Stokes vector depending on the angle α of the waveplate. Exaggerated depiction.

It turns out, that the error of the measurement made in the basis vector closest to the prepared state is the smallest. This is because here the greatest intensity difference can be measured in the two branches of the analysing beamsplitter. The smallest total error can be achieved by choosing the measurement basis such, that the prepared state is diagonal in one of the new measurement bases. If the first measurement yields $\rho = \lambda_1|\psi_1\rangle\langle\psi_1| + \lambda_2|\psi_2\rangle\langle\psi_2|$, then we choose the next basis as $|\psi_{3/4}\rangle = \frac{1}{2}|\psi_1\rangle \pm |\psi_2\rangle$ and $|\psi_{5/6}\rangle = \frac{1}{2}|\psi_1\rangle \pm i|\psi_2\rangle$. Like this we will always have a measurement, which yields the highest intensity difference between $|\psi_i\rangle$ and $|\psi_j\rangle$ [65].
Concerning the state preparation it turns out, that preparing for example $|R\rangle$ is more error-prone, than preparing $|V\rangle$.

5.3. Characterization of the setup

In order to make a good estimate about the counts $\bar{n}$ to be expected, we can take some properties of our setup into account. We recall, that the expected counts for the measurement in the ν-th eigenstate at the r-th detector are given as $\bar{n}_{\nu,r} = I_0 \cdot \mathrm{tr}(M_{\nu,r} \cdot \rho)$. A list of influences, which can actually be taken into account is given here and the corresponding methods and characterizations, that were performed are presented in the next chapters:

- Different detector efficiencies: $\bar{n}_{\nu,r} = I_0 \cdot E_0 \cdot E_r \cdot \mathrm{tr}(M_{\nu,r} \cdot \rho)$
- Accidental counts: $\bar{n}_{\nu,r} = I_0 \cdot E_0 \cdot E_r \cdot \mathrm{tr}(M_{\nu,r} \cdot \rho) + n^{acc}_{\nu,r}$
- Imperfect waveplates: $\bar{n}_{\nu,r} = I_0 \cdot E_0 \cdot E_r \cdot \mathrm{tr}(\tilde{M}_{\nu,r} \cdot \rho) + n^{acc}_{\nu,r}$
- Beamsplitter crosstalk: $\bar{n}_{\nu,r} = I_0 \cdot E_0 \cdot E_r \cdot \mathrm{tr}(\tilde{\tilde{M}}_{\nu,r} \cdot \rho) + n^{acc}_{\nu,r}$
- Intensity drifts: $\bar{n}_{\nu,r} = I_0 \cdot I_\nu \cdot E_0 \cdot E_r \cdot \mathrm{tr}(\tilde{\tilde{M}}_{\nu,r} \cdot \rho) + n^{acc}_{\nu,r}$

5.3.1. Setup

In order to test the tomography scheme, the code and to see how crucial the characterization of included devices and optics is, a test setup has been built to measure the classical polarization state of coherent light. The experiment consists of a DFB diode laser [EYP-DFB-0780-00080-1500-SOT02-0000] at 780 nm with an output power of 86 mW. The wavelength can be measured with a wavemeter to which the light is guided with a beamsampler and a multimode fiber. The beamsampler is used only for this purpose and detached otherwise. An OD-filter and a 50:50 beamsplitter set an appropriate laser power. In order to clean the spatial mode, the light is coupled into a single-mode fiber with polarization matching according to [66]. The output power is then 1.9 mW and the $1/e$ beamdiameter is 1.1×1.1 mm. The light is then reflected by a polarizing beamsplitter and sent through a Glan-Taylor prism to clean the vertical

polarization even more accurate. Next to it stands a π- and a $\pi/2$-waveplate to prepare a polarization state, which is then measured using another pair of π- and $\pi/2$-waveplates and another Glan-Taylor prism. The measurement waveplates are both mounted in motorized rotational mounts designed and built by the 3rd institute of physics at the university of Stuttgart. For the state tomography, the waveplates for the state preparation are mounted in standard rotational mounts and for the process tomography they are also mounted in motorized rotational stages. The result is read out in the transmitted horizontal branch of the prism with a logarithmically amplified photodiode and the oscilloscope Agilent DSOX2014A (100 MHz).

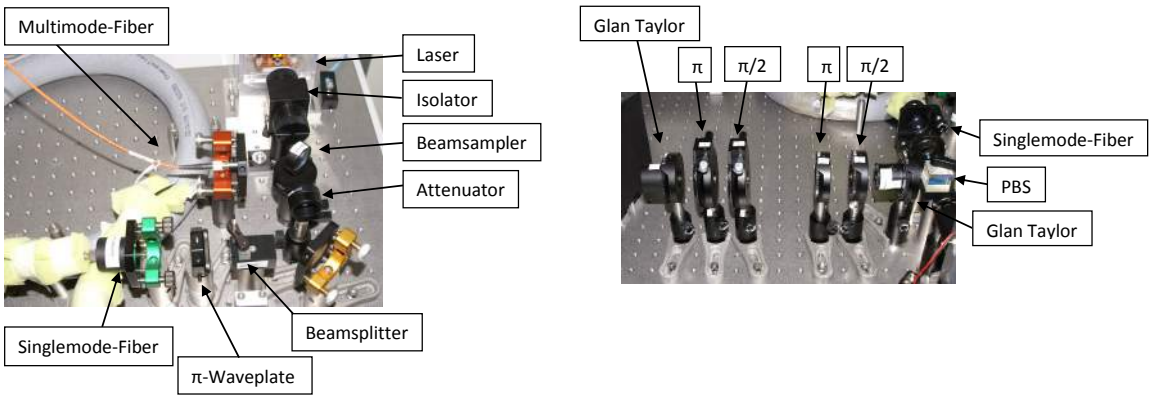

Figure 51: Left: First part of the test setup, Right: Tomography part.

5.3.2. Photodetectors

A logarithmically amplified photodiode, designed and built in the electronics workshop, has been used for most of the measurements. It contains the diode FND-100 from Thorlabs but has also the ability to plug in every other diode with SO-5 housing. The signal is amplified by the logarithmic amplifier AD8307. In this way one can measure intensities ranging over seven to eight orders of magnitude without having to change load resistors at the output of the photodiode. For the tomography this has a second advantage: All data points are recorded with the same amount of bits and in the same measurement range of the oscilloscope. The power supply was also designed by the electronics workshop and shows no distinct noise peaks, as can be seen in figure 52.

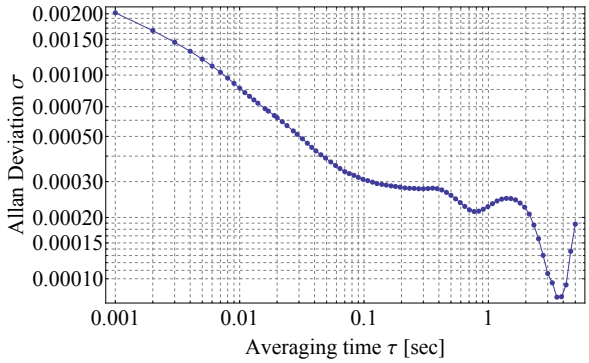

Figure 53: Allan deviation of the setup measured with the logarithmically amplified photodiode.

Allan deviation: The Allan variance [67] is a measure of the frequency stability in the time domain. It is defined as

$$\sigma_y^2(\tau) = \left\langle \frac{(\bar{y}_{k+1} - \bar{y}_k)^2}{2} \right\rangle, \qquad (75)$$

where $\bar{y}_k$ is originally defined as relative frequency error $\bar{y}_k = \langle \frac{\delta\nu}{\nu} \rangle$. We use instead simply $\bar{y}_k = I_k$ as the intensity of the k-th data point. This gives us then the stability of the

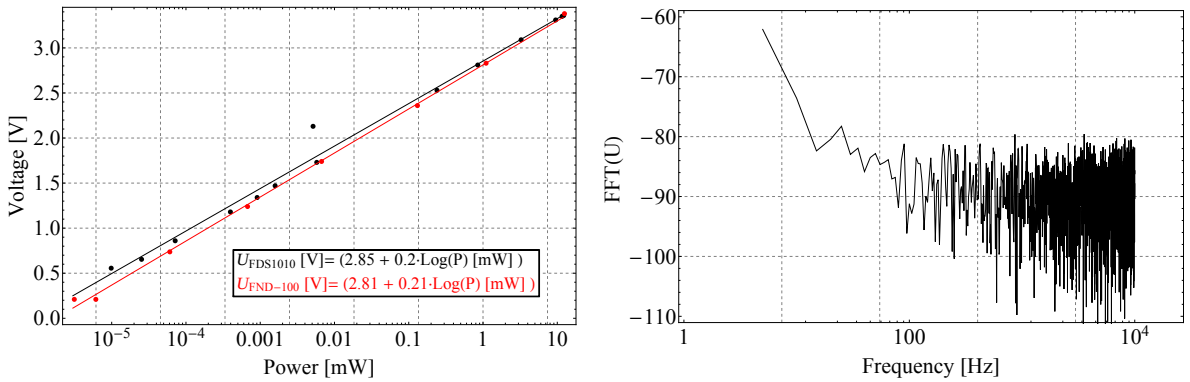

Figure 52: Left: Characteristics of the logarithmically amplified photodiode with two different diodes, Right: Fast Fourier transform of the recorded signal at a power of 12.5 mW.

intensity over time and can give good indications on what a suitable averaging time could be. A measurement of the Allan deviation $\sigma_y(\tau)$ recorded with the logarithmically amplified photodiode just after the Glan-Taylor prism is shown in figure 53. Care must be taken not to use different amounts of bits per time unit or amplitude unit, because this has direct influence on the Allan deviation. Also the last several points of the Allan deviation show an unphysical increase due to a sampling error. On the timescale of 10 seconds longterm drifts are negligible. A reasonable measurement time is one second and in this time also most of the noise on short timescales is being averaged out. This is why for all future measurements an averaging time of one second will be used.

5.3.3. Waveplates

In order to measure in a known measurement basis, one has to determine exactly the retardation of the used waveplates. The retardance of a waveplate is defined as

$$\Delta = \frac{2\pi \cdot \Delta n(\lambda) \cdot L}{\lambda}, \tag{76}$$

with $\Delta n(\lambda)$ being the difference between the ordinary and the extraordinary index of refraction and L is the thickness of the material.
Also there are combinations of waveplates, which cannot be used at all, because an incoming polarization direction cannot be rotated in every direction on the Poincaré sphere. It can be shown [61], that for two waveplates with retardations $0 \leq \phi_1 \leq \phi_2 \leq \pi$ two conditions must be fulfilled:

$$2\left|\frac{\pi}{2} - \phi_1\right| \leq \pi - \phi_2 \tag{77}$$

$$\phi_1 + \phi_2 \geq \pi. \tag{78}$$

If the first condition cannot be met, then a state $|H\rangle$ cannot be rotated to the poles, if the second condition is violated, then the Poincaré sphere has a slit in the equatorial plane. This is illustrated in figure 54.

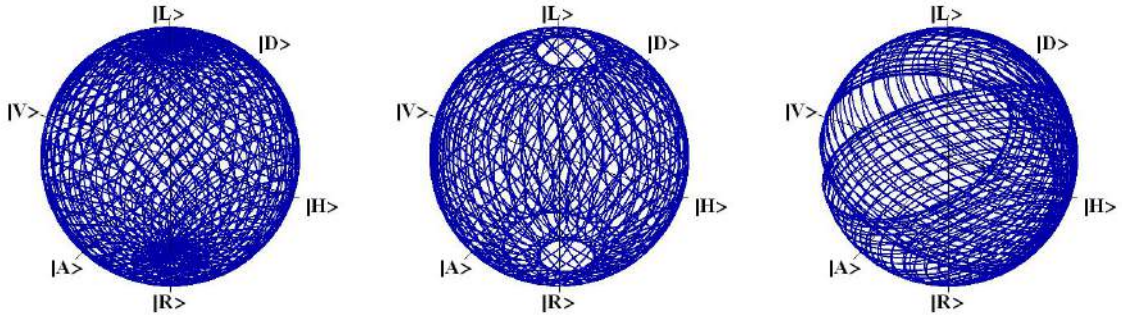

Figure 54: Result of rotating an incident polarization vector $|H\rangle$ on the Poincaré sphere with waveplates with retardations: Left: 0.955π, 0.515π, Middle: 0.95π, 0.4π, Right: 0.6π, 0.33π.

The Jones matrices of a waveplate with retardation Δ and of a polarizer are given by [61,68]

$$W(\Delta) = \begin{pmatrix} exp(-i\Delta/2) & 0 \\ 0 & exp(-i\Delta/2) \end{pmatrix}, \quad P = \begin{pmatrix} 1 & 0 \\ 0 & 0 \end{pmatrix}. \tag{79}$$

One has to transfer always in the correctly rotated frame of reference with the matrix

$$R(\theta) = \begin{pmatrix} \cos(\theta) & \sin(\theta) \\ -\sin(\theta) & \cos(\theta) \end{pmatrix}. \tag{80}$$

The output electric polarization using one polarizer at an angle of Ω_1, a waveplate at an angle θ and a second polarizer at an angle Ω_2 is given by

$$E_{out} = P \cdot R(\Omega_2) \cdot (R(-\theta) \cdot W(\Delta) \cdot R(\theta)) \cdot \begin{pmatrix} \cos(\Omega_1) \\ \sin(\Omega_1) \end{pmatrix} \tag{81}$$

The output intensity is then [68]

$$I_{out} = E_{out}^{\dagger} \cdot E_{out} = \frac{I_0}{2}(1 + A + B\cos(\Delta)) \quad \text{with} \tag{82}$$

$$A = \cos(2(\Omega_2 - \theta))\cos(2(\Omega_1 - \theta)) \tag{83}$$

$$B = \sin(2(\Omega_2 - \theta))\sin(2(\Omega_1 - \theta)). \tag{84}$$

The equation (82) can be written as a linear equation of $\cos(2\Omega_2)$ by setting the waveplate fixed to $\theta = \pi/4$ and $(\Omega_1 - \theta) = \pi/4$, then the output intensity is

$$I_{out} = \frac{I_0}{2}(1 - \cos(\Delta)\cos(2\Omega_2)), \tag{85}$$

and the retardation can be calculated from the slope m and the ordinate n of this line by [68]

$$\left(\frac{m}{n}\right) = \cos(\Delta). \tag{86}$$

With this method at hand several measurements were done. First of all, the retardation of different available waveplates was determined. The measurements are shown in figure 55.

The measurements were done with the DET100A photodiode from Thorlabs and varying load resistors to cover the whole dynamic range. The wavelength of the laser at the time of these measurements was 780.235 nm. From the results in figure 55 we chose to take the combination HP1 and QP3 for the preparation of polarization encoded states and the waveplates HP2 and QP4 for the state estimation, since those were the two pairs fulfilling the equations (77) and (78) best.

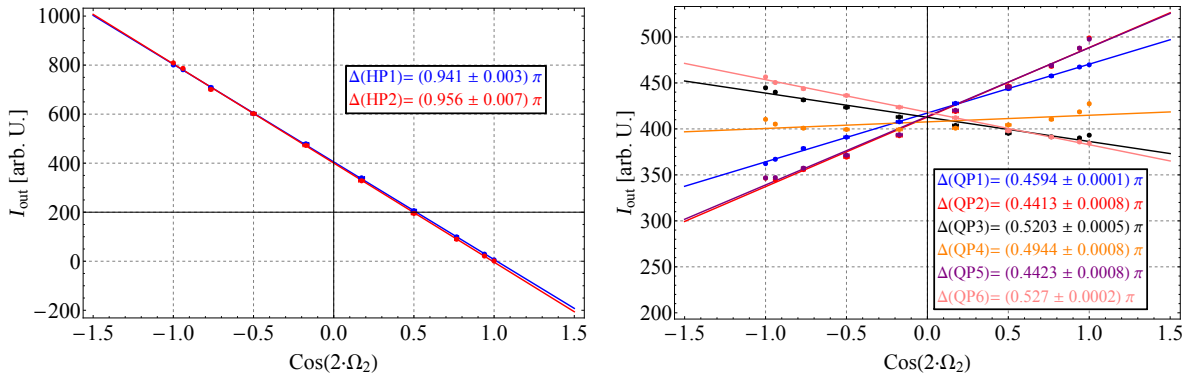

Figure 55: Left: Retardation of π-waveplates, Right: Retardation of $\pi/2$-waveplates.

In the case of a tilt of the waveplate with respect to the optical axis by an angle α, the effective thickness L of the waveplate increases to $L/\cos(\alpha)$ and therefore $\Delta_0 \longrightarrow \Delta_0/\cos(\alpha)$. This is plotted together with the measurement points in figure 56. The measurement was performed with the $\pi/2$-waveplate QP1 again at 780.235 nm. The deviation from the expected behaviour for large angles results from the refractive index of the waveplate, which deflects the beam and causes the thickness of the waveplate to be effectively smaller.

Most of the waveplates consist of quartz glass, which is in its crystalline form birefringent. The material size has of course some dependence on temperature, as does the birefringence Δn. In the most general case we can write the change of the retardation with temperature as

$$\frac{d\Delta}{dT} = \frac{2\pi}{\lambda} \cdot \Delta n \cdot L \cdot \left(\frac{1}{L}\frac{dL}{dT} + \frac{1}{\Delta n}\frac{d\Delta n}{dT} \right). \qquad (87)$$

Because a change of the birefringence with temperature will effectivly have the same impact like a change in the thickness of the plate [69], we can write $\frac{d\Delta}{dT} = \Delta \cdot \delta$ and therefore

$$\Delta = \Delta_0 \cdot exp(T \cdot \delta) \simeq \Delta_0 \cdot (1 + T \cdot \delta). \qquad (88)$$

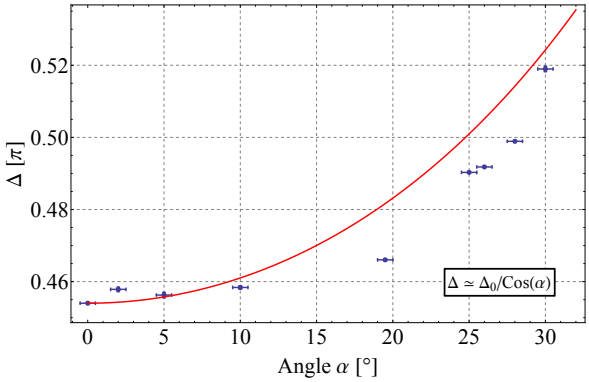

Figure 56: Retardation depending on a a tilt of the waveplate by an angle α with respect to the optical axis.

This relation was measured using a temperature controlled lenstube [SM1L10H] from Thorlabs. The result for δ is $\delta = -0.005\ \frac{1}{°C}$, which is in the same order of magnitude like the literature value $\delta_{lit} = -0.007\ \frac{1}{°C}$ [70]. The data is depicted in figure 57.

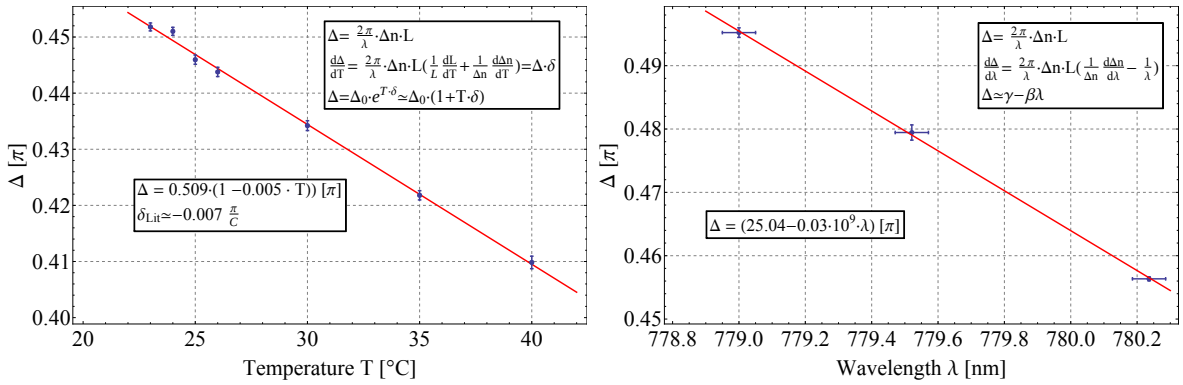

Figure 57: Left: Retardation depending on the temperature, Right: Retardation depending on the wavelength.

The retardation depends also on the wavelength. By changing the temperature and the current of the laser, the wavelength was changed and the retardation was measured. This is shown in figure 57.

In this case the retardation itself and the birefringence, through the dispersion, depend both on the wavelength. We write again the derivative of the retardance over the wavelength

$$\frac{d\Delta}{d\lambda} = \frac{2\pi}{\lambda} \cdot \Delta n \cdot L \cdot \left(\frac{1}{\Delta n} \frac{d\Delta n}{d\lambda} - \frac{1}{\lambda} \right) = \Delta \cdot (\alpha - \frac{1}{\lambda}). \tag{89}$$

Solving this differential equation yields

$$\Delta = \Delta_0 \cdot \lambda_0 \cdot \frac{exp(\alpha\lambda)}{\lambda} \simeq \gamma - \beta\lambda. \tag{90}$$

γ and β are some constants. This is just a very rough derivation, but the intention is to show merely the overall behaviour rather than a quantitatively derivation.

5.3.4. Beamsplitter

There a two types of errors, that can occur with beamsplitters. First of all they can absorb one polarization direction more than the other and second they can mix up polarizations, so that there is still a part of the $|H\rangle$ polarization coming out of the $|V\rangle$ branch and vice versa. The second is caused by scattering at the surfaces and causes depolarization in the outgoing branches. We are using the Müller formalism, since this provides the possibility of taking dephasing and loss into account. The Müller matrix for a polarizer can be given as [71]

$$T(0) = T \begin{pmatrix} 1+u+v & 1 & 0 & 0 \\ 1 & 1+u-v & 0 & 0 \\ 0 & 0 & 0 & 0 \\ 0 & 0 & 0 & 0 \end{pmatrix}, \tag{91}$$

where u and v are the ratios of copolarized and crosspolarized incoherent scattering and T is the transmittance for unpolarized light. The measured transmittance is $T^* = I/I_0 = T(1+u+v)$,

which includes the pure transmittance and the unwanted influence of scattering. The ratio of minimum to maximum transmission for linearly polarized incident light is called extinction ratio

$$E = \frac{I_{min}}{I_{max}} = \frac{u+v}{2+u+v}. \tag{92}$$

The first problem is, that the incident light is only partially polarized. Therefore we use two polarizers. One is the polarizer P and the other is the analyzer A. It can be shown [71], that the extinction of the whole assembly can then be given by

$$E = \frac{I(0,90)+I(90,0)}{I(0,0)+I(90,90)} = \frac{u_A+v_A+u_P+v_P}{2+u_A+v_A+u_P+v_P}, \tag{93}$$

and the effects of partially polarized light is cancelled out.
The next problem are the imperfect polarizers itself. To counterbalance this effect one can make three measurements with two of three polarizers, which are interchanged. The combined cross scattering is given by [71]

$$u_P+v_P+u_A+v_A = \frac{2(I(0,90)+I(90,0))}{I(0,0)+I(90,90)-I(0,90)-I(90,0)}. \tag{94}$$

With at total three sets of measurements for three pair combinations of polarizers one gets an equation system, which can be solved for the combined cross scattering $u+v$, which can then be inserted in equation (92) to get the extinction of the polarizer. This procedure is called zone average method [71]. Note, that the polarizers need to have extinction ratios of at least the same magnitude, otherwise the worst polarizer will always degrade the resulting extinction of the better polarizer.
We used three polarizers, two Glan-Taylor prisms, "GT1" and "GT2" (GT10-B) and one Wollaston prism "W" (WP10-B) all from Thorlabs. The Wollaston prism has the disadvantage, that the beams leave the device under an angle of around 10°. Although the Wollaston prism works extremly well, this beam deviation makes it very hard to align the outgoing beams. The measurement was done with the photodiode DET100A and appropriate load resistors. The incident light was "depolarized" by a $\pi/2$-waveplate, such that the transmitted intensities after the first polarizer were independent of the angular position. The data looks like this:

	GT2-GT1	W-GT2	GT1-W
$I(0,0)$ [arb. U.]	414.8	432.8	436.4
$I(90,90)$ [arb. U.]	443.5	495.6	481.2
$I(0,90)$ [arb. U.]	0.005	0.004	0.004
$I(90,0)$ [arb. U.]	0.005	0.004	0.003

From this result the extinctions

GT1	$1:176029 \longmapsto (5.7\pm0.2)\cdot10^{-6}$
GT2	$1:174985 \longmapsto (5.7\pm0.2)\cdot10^{-6}$
W	$1:402162 \longmapsto (2.5\pm0.2)\cdot10^{-6}$

can be extracted, which are in agreement with the estimated extinctions given by the manufacturers.

5.4. Test Results

5.4.1. Quantum state tomography

The tests for the state tomography were done at 780.242 nm and an input intensity of 1.83 mW. In front of all the preparation the prism $GT1$ was standing. The state preparation was done with waveplates with retardations $(0.919 \pm 0.01)\ \pi$ and $(0.483 \pm 0.001)\ \pi$ with a temperature dependence of $0.005\ \pi/°C$, from figure 57. The two waveplates were mounted in standard rotational mounts with an accuracy of 1°. The states were then characterized using two waveplates with retardations $(0.955 \pm 0.015)\ \pi$ and $(0.515 \pm 0.001)\ \pi$ mounted in rotational stepper motors with a step size of 0.06°. Several hundred measurements were done for each state, from which each complete tomography takes about 50 seconds limited by the speed of the steppermotors.
For the following discussion I will restrict myself on the measurements of the $|V\rangle$ and the $|L\rangle$ state, which serve as an example. Comparing these two states shows best the influence of errors. $|V\rangle$ shows minimal errors and $|L\rangle$ shows the largest possible errors.

Distance, fidelity and entropy From the recorded data the trace distance, the fidelity and the von Neumann entropy were extracted. For comparison the data for the $|L\rangle$ state is shown in figure 58 prepared once with only one $\pi/2-$waveplate and once prepared with a $\pi/2-$ and a $\pi-$waveplate. The fidelity of the quantum state is in both cases very large, although the trace distances of the two $|L\rangle$ states indicate differences. This is because the fidelity is no metric and therefore only limited suitable for comparative analysis.
The trace distance for the $|L\rangle$ state prepared with two waveplates is twice as large as the trace distance for the state prepared with only one waveplate. This indicates a systematic error at the preparation of the state. The trace distance is lowest for the $|V\rangle$ state, which supports the argumentation in chapter 5.2.4, that retardation errors have the lowest impact for states prepared near the initial state, which is $|V\rangle$ directly after the first Glan-Taylor prism.
Moreover, the von Neumann entropy as a measure for the decoherence of a state, is lower for the state prepared with less waveplates and is lowest for states, which do not need much preparation like the $|V\rangle$ state. The shorttime fluctuations result from the noise of the whole laser setup and the photodetector. The longterm drifts can be a result of a temperature dependent rotation of the initial polarization in the single mode fiber. The loss of perfect linearly polarized light incident on the polarizing beamsplitters could lead to increased crosstalk, which results in decoherence.

Preparation errors The data in figure 58 indicates errors occurring at the preparation, especially the comparison of states prepared with one and with two waveplates underlines this argument. In order to quantify the source of those errors, error estimations were made.
By choosing values for parameters, like the setting of the polarizer or the retardation from a limited range various presumably prepared states can be calculated from the Müller matrices of the polarizer and the waveplates. In figure 59 the results are shown. In red is the Stokes vector shown for the probably prepared state. The dots around it are the results for different parameters of the preparation optics. A setting error of 0.05°of the polarizer has only minor

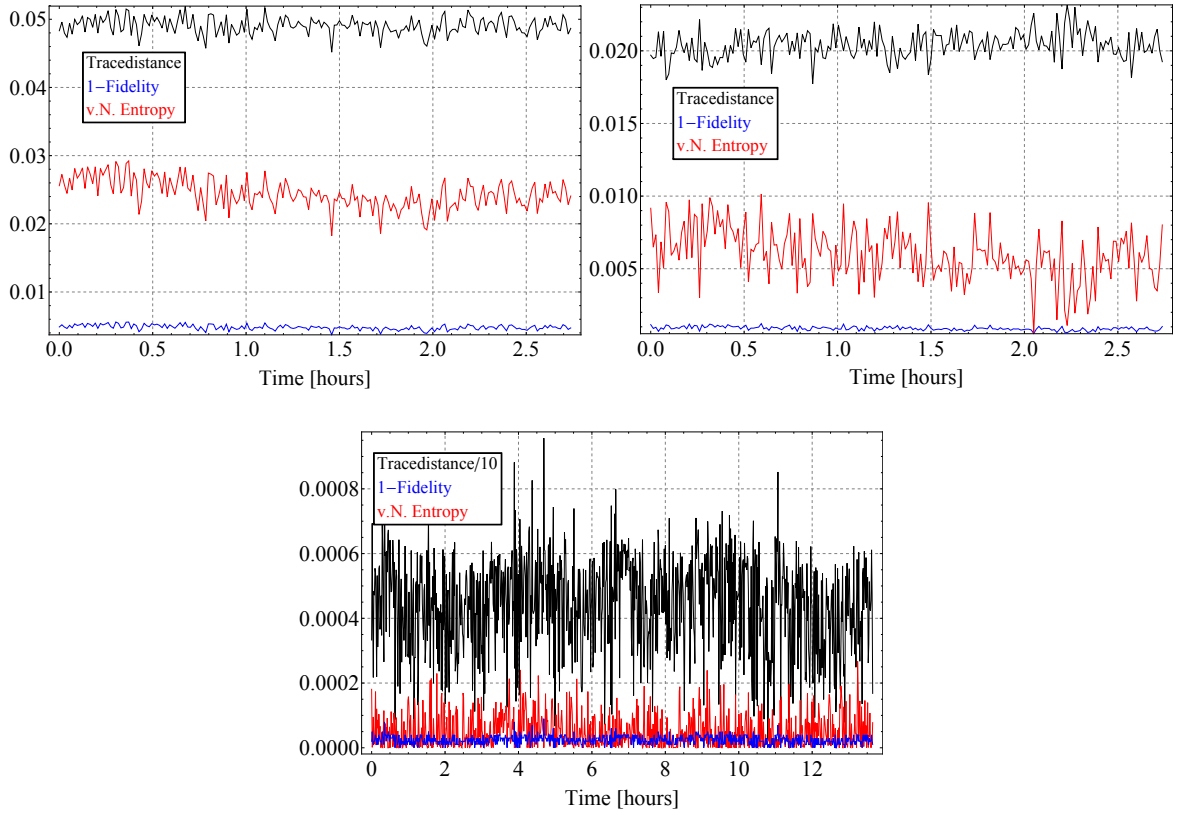

Figure 58: Trace distance, fidelity and von Neumann entropy for: Top: $|L\rangle$ state, Left: $\pi/2-$ and $\pi-$waveplate (200 runs), Right: Only $\pi/2-$waveplate (200 runs), Bottom: $|V\rangle$ state (900 runs).

impact. The effect of 0.5°misadjustement of one or both of the waveplates is already larger. Note that this estimate is very small since also the zero position of the waveplates could easily be wrong by this amount. An error of 0.01π and 0.02π of the retardation of the $\pi/2-$ and the $\pi-$waveplate caused by a faulty characterization as well as a temperature drift of < 2 °C in the lab has already a very large effect on the actually prepared state. The overall error taking all those effects into account is shown in the last figure in 59.

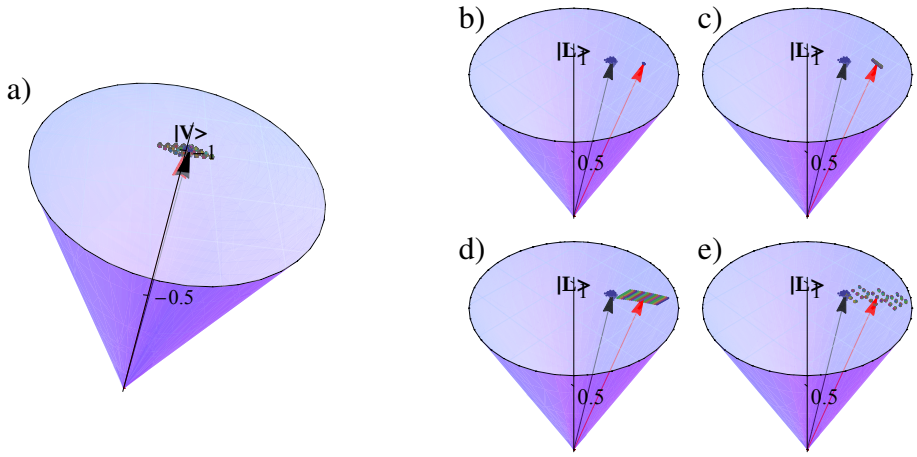

Figure 59: a): Black arrow: Measurement and error estimation of the measurement, Red arrow: Prepared state and all possible preparation errors for the $|V\rangle$ state.
b)-e): Black arrow: Measurement and error estimation of the measurement, Red arrow: Prepared state and preparation errors for the $|L\rangle$ state. b): Errors by misadjustment of the polarizing beam splitter, c): Errors by misadjustment of the waveplates, d): Errors by faulty retardation, e): All possible errors together.

The maximum trace distance among the presumably prepared states is already 0.10 and 0.06 for the $|L\rangle$ and the $|V\rangle$ state.
In order to calculate the errors of the state measurement in a similar manner a set of possible characteristic values was randomly chosen from normal distributions of the characteristic values centered around the actually measured value. For example the retardation was perturbed randomly with a Gaussian distribution with a standard deviation equal to the error. Then the likelihood estimation was performed again with those slightly changed parameter settings.
The error of the waveplate setting was set to 0.05°, which corresponds to the step size of the steppermotors, the total error of the retardation of the waveplates was set to 0.015π and the voltage error of the photodiode was set to 0.002 V. The resulting data points are shown in figure 59 at the end of the actually measured black Stokes vectors, which is the average of all tomographic measurement runs. The corresponding trace distances of the estimated errors are maximally 0.01 and 0.02 for $|V\rangle$ and $|L\rangle$ states.
The real measured fluctuations are normally a bit smaller, than the estimated errors. For the $|L\rangle$ states the average trace distance is 0.002 compared to 0.005 for the estimated errors, the trace distances between two measurements of the $|V\rangle$ states is on average 0.003 compared to 0.004 for the estimated errors.

In general, the error estimation of the measurement process is able to predict the amplitude of the measurement fluctuations. But the error estimation is not able to make a statement about the quality of the state estimation. This is visible in the huge mismatch between the trace distances of the error estimation and the actually measured trace distance between prepared and measured state, which indicates, that either the determined retardation has a larger error than assumed or temperature drifts must have taken place inbetween the characterization of the waveplates and the tomography, since the trace distances of the actual measurements is not fluctuating by this amount.
Note, that temperature changes of $1-2$ °C are common in our labs, especially during the change of seasons.
Altogether the tomography seems to work better than the preparation of the states. In general state estimation with accuracies of more than 95% are possible. This can be further improved by using zero order waveplates, which are designed such, that retardation changes due to temperature drifts are compensated. Additional monitoring of the temperature can help to identify error sources even better.

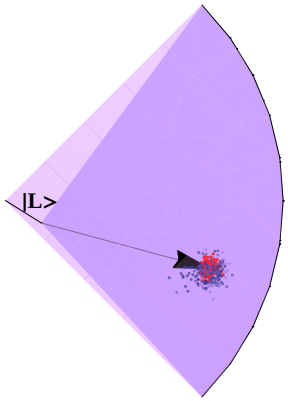

Figure 60: Errors: Blue: Measurements, Red: Simulated measurement outcomes for perturbed initial values.

Minimal phase shift The phase of the components of a state are in general given by $\arg(\rho)$. In order to calculate the minimal resolvable phase shift we assume an input state $|\psi\rangle = |H\rangle = \frac{1}{\sqrt{2}}(|R\rangle + |L\rangle)$ in the manner of [18]. This state experiences a phase shift ϕ and is therefore $|\psi'\rangle = \frac{1}{\sqrt{2}}(e^{i\phi}|R\rangle + |L\rangle)$. Calculating the trace distance of those two states yields $D(\phi) = \frac{1}{2}tr(||\psi'\rangle\langle\psi'| - |\psi\rangle\langle\psi||) = |\sin(\phi/2)|$. For states near to $|H\rangle$ the trace distance to the shifted state, which is distinguishable from $|H\rangle$, is given by the estimated errors, which was 0.004. This corresponds to a minimal phaseshift of 0.5°. The phaseshift between the presumably prepared $|L\rangle$ state and the actually measured state is 2.3°. At total the error of the phase shift is between 0.5°and 2.3°, depending on the state under observation. The actual error of the measurement will be much smaller, since we cannot circumvent taking the error of the state preparation into account as well. Similar error ranges are presented in [18]. Here the errors were between 1.7°and 3.6°. By making use of a local oscillator in a homodyne detection

scheme one can achieve errors between 0.7°and 1° [72]. The most accurate way to measure a phase shift is by using a stabilized interferometer [73]. By using this method accuracies below 0.5°can be achieved, although only the phase shift and not the whole density matrix is being measured. Those publications are all works in the context of measuring phaseshifts of single photons caused by single atoms.

Average quality In order to derive a mean trace distance, several hundred randomly chosen states were prepared using another pair of steppermotors. For this, angles were randomly selected and the presumably prepared states were calculated. In total a mean trace distance of (0.031 ± 0.012) can be achieved with a minimum of 0.002 and a maximum of 0.064. The average error of the phaseshift is $(3.53 \pm 0.02)°$.

Comparison between maximum likelihood and linear tomography A comparative depiction of the results of the maximum likelihood estimation and the linear tomography is shown in figure 61. In all cases the maximum likelihood estimation beats the linear calculation. For example for the $|L\rangle$ state prepared with two waveplates the average distance of the estimation to the presumably prepared state is (0.049 ± 0.001), whereas the linear tomography yields a distance of (0.052 ± 0.002).

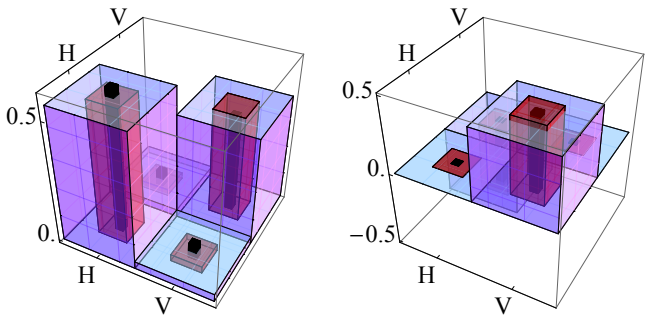

Figure 61: Blue: Linear estimation, Red: Maximum likelihood estimation, Black: Presumably prepared state. Left: Real part of the density matrices, Right: Imaginary part.

5.4.2. Quantum process tomography

For the test of the the quantum process tomography, waveplates with retardations $(0.973 \pm 0.014)\pi$ and $(0.468 \pm 0.0005)\pi$ were used for preparing the input states $|H\rangle$, $|V\rangle$, $|D\rangle$ and $|L\rangle$ and waveplates with retardations $(0.939 \pm 0.009)\pi$ and $(0.510 \pm 0.0004)\pi$ were used for analyzing the state. Three tests were made. The first without any optical device inbetween the preparation and the analyzation, next with a $\pi-$waveplate with retardation $(0.94 \pm 0.01)\pi$ and last with a polarizing beamsplitter, which is specified with an extinction ratio of $< 1:1000$.

No optics In this case, the "gate" acts like an identity matrix on the incoming state, apart from measurement errors. 260 measurement runs yield an average distance between input

state and measured state of (0.043 ± 0.021). This is slightly larger, than the distance error obtained in the previous section, which is due to an erroneous setting of the input states. In fact, the input states have never been perfectly polarized, like it would have been necessary for the algorithm presented in 5.2.3.

Waveplate A π-waveplate at an angle of $\pi/4$ acts like a Pauli X-gate $\begin{pmatrix} 0 & 1 \\ 1 & 0 \end{pmatrix}$ [19], which swaps $|H\rangle$ and $|V\rangle$ or $|L\rangle$ and $|R\rangle$ respectively. The average measured phaseshift between $|H\rangle$ and $|V\rangle$ ($|L\rangle$ and $|R\rangle$) is $(0.96 \pm 0.02)\pi$, which is in accordance to the retardation of the waveplate obtained with the method presented in 5.3.3.

Polarizing beamsplitter A polarizer $\begin{pmatrix} 1 & 0 \\ 0 & 0 \end{pmatrix}$ is not a quantum gate, since it is not a unitary matrix, that means, it is not energy conserving. The trace distance between the measured $|H\rangle$ and the input states $|H\rangle$, $|D\rangle$ and $|L\rangle$ is (0.005 ± 0.003) as expected. The $|V\rangle$ state will vanish completely and a tomography of this state should yield a completely mixed state. This becomes visible by calculating $\mathrm{tr}(\rho^2) \neq 1$ for all $|V\rangle$ input states and can be quantified by looking at the von Neumann entropy, which is (0.10 ± 0.05). Note, that this way of proceeding is questionable, since the method of quantum state tomography will more likely produce a pure state. For random results of the state estimation, the process tomography will still yield impure states, although the quantization of the mixedness by means of the von Neumann entropy shows clearly an underestimation of the impureness.

5.5. Guide to the program

The Matlab code for the tomography was originally written at the group of Paul Kwiat at the university of Illinois. During this thesis the code was completely revised, filled with comments and adapted to our purposes. Without going into too much detail I will outline the major parts of the program and explain how to insert data and configurations. Along with the program come sample code snippets and sample data files, which contain much more comments and information about the functions.

5.5.1. Main program parts

The tomography begins by initializing a `Tomography` object, whereby data and configurations are loaded and checked for obvious errors. By calling the basic routine `state_tomography(obj)`, the program starts calculating the state $|r\rangle$ in which we project the input state and the corresponding transformation matrix $\tilde{\tilde{M}}_{V,r}$. For example different detector efficiencies, beamsplitter crosstalk, accidental counts and the retardations can be taken into account.
This is then followed by a deterministic calculation of the density matrix in the class `LinearTomography`. The resulting density matrix is used as a starting point for the maximum likelihood algorithm and it can also be used to compensate for different intensities of the measurements for different bases.

The main class is `MLTomography`, where the equation (50) gets optimized using the Matlab internal routine `lsqnonlin`.
Furthermore there is a whole bunch of measurements available, like the entropy, the fidelity or the trace distance as well as several options to write the results.
Commands for controlling the scope and the motors can be found in `@ExperimentControl`. The commands for the motors just call functions from a python script made by the 3rd insitute of physics at the university of Stuttgart.

5.5.2. Configuration and raw data

The configuration file and the file with the raw measurements have to be saved in the form `NAMEconf.txt` and `NAMEraw_counts.txt`. The files are of the form:

```
struct
        configparameter: value
endstruct
```

It is possible to run the program without setting any options, in this case some preset options will be used. The following configurations can be set:

- `NDetectors`: Set to 1 for n detectors or 2 for 2n detectors.
- `NQubits`: Number of qubits.
- `QuditSizes`: Size of each Qudit.
- `StateDimension`: Dimension of the HilbertSpace.
- `DoDriftCorrection`: 1:yes, 0:no, Uses the result of `LinearTomography` for drift correction.
- `PDC`: 1:yes, 0:no, Calculates accidental counts, only meaningful for parametric down-conversion.
- `DarkCounts`: 1:yes, 0:no, Correction of dark counts.
- `DarkCountRates`: [counter1, counter2], Dark count rates for every counter in nanoseconds.
- `Window`: Coincidence window in nanoseconds.
- `Crosstalk`: $[C_{0\to0}, C_{0\to1}; C_{1\to0}, C_{1\to1}]$, Crosstalk matrix of Beamsplitters.
- `Efficiency`: [counter1, counter2], Efficiency for each counter.
- `Angles`: 0: Use `settings` in `raw_counts.txt`, 1:Angles in units of Pi are given in `raw_counts.txt`.
- `Retardation`: $[WP_{\pi,qubit1}, WP_{\pi/2,qubit1}; WP_{\pi,qubit2}, WP_{\pi/2,qubit2}]$, Retardation of wave-plates in units of Pi, only required, when Angles=1.

- `ProjectState`: [1,0], Projecting channel in which the detector is standing; e.g. $[1,0] = |H\rangle$, $[0,1] = |V\rangle$. Only required for the n-detector case.
- `PowerError`: Error in the power measurement, use only for coherent light source, otherwise set to 0, then a poissonian distribution is assumed.
- `SettingsError`: Error in waveplate setting in degrees or error in settings in units of π.
- `TempDependence`: Temperature dependence of the retardation of the waveplates in $\pi/°$C.
- `UseDerivatives`: 1:yes, 0:no, Use derivative of maximum likelihood function to increase speed of calculation.
- `Measurements`: 1:yes, 0:no, Do several measurements at the end.
- `EstimatedCounts`: 1:yes, 0:no, Show actually estimated counts at the end, only possible if Measurements=1.
- `ErrorEstim`: Number of cycles for error estimation, 0: No error estimation.
- `Write`: 1:yes, 0:no, Write results.
- `Overwrite`: 1:yes, 0:no, Overwrite previous file or make backup.
- `PDF`: 1:yes, 0:no, Create .pdf with results and plots.

The raw data has to be given in the following form:

- `time`: [msrm1; ...; msrmN], Time of each complete measurement in nanoseconds
- `singles`: [msrm1 ctr1, msrm1 ctr2; ...; msrmN ctr1, msrmN ctr2], Amount of nonintended or nontriggered counts, used to calculate amount of accidental counts.
- `coincidences`: [msrm1 ctr1, msrm1 ctr2; ...; msrmN ctr1, msrmN ctr2], Amount of counts in counter r for the ν-th measurement.
- `settings`: [msrm1 qubit1, msrm1 qubit2; ...; msrmN qubit1, msrmN qubit2], Each qubit gets projected in a state of the form $\alpha|H\rangle + \beta|V\rangle$. α and β have to be written for each measurement and qubit in the corresponding space.
- `angles`: [msrm1 qubit1, msrm1 qubit2; ...; msrmN qubit1, msrmN qubit2], Like `settings` but with the angles of the two waveplates instead of α and β.
- `intensities`: [msrm1, ..., msrmN], Total intensity of the ν-th measurement.

5.6. Concluding remarks

Although the method of reconstructing a quantum state presented here is already quite sophisticated, there are some remarks to make.

5.6.1. Pitfalls

It is undoubtly dangerous to edit the acquired data in order to get physical results. But in most cases this is necessary, because the deterministic calculation of the density matrix yields negative eigenvalues.
The problem is, that in maximum likelihood estimation, the state often lies directly on the boundary of the n-dimensional Poincaré sphere and has therefore eigenvalues which are equal to zero. While this is no violation of the physicality constraint it is still implausible. This is similar to throwing a coin N times. If by chance head is lying ontop N times, it is still not justified to set the probability of getting tails equal to zero. Moreover, the errorbars get restricted. Since there cannot be a negative probability of getting tails we have to say, the probability is zero or maybe larger but certainly not smaller. This is a implausible restriction of the error bounds [74].
The underlying problem is, that observed intensities are being interpreted as probabilities, with which one wants to predict every possible outcome of an arbitrary measurement on the system. This will not work, since an interpretation of intensities as probabilities is only valid for an infinitesimal large amount of samples. As an extreme example, assume an experiment, where a coin is only thrown once and heads is ontop. The result of a maximum likelihood estimation based on this one experiment will yield, that heads must be lying ontop in every subsequent experiment [74].
A method, which tries to avoid these pitfalls is bayesian mean estimation [75], which is not part of this thesis.
Fitting theory curves to datapoints is normally no problem, but it is questionable whether showing only the fit without the data is a good way to go. Of course no one is really showing the results of a linear inversion of the data, because it is in the most cases unphysical and it is hard to visualize the data and the fit together in a meaningful way.

5.6.2. Other methods

There exist other methods to reconstruct the quantum state of a system, like permutationally invariant tomography and compressed sensing, which rely on assumptions made on the properties of the density matrix [76]. If it comes to special properties of the density matrix, like showing entanglement or a violation of the bell inequalities, there are other methods, which require much less measurement settings.

6. Summary

In this thesis the results of the single-photon transistor [23] have been presented. For a source photon rate of $R_{s,in} = 0.69(1)\ \mu s^{-1}$ and on average $1.04(3)$ incoming gate photons an optical contrast of $0.39(4)$ could be measured. We predict a contrast of $0.53(2)$ for a single deterministic gate photon. For $0.75(3)$ gate photons a gain of $10(1)$ could be achieved. With our method we were able to predict the presence of a Rydberg atom with a fidelity of $0.79(4)$.
In order to apply the transistor scheme for spatially resolved imaging of the blockade sphere around Rydberg atoms, an imaging system has been designed with Zemax and characterized yielding a resolution of at least $(1.55 \pm 0.1)\ \mu$m and a magnification of (8.53 ± 0.37).
During the course of this thesis an electric field control was put inside the experiment chamber. Therefore the complete design, assembly and testing was done. The field control is in theory able to compensate electric stray fields down to $\approx 10^{-6}$ V/mm, much beyond the resolution of our laser linewidth. Atoms with principal quantum number down to $n^* = 44$ are ionizable with 500 V at two electrodes. Among other electronics, like voltage supplies, two different kinds of ion detectors were tested and characteristic values are presented here. To further improve the total experimental setup, we chose to exchange the current glass cell with a chamber made from quartz glass, where the tendency of thermal lensing is no longer so strongly pronounced.
Preparatory work for realizing a controlled phase gate has been done by setting up and thoroughly testing the method of maximum likelihood estimation. For this purpose all involved optics and electronics were characterized. For example the Allan deviation of the logarithmically amplified photodiode or the extinctions of the polarizing beamsplitters have been determined. Furthermore the effect of temperature and wavelength differences on the retardation of waveplates have been investigated. It was shown, that quantum states encoded in the polarization of the radiation field can be determined with an error minimum corresponding to a phaseshift of $0.5°$. For random states the average accuracy corresponds to a trace distance of (0.031 ± 0.012), which corresponds to a phaseshift of $(3.53 \pm 0.02)°$. With this method quantum gates can be characterized. As an example, the effect of a π-waveplate acting like a pauli X-gate on the incoming state was measured and a retardation of $(0.96 \pm 0.02)\pi$ could be retrieved, which fits well to the retardation of the waveplate of $(0.94 \pm 0.01)\pi$ quantified with another method presented in chapter 5.3.3.
With this work some more steps have been achieved towards the realization of a controlled phase gate in free space. The next major step will be to realign the whole experiment around the new chamber and to test and calibrate the electric field control together with the atoms. Also the imaging setup has to be adjusted together with the atoms and one has to see, whether the contrast is sufficient to observe the blockade radius.

A. References

[1] M. Fox, *Quantum Optics : An Introduction: An Introduction*. Oxford Master Series in Physics, OUP Oxford, 2006.

[2] D. Englund, A. Faraon, I. Fushman, N. Stoltz, P. Petroff, and J. Vuckovic, "Controlling cavity reflectivity with a single quantum dot," *Nature*, vol. 450, pp. 857–861, 2007.

[3] I. Fushman, D. Englund, A. Faraon, N. Stoltz, P. Petroff, and J. Vuckovic, "Controlled phase shifts with a single quantum dot," *Science*, vol. 320, no. 5877, pp. 769–772, 2008.

[4] K. D. Jöns, P. Atkinson, M. Müller, M. Heldmaier, S. M. Ulrich, O. G. Schmidt, and P. Michler, "Triggered indistinguishable single photons with narrow line widths from site-controlled quantum dots," *Nano Letters*, vol. 13, no. 1, pp. 126–130, 2013. PMID: 23198958.

[5] T. Wilk, S. C. Webster, A. Kuhn, and G. Rempe, "Single-atom single-photon quantum interface," *Science*, vol. 317, pp. 488 – 490, 2007.

[6] A. Rauschenbeutel, G. Nogues, S. Osnaghi, P. Bertet, M. Brune, J. M. Raimond, and S. Haroche, "Coherent operation of a tunable quantum phase gate in cavity qed," *Phys. Rev. Lett.*, vol. 83, pp. 5166–5169, Dec 1999.

[7] D. Chang, V. Gritsev, G. Morigi, V. Vuletic, M. Lukin, and E. Demler, "Crystallization of strongly interacting photons in a nonlinear optical fiber," *Nature Physics*, vol. 4, pp. 884 – 889, 2008.

[8] M. Bajcsy, S. Hofferberth, V. Balic, T. Peyronel, M. Hafezi, A. S. Zibrov, V. Vuletic, and M. D. Lukin, "Efficient all-optical switching using slow light within a hollow fiber," *Phys. Rev. Lett.*, vol. 102, p. 203902, 2009.

[9] K. Singer, M. Reetz-Lamour, T. Amthor, L. G. Marcassa, and M. Weidemüller, "Suppression of excitation and spectral broadening induced by interactions in a cold gas of rydberg atoms," *Phys. Rev. Lett.*, vol. 93, p. 163001, Oct 2004.

[10] M. Saffman, T. G. Walker, and K. Molmer, "Quantum information with rydberg atoms," *Rev. Mod. Phys.*, vol. 82, p. 2313, 2010.

[11] R. Löw, H. Weimer, J. Nipper, J. B. Balewski, B. Butscher, H. P. Büchler, and T. Pfau, "An experimental and theoretical guide to strongly interacting rydberg gases," *Journal of Physics B: Atomic, Molecular and Optical Physics*, vol. 45, no. 11, p. 113001, 2012.

[12] M. D. Lukin, M. Fleischhauer, R. Cote, L. M. Duan, D. Jaksch, J. I. Cirac, and P. Zoller, "Dipole blockade and quantum information processing in mesoscopic atomic ensembles," *Phys. Rev. Lett.*, vol. 87, p. 037901, 2001.

[13] T. Wilk, A. Gaëtan, C. Evellin, J. Wolters, Y. Miroshnychenko, P. Grangier, and A. Browaeys, "Entanglement of two individual neutral atoms using rydberg blockade," *Phys. Rev. Lett.*, vol. 104, p. 010502, 2010.

[14] L. Isenhower, E. Urban, X. L. Zhang, A. T. Gill, T. Henage, T. A. Johnson, T. G. Walker, and M. Saffman, "Demonstration of a neutral atom controlled-not quantum gate," *Phys. Rev. Lett.*, vol. 104, p. 010503, Jan 2010.

[15] M. Fleischhauer and M. D. Lukin, "Dark-state polaritons in electromagnetically induced transparency," *Phys. Rev. Lett.*, vol. 84, pp. 5094 – 5097, 2000.

[16] J. D. Pritchard, D. Maxwell, A. Gauguet, K. J. Weatherill, M. P. A. Jones, and C. S. Adams, "Cooperative atom-light interaction in a blockaded rydberg ensemble," *Phys. Rev. Lett.*, vol. 105, p. 193603, 2010.

[17] Y. O. Dudin and A. Kuzmich, "Strongly interacting rydberg excitations of a cold atomic gas," *Science*, vol. 336, pp. 887–889, 2012.

[18] O. Firstenberg, T. Peyronel, Q. Liang, A. V. Gorshkov, M. D. Lukin, and V. Vuletic, "Attractive photons in a quantum nonlinear medium," *Nature*, vol. 502, pp. 71–75, 2013.

[19] M. Nielsen and I. Chuang, *Quantum Computation and Quantum Information*. Cambridge University Press, Cambridge, UK, 2000.

[20] T. Peyronel, O. Firstenberg, Q. Liang, S. Hofferberth, A. Gorshkov, T. Pohl, M. Lukin, and V. Vuletic, "Quantum nonlinear optics with single photons enabled by strongly interacting atoms," *Nature*, vol. 488, pp. 57–60, 2012.

[21] G. Günter, H. Schempp, M. R. de Saint-Vincent, V. Gavryusev, S. Helmrich, C. S. Hofmann, S. Whitlock, and M. Weidemüller, "Observing the dynamics of dipole-mediated energy transport by interaction-enhanced imaging," *Science*, vol. 342, pp. 954–956, 2013.

[22] G. Günter, M. Robert-de Saint-Vincent, H. Schempp, C. S. Hofmann, S. Whitlock, and M. Weidemüller, "Interaction enhanced imaging of individual rydberg atoms in dense gases," *Phys. Rev. Lett.*, vol. 108, p. 013002, Jan 2012.

[23] H. Gorniaczyk, C. Tresp, J. Schmidt, H. Fedder, and S. Hofferberth, "Single-photon transistor mediated by interstate rydberg interactions," *Phys. Rev. Lett.*, vol. 113, p. 053601, Jul 2014.

[24] C. Adams, "Optical transistor flips on with one photon," *Physics*, vol. 7, p. 80, Jul 2014.

[25] W. Chen, K. M. Beck, R. Bücker, M. Gullans, M. D. Lukin, H. Tanji-Suzuki, and V. Vuletic, "All-optical switch and transistor gated by one stored photon," *Science*, vol. 341, pp. 768–770, 2013.

[26] M. Müller, I. Lesanovsky, H. Weimer, H. P. Büchler, and P. Zoller, "Mesoscopic rydberg gate based on electromagnetically induced transparency," *Phys. Rev. Lett.*, vol. 102, p. 170502, Apr 2009.

[27] Y. Han, B. He, K. Heshami, C.-Z. Li, and C. Simon, "Quantum repeaters based on rydberg-blockade-coupled atomic ensembles," *Phys. Rev. A*, vol. 81, p. 052311, May 2010.

[28] D. Møller, L. B. Madsen, and K. Mølmer, "Quantum gates and multiparticle entanglement by rydberg excitation blockade and adiabatic passage," *Phys. Rev. Lett.*, vol. 100, p. 170504, Apr 2008.

[29] A. Reiserer, N. Kalb, G. Rempe, and S. Ritter, "A quantum gate between a flying optical photon and a single trapped atom," *Nature*, vol. 508, pp. 237–240, 2014.

[30] M. Fleischhauer and M. D. Lukin, "Quantum memory for photons: Dark-state polaritons," *Phys. Rev. A*, vol. 65, p. 022314, Jan 2002.

[31] M. Fleischhauer, A. Imamoğlu, and J. Marangos, "Electromagnetically induced transparency: Optics in coherent media," *Rev. Mod. Phys.*, vol. 77, p. 633, 2005.

[32] D. A. Steck, "Rubidium 87 d line data," 2001.

[33] D. Maxwell, D. J. Szwer, D. Paredes-Barato, H. Busche, J. D. Pritchard, A. Gauguet, K. J. Weatherill, M. P. A. Jones, and C. S. Adams, "Storage and control of optical photons using rydberg polaritons," *Phys. Rev. Lett.*, vol. 110, p. 103001, Mar 2013.

[34] K. Singer, J. Stanojevic, M. Weidemüller, and R. Coté, "Long-range interactions between alkali rydberg atom pairs correlated to the ns-ns, np-np and nd-nd asymptotes," *Journal of Physics B: Atomic, Molecular and Optical Physics*, vol. 38, no. 2, p. S295, 2005.

[35] A. V. Gorshkov, J. Otterbach, M. Fleischhauer, T. Pohl, and M. D. Lukin, "Photon-photon interactions via rydberg blockade," *Phys. Rev. Lett.*, vol. 107, p. 133602, 2011. arXiv:1103.3700v1.

[36] R. Heidemann, U. Raitzsch, V. Bendkowsky, B. Butscher, R. Löw, L. Santos, and T. Pfau, "Evidence for coherent collective rydberg excitation in the strong blockade regime," *Phys. Rev. Lett.*, vol. 99, p. 163601, 2007.

[37] S. Baur, D. Tiarks, G. Rempe, and S. Dürr, "Single-photon switch based on rydberg blockade," *Phys. Rev. Lett.*, vol. 112, p. 073901, Feb 2014.

[38] J. Bochmann, M. Mücke, C. Guhl, S. Ritter, G. Rempe, and D. L. Moehring, "Lossless state detection of single neutral atoms," *Phys. Rev. Lett.*, vol. 104, p. 203601, May 2010.

[39] B. Olmos, W. Li, S. Hofferberth, and I. Lesanovsky, "Amplifying single impurities immersed in a gas of ultracold atoms," *Phys. Rev. A*, vol. 84, p. 041607, Oct 2011.

[40] E. Hecht, *Optik*. Oldenbourg, 2005.

[41] L. M. Bennie, P. T. Starkey, M. Jasperse, C. J. Billington, R. P. Anderson, and L. D. Turner, "A versatile high resolution objective for imaging quantum gases," *Opt. Express*, vol. 21, pp. 9011–9016, Apr 2013.

[42] J. Nipper, J. B. Balewski, A. T. Krupp, B. Butscher, R. Löw, and T. Pfau, "Highly resolved measurements of stark-tuned förster resonances between rydberg atoms," *Phys. Rev. Lett.*, vol. 108, p. 113001, Mar 2012.

[43] M. S. O'Sullivan and B. P. Stoicheff, "Scalar polarizabilities and avoided crossings of high rydberg states in rb," *Phys. Rev. A*, vol. 31, pp. 2718–2720, Apr 1985.

[44] J. Balewski, A. Krupp, A. Gaj, D. Peter, H. Buchler, R. Low, S. Hofferberth, and T. Pfau, "Coupling a single electron to a bose-einstein condensate," *Nature*, vol. 502, pp. 664–667, 2013.

[45] N. L. M. Müller, "Excitation and detection of rydberg atoms in an ultracold gas," Master's thesis, University of Heidelberg, 2010.

[46] H.-J. Bargel, H. Hilbrans, and G. Schulze, *Werkstoffkunde*. VDI-Buch, Springer, 2008.

[47] S. Sgobba, "Physics and measurements of magnetic materials," *arXiv*, no. arXiv:1103.1069, 2011.

[48] S. Sgobba, "Materials for high vacuum technology: an overview s. sgobba," *CERN*.

[49] S. N. Atutov, R. Calabrese, V. Guidi, B. Mai, A. G. Rudavets, E. Scansani, L. Tomassetti, V. Biancalana, A. Burchianti, C. Marinelli, E. Mariotti, L. Moi, and S. Veronesi, "Fast and efficient loading of a rb magneto-optical trap using light-induced atomic desorption," *Phys. Rev. A*, vol. 67, p. 053401, May 2003.

[50] L. JapanCell Co., *Technical Drawing of the Glass Cell JPC-4-0921*, 2014.

[51] K. M. Birnbaum and T. Q. O. Group, "Ultra-high vacuum chambers," *Cal-Tech*, 2005.

[52] F. Paschen, *Ueber die zum funkenübergang in luft: wasserstoff und kohlensäure bei verschiedenen drucken erforderliche potentialdifferenz ...* J.A. Barth, 1889.

[53] C. L. Wadhwa, *High voltage engineering. 2nd ed.* New Age International Pub- lishers, 2007.

[54] CGC Instruments, *Universeller digital gesteuerter dreifacher Analogschalter/ Multiplexer NIM-AMX500-3 für Spannungen bis 500 V - Bedienungsanleitung*.

[55] Hamamatsu, *MCP Assembly*, 2006.

[56] Hamamatsu, *MCP & MCP Assembly, Selection Guide*, 2013.

[57] J. L. Wiza, "Microchannel plate detectors," *Nuclear Instruments and Methods*, vol. 162, no. 1-3, pp. 587 – 601, 1979.

[58] Hamamatsu, "Mcp f4655-13 specsheet," tech. rep., 2014.

[59] Burle, *Channeltron - Electron Multiplier, Handbook for Mass Spectrometry Applications*.

[60] Photonis, *MAGNUM Electron Multiplier 5900 Series*, 2009.

[61] J. Altepeter, E. Jeffrey, and P. Kwiat, "Photonic state tomography," vol. 52 of *Advances In Atomic, Molecular, and Optical Physics*, pp. 105 – 159, Academic Press, 2005.

[62] I. L. Chuang and M. A. Nielsen, "Prescription for experimental determination of the dynamics of a quantum black box," *Journal of Modern Optics*, vol. 44, no. 11-12, pp. 2455–2467, 1997.

[63] Z. Hradil, J. Rehacek, J. Fiurasek, and M. Jezek, *Quantum State Estimation*, ch. Maximum-Likelihood Methods in Quantum Mechanics, pp. 59–100. Lecture Notes in Physics, Springer, 2004.

[64] M. Mohseni, A. T. Rezakhani, and D. A. Lidar, "Quantum-process tomography: Resource analysis of different strategies," *Phys. Rev. A*, vol. 77, p. 032322, Mar 2008.

[65] D. H. Mahler, L. A. Rozema, A. Darabi, C. Ferrie, R. Blume-Kohout, and A. M. Steinberg, "Adaptive quantum state tomography improves accuracy quadratically," *Phys. Rev. Lett.*, vol. 111, p. 183601, Oct 2013.

[66] T. T. Aalto, M. Harjanne, and M. Kapulainen, "Method for the rotational alignment of polarization-maintaining optical fibers and waveguides," *Optical Engineering*, vol. 42, no. 10, pp. 2861–2867, 2003.

[67] J. A. Barnes, A. R. Chi, L. S. Cutler, D. J. Healey, D. B. Leeson, T. E. McGunigal, J. A. Mullen, W. L. Smith, R. L. Sydnor, R. F. C. Vessot, and G. M. R. Winkler, "Characterization of frequency stability," *Instrumentation and Measurement, IEEE Transactions on*, vol. IM-20, pp. 105–120, May 1971.

[68] A. Márquez, C. Cazorla, M. J. Yzuel, and J. Campos, "Characterization of the retardance of a wave plate to increase the robustness of amplitude-only and phase-only modulations of a liquid crystal display," *Journal of Modern Optics*, vol. 52, no. 4, pp. 633–650, 2005.

[69] P. D. Hale and G. W. Day, "Stability of birefringent linear retarders(waveplates)," *Appl. Opt.*, vol. 27, pp. 5146–5153, Dec 1988.

[70] C. Hernández-Rodríguez and P. Gómez-Garrido, "Optical anisotropy of quartz in the presence of temperature-dependent multiple reflections using a high-accuracy universal polarimeter," *Journal of Physics D: Applied Physics*, vol. 33, no. 22, p. 2985, 2000.

[71] S.-M. F. Nee, C. Yoo, T. Cole, and D. Burge, "Characterization for imperfect polarizers under imperfect conditions," *Appl. Opt.*, vol. 37, pp. 54–64, Jan 1998.

[72] Q. A. Turchette, C. J. Hood, W. Lange, H. Mabuchi, and H. J. Kimble, "Measurement of conditional phase shifts for quantum logic," *Phys. Rev. Lett.*, vol. 75, pp. 4710–4713, Dec 1995.

[73] S. A. Aljunid, M. K. Tey, B. Chng, T. Liew, G. Maslennikov, V. Scarani, and C. Kurtsiefer, "Phase shift of a weak coherent beam induced by a single atom," *Phys. Rev. Lett.*, vol. 103, p. 153601, Oct 2009.

[74] R. Blume-Kohout, "Optimal, reliable estimation of quantum states," *New Journal of Physics*, vol. 12, no. 4, p. 043034, 2010.

[75] R. S. C. A. Fuchs, *Unknown Quantum States and Operations, a Bayesian View*, ch. Maximum-Likelihood Methods in Quantum Mechanics, pp. 147–182. Lecture Notes in Physics, Springer, 2004.

[76] C. Schwemmer, G. Tóth, A. Niggebaum, T. Moroder, D. Gross, O. Gühne, and H. Weinfurter, "Experimental comparison of efficient tomography schemes for a six-qubit state," *Phys. Rev. Lett.*, vol. 113, p. 040503, Jul 2014.

B. Eigenständigkeitserklärung

Hiermit erkläre ich, dass ich die vorliegende Arbeit selbstständig verfasst habe. Ich habe keine anderen als die angegebenen Quellen benutzt und alle wörtlich oder sinngemäß aus anderen Werken übernommenen Aussagen als solche gekennzeichnet. Die vorliegende Arbeit war weder vollständig noch in Teilen Gegenstand eines anderen Prüfungsverfahrens. Der Inhalt des elektronischen Exemplars stimmt mit dem Druckexemplar überein.

Stuttgart, 24.10.2014

Johannes Schmidt